DISS. ETH N° 20551

Reconstruction of the muon tracks in the OPERA experiment and first results on the light collection in the ArDM experiment

A dissertation submitted to

ETH ZURICH

for the degree of

Doctor of Sciences

presented by

Claudia Lazzaro

MSc Physics, Università degli Studi di Padova

born on April 29 1981 in Dolo (Italy)

citizen of Italy

accepted on the recommendation of

Prof. Dr. André Rubbia, examiner
Prof. Dr. Günther Dissertori, co-examiner

2012

Abstract

The OPERA Experiment (Oscillation Project with Emulsion tRacking Apparatus) is a long-baseline neutrino oscillation experiment. The goal is the first observation of the ν_τ appearance in a pure ν_μ beam. The beam is produced at CERN and sent to Gran Sasso (CNGS), with a base-line of 730 km, and it is optimized to detect the ν_τ appearance. The ν_τ appearance is proved by the detection of the τ lepton produced in the charged current ν_τ interaction, identifying the different τ decay topologies. The experiment requires a high spatial resolution and a large detector mass, requirements fulfilled using a sandwich of nuclear emulsion films and lead plates.

The neutrino interactions in OPERA are triggered by the electronic detectors composed of scintillator planes, which interleave the target walls consisting of nuclear emulsion/lead bricks, and the magnetic spectrometers placed downstream of the two identical target sector modules, which are equipped with drift tubes. The electronic detector data analysis aims to trigger the neutrino events (and reconstruct the tracks due to charged particles). After the track reconstruction, a Kalman filter is applied to find the origin of the track in the target and to estimate the momentum at the interaction vertex. Focusing on the muon track from ν_μ charged current interactions, a monitoring of the CNGS beam and an estimation of the expected neutrino interactions is possible. In particular, the Kalman procedure is described and the momentum resolution and the track position estimation is investigated in this thesis, including the analysis of the electronic detector data taken during the years 2008, 2009, 2010, reporting the reconstructed muon momentum spectrum. The reconstructed muon momentum spectrum, and its comparison with the MonteCarlo expectation has then been used to estimate the number of the τ decays expected.

Furthermore, a brief overview of the ArDM (Argon Dark Matter) experiment and the analysis of the first calibration run is reported. The calibration run includes some tests using an external ^{22}Na source, which allows to study the collection of the LAr scintillation light in the detector.

Abstract

OPERA (Oscillation Project with Emulsion tRacking Apparatus) e' un esperimento di oscillazione di neutrini. Il suo obiettivo e' l'osservazione della comparsa di un neutrino ν_τ in un fascio di neutrini ν_μ. Il fascio di neutrini ν_μ viene generato al CERN in direzione del Gran Sasso (CNGS). Ha una lunghezza di percorrenza di 730 km, ed e' stato ottimizzato per ottenere la miglior efficienza di rivelazione della comparsa del ν_τ. L'apparizione del ν_τ viene verificata mediante la rivelazione del leptone τ, generato nelle interazioni di neutrino di corrente carica, identificando i differenti decadimenti del leptone. Questo richiede un esperimento con una risoluzione spaziale molto elevata, ed allo stesso tempo, per compensare la piccola sezione d'urto dei neutrini, un rivelatore con una grande massa. Queste opposte condizioni vengono soddisfatte utilizzando piccole unita', i bricks, costituiti da lastrine di piombo intervallati da films di emulsioni nucleari.

Le interazioni di neutrino in OPERA sono triggerati da rivelatori elettronici formati da piani di scintillatori che intervallano il bersaglio costituito da muri di bricks, e dagli spettrometri posti dopo ogni modulo del bersaglio, che includono dei tubi a deriva.

L'analisi dei dati ottenuti con i rivelatori elettronici permette di selezionare le interazioni di neutrino interne ad OPERA, e ricostruire gli eventi (le tracce dovute a particelle cariche). Sulle tracce ricostruite viene poi applicato un Kalman filter, che permette di avere una stima della posizione di inizio della traccia, che determina il punto di interazione del neutrino, e inoltre una stima del momento della particella in questo punto. Concentrando l'analisi sulle tracce muoniche, e' possible ottenere un controllo del fascio CNGS, e una stima degli eventi attesi nel rivelatore. In questa tesi il Kalman filter, la risoluzione del momento e la stima della posizione della traccia vengono discussi, includendo l'analisi dei dati del 2008, 2009 e 2010 e la ricostruzione dello spettro del momento delle tracce muoniche ricostruite. Lo spettro del momento delle tracce muoniche ricostruite, e il suo confronto con le stime MonteCarlo sono stati poi utilizzati per ottenere una stima del numero di neutrini tau attesi.

Inoltre una breve introduzione dell'esperimento ArDM (Argon Dark Matter), e dell'analisi della prima presa dati, di calibrazione, vengono discusse nell'ultima parte della tesi. La presa dati di calibrazione include l'uso di una sorgente di raggi gamma (NaI) posizionata esternamente al rivelatore, dalla cui analisi dati e' stato possibile avere una stima della capacita' di rivelazione della luce in ArDM.

Contents

Introduction

In modern particle physics two main field still under investigation are: the neutrino physics and the dark matter search. In the first part of the thesis the neutrino physics and the OPERA experiment will be discussed, the second part will be focused on the dark matter research and in particular on the ArDM experiemnt and the work done in the first calibration run of the experiment.

In the Standard Model of particle physics, neutrinos are classified as massless, left-handed particles, however, since the 70's some anomalies in the neutrino experimental results were found. In particular, experiments measuring the solar neutrino observed a deficit flux compared to the the expectation from solar model calculations. Later, an anomaly was also observed with atmospheric neutrino measurments, mainly by the SuperKamiokande (SK) experiment. These experimental results seem to be explained by neutrino oscillations that involves a flavour oscillation between neutrino types. However, the neutrino oscillations are possible only if not all the neutrinos are degenerate in mass, requiring the extension of the theory beyond the Standard Model. Many experiments in the last two decades obtained important results supporting the oscillation phenomenon, and measured the parameters describing it. Still many issues remain unresolved in neutrino physics: the nature (Majorana or Dirac) of the neutrinos, the absolute masses of the neutrinos, the mass hierarchy between them, and, concerning the neutrino oscillation the sub-leading oscillation, amplitude in the atmospheric sector. Also, the direct evidence of the $\nu_\mu \rightarrow \nu_\tau$ appearance in an accelerator neutrino beam is an important ingredient.

OPERA is an appearance experiment, it aims to prove the $\nu_\mu \rightarrow \nu_\tau$ oscillation via the detection of the τ lepton produced in the charged current neutrino interactions. The detection of the τ, having a very short lifetime, requires a high spatial resolution, on the other hand, the very small cross section of the neutrino interactions requires a large target mass. The OPERA experiment was realized using the emulsion technique: a sandwich of emulsion films and lead plates set up the target of the experiment. The target is divided into small stand-alone units, called bricks, and it has a total mass of 1.25 kton. The OPERA experiment includes also electronic detectors composed of scintillator planes , which interleave the target walls, and the magnetic spectrometers placed downstream of each target sector module, which are equipped with drift tubes and resistive plate chambers.

The electronic detectors aim to trigger the neutrino events and subsequently the reconstruction of the tracks to find the brick, in which the interaction occurred. The

reconstruction with the electronic detector data is also important to track the path of the charged particles; this permits to identify the muon tracks produced in the ν_μ CC events. The reconstruction and identification of the muon tracks in OPERA is used first of all to identify the ν_μ interactions, preventing to misidentify them as ν_τ interactions. It also allows to monitor the CNGS beam and to estimate the number of expected events. The estimation of the muon momentum is obtained by the Kalman filter procedure applied to the tracks identified as muons in the events.

The OPERA commissioning run took place in 2006; the first short run in 2007, with only few bricks in the target allowed a test of the detector and the analysis chain.The physics runs with a full detector were in 2008, 2009 and 2010; a first τ candidate was observed in 2009, in a subsample of the 2008/2009 events which were analysed.

The thesis work will be organised as follows: in the first chapter a review of the neutrino physics and the main neutrino oscillation experiments is presented. A brief introduction of the open issues in the neutrino oscillation theory is also given in the last part of the chapter.

In the second chapter the OPERA experiment with a detailed description of the detector, together with the performance and the main issues of the analysis, are presented. The different decay topologies of the τ and the different analysis requirements are also described. The current status of the analysis, with a short selection of the main results of the 2008 and 2009 data concludes the chapter.

In the third chapter the reconstruction of the charged particle tracks with the electronic detector is described. After a short summary on the tracking, a theoretical introduction to the Kalman procedure is reported; then the chapter focuses on the Kalman filter applied to the OPERA tracking. In the second part of this chapter the MC studies on the charged current events, made for this thesis, are depicted; they test the expected resolution on the position and the momentum reconstructed for the muon tracks. Since the main goal of this thesis is the muon track reconstruction and the evaluation of the muon momentum spectrum, in the last part of the chapter a MC analysis on different samples of events is presented. It includes also neutral current and anti-neutrino events, which could contaminate the muon sample.

In the chapter four the analysis of the electronic detector data, for the 2008, 2009 and 2010 runs, with the muon momentum spectrum and the data-MC comparison is reported, and the number of expected $\tau \to \mu$ decays is given.

The second part of the thesis is focused on a differnet topic, the ArDM (Argon Dark Matter) experiment. The goal of the ArDM experiment is the detection of the elastic collisions of WIMPS (Weakly Interacting Massive Particle) with argon nuclei, measuring the ionization charge and the argon scintillation light of the recoiling nuclei; WIMPS are leading candidates for the non-baryonic Dark Matter in the universe.

The ArDM experiment is in the commissioning phase, a short overview on the detector is reported. During the fall of 2010, a first test run took place to study the light collection in the detector. A summary of the run conditions and the tools to analyze the light signal is presented. Results are reported from a calibration run with an external ^{22}Na positron source. In the last part of the chapter the tools developed with GEANT4 software for the Monte Carlo studies are described, including the MC-

data comparison for the calibration run with the external source.

Part I

OPERA experiment

Chapter 1

Neutrino physics

The existence of a neutral weakly interacting particle was postulated by Pauli in 1930 to explain the continuous spectrum of the β decay [1]; this particle was then called neutrino in the four-fermion theory of β decay formulated by Fermi in 1934. The first experimental evidence of it was obtained only in 1956 by Reines and Cowan, in the first reactor-neutrino experiment, measuring the inverse β decay: $\overline{\nu}_e + p \rightarrow e^+ + n$. In 1958 the polarization of neutrinos was determined by measuring the helicity of gamma-rays produced in the radioactive decay of Europium-152 [2]; the neutrino was found to be left-handed. Later, the fact that the reaction $\mu \rightarrow e + \gamma$ was not observed, and that a ν_μ beam interacting in a target produces muons but not electrons, suggested that there are two different types of neutrinos, one associated with the electron and one with the muon. The concept of lepton flavor number was introduced and associated to the different lepton families. The third charged lepton, the τ was discovered only in 1975, and the corresponding neutrino ν_τ in 2000 in the DONUT experiment [3]. In the 70's Glashow, Weinberg and Salam formulated the electro-weak theory, which is part of what is now called the Standard Model (SM) of particle physics. It describes the particle properties, including the neutrino as massless and left-handed (assuming the non-existence of right-handed neutrino fields). The discovery in 1973 of neutral current neutrino interactions in the Gargamelle experiment at CERN [4] represents one of the most successful confirmations of the SM, followed in 1983 by the discovery of the Z and W boson. In 1989 LEP experiments at CERN, studing the Z width, fixed the number of light (interacting) neutrinos to three [5].

In the last decades, evidence for a non-zero neutrino mass was presented by many experiments, observing neutrino oscillation phenomena, which is only possible, when not all the neutrino masses are degenerate. This forces the physicists to introduce new physics beyond the SM.

1.1 Neutrino mass

In the SM neutrinos are assumed to be massless, with fixed helicity, it includes only the left-handed neutrino ν_L coupling to the $W^\pm$ (charged current interactions) or Z (neutral current interactions) and not the right-handed one. To include a massive

neutrino, considering only one neutrino field, it is possible to build a Dirac-mass or a Majorana-mass term and the Lagrangian changes as follows [6]:

Dirac mass A Dirac neutrino mass term is given by:

$$\mathcal{L}_D = -m_D \left(\overline{\nu_L}\nu_R + \overline{\nu_R}\nu_L\right). \tag{1.1}$$

where ν_L and ν_R are respectively the chiral left-handed and right-handed components of the neutrino field, and m_D is a mass parameter. This term conserves the total lepton number, that distinguishes leptons from antileptons, in this case $\nu_i \neq \overline{\nu_i}$.

Majorana mass In 1937 Majorana discovered that a massive neutral fermion can be described by a spinor ψ with only two free components, if the condition: $\psi = \psi^c$ is imposed, the Majorana mass field can be written as $\psi = \psi_L + \psi_L^c$. The mass term for a left-handed field is given by:

$$\mathcal{L}_L^M = -\frac{1}{2} m_L (\overline{\nu_L^c}\nu_L + \overline{\nu_L}\nu_L^c) \tag{1.2}$$

and at the same time also a right-handed term can be added, and it is:

$$\mathcal{L}_R^D = -\frac{1}{2} m_R (\overline{\nu_R^c}\nu_R + \overline{\nu_R}\nu_R^c) \tag{1.3}$$

where ν_R^c represents the charge conjugate of ν_R and m_L and m_R are two mass parameters. Since both ν_R and $\overline{\nu_R^c}$ absorb ν and create $\overline{\nu}$, $\mathcal{L}$ mixes ν and $\overline{\nu}$; thus it does not conserve the lepton number.

Taking into account equations 1.1, 1.2, 1.3, the total mass term can be written as:

$$\mathcal{L}^{D+M} = \mathcal{L}^D + \mathcal{L}_L^M + \mathcal{L}_R^M \tag{1.4}$$

in the extended form with the weak isospin SU(2) doublets:

$$\mathcal{L}^{D+M} = -\frac{1}{2} \begin{pmatrix} \overline{\nu_L^c} & \overline{\nu_R} \end{pmatrix} \begin{pmatrix} m_L & m_D \\ m_D & m_R \end{pmatrix} \begin{pmatrix} \nu_L \\ \nu_R^c \end{pmatrix} \tag{1.5}$$

The fields ν_L and ν_R have not a definitive mass, in order to find the mass eigenstates, we have to diagonalize the mass matrix in the last equation. To do this it is possible to define:

$$\mathcal{L}^{D+M} = \frac{1}{2} \overline{N_L^c} M N_L + H.c. \tag{1.6}$$

where

$$M = \begin{pmatrix} m_L & m_D \\ m_D & m_R \end{pmatrix} \quad , \quad N_L = \begin{pmatrix} \nu_L \\ \nu_R^c \end{pmatrix} \tag{1.7}$$

and

$$N_L = Un_L \qquad with \qquad n_L = \begin{pmatrix} \nu_{1L} \\ \nu_{2L} \end{pmatrix}, \tag{1.8}$$

where U is an unitary mixing matrix, n_L the column matrix of the left-handed components of the massive neutrino fields. The mass matrix, expressed in the basis of the mass eigenstates, will be defined as:

$$U^T M U = \begin{pmatrix} m_1 & 0 \\ 0 & m_2 \end{pmatrix} \tag{1.9}$$

where m_k are real and positive for k=1,2. Considering the case of a real mass matrix M, it is possible to choose m_L and m_R as real and positive, with an appropriate choice of phase of the chiral fields ν_L and ν_R, so that the mass matrix M is real if m_D is real; and the mixing matrix U is represented by:

$$U = \mathcal{O}\rho \tag{1.10}$$

where $\mathcal{O}$ is an orthogonal matrix and ρ is the diagonal matrix of phases:

$$\mathcal{O} = \begin{pmatrix} \cos\theta & \sin\theta \\ -\sin\theta & \cos\theta \end{pmatrix} \qquad \rho = \begin{pmatrix} \rho_1 & 0 \\ 0 & \rho_2 \end{pmatrix} \tag{1.11}$$

with $\mid \rho_K \mid^2 = 1$. The orthogonal matrix $\mathcal{O}$ can be written as:

$$\mathcal{O}^T M \mathcal{O} = \begin{pmatrix} m'_1 & 0 \\ 0 & m'_2 \end{pmatrix} \tag{1.12}$$

leading to:

$$tan2\theta = \frac{2m_D}{m_R - m_L} \qquad and \qquad m'_{1,2} = \frac{1}{2} \mid m_L + m_R \pm \sqrt{(m_L - m_R)^2 + 4m_D^2} \mid \tag{1.13}$$

Since m_L and m_R have been chosen positive, m'_2 is always positive, while m'_1 is negative if $m_D^2 > m_L m_R$. Therefore, since the eq. 1.9 can be written as:

$$U^T M U = \rho_T \mathcal{O}^T M \mathcal{O} \rho = \begin{pmatrix} \rho_1^2 m'_1 & 0 \\ 0 & \rho_2^2 m'_2 \end{pmatrix} \tag{1.14}$$

we have $\rho_2^2 = 1$ always, and $\rho_1^2 = 1$ if $m'_1 \geq 0$ or $\rho_1^2 = -1$ if $m'_1 < 0$.

The diagonalized Dirac+Majorana mass term can be written as a sum of Majorana mass terms for neutrino fields $\nu_K = \nu_{kL} + \nu^c_{kL} + H.c.$ $(k = 1, 2)$

$$\mathcal{L}^{D+M} = \frac{1}{2} \sum_{k=1,2} m_k \overline{\nu^c_{kL}} \nu_{kL} + H.c. \tag{1.15}$$

so the two massive neutrinos are Majorana particles [6].

1.1.1 The See-Saw mechanism

It seems natural to assume that the Dirac neutrino mass m_D is of the same order of magnitude as the Dirac masses of the charged lepton (in the same family). The fact that the neutrino masses are much smaller than the corresponding charged lepton masses can be explained by the "see-saw" mechanism [7], considering the Dirac-Majorana mass term in the case $m_l = 0$ and $\mid m_D \mid \ll m_R$. In this case, considering 1.13:

$$m_1 \simeq \frac{m_D^2}{m_R} \ll \mid m_D \mid \qquad m_2 \simeq m_R \qquad tan\theta \simeq \frac{m_D}{m_R} \ll 1 \qquad \rho_1^2 = -1 \tag{1.16}$$

Being suppressed by the small ratio m_D/m_R, from Eq. 1.16 follows that m_1 is much smaller than m_D. Since m_2 is of the order m_R, a very heavy ν_2 corresponds to a very light ν_1, and vice versa as in a see-saw. Hence, the see-saw mechanism explains naturally the suppression of m_1 with respect to m_D, providing the most plausible explanation of the smallness of neutrino masses.

As it happens in the general case of a Majorana-Dirac mass term, another important consequence of the see-saw mechanism, in case it is realized in nature, is that massive neutrinos are Majorana particles [6].

1.2 Neutrino mixing

In the previous section we considered the existence of only one neutrino, but from the experimental evidences [5] it is clear that there are three leptonic generations $l_{L\alpha}$, where $\alpha = e, \mu, \tau$. The coupling of active neutrinos and charged leptons to the W boson is described in the Standard Model by the Lagrangian:

$$\mathcal{L}_W = -\frac{g}{2\sqrt{2}} \sum_{\substack{\alpha=e,\nu,\tau \\ \imath=1,2,3}} \left(\overline{l_{L\alpha}} \gamma^\lambda U_{\alpha i} \nu_{Li} W_\lambda^- + \overline{\nu_{Li}} \gamma^\lambda U_{\alpha i}^* l_{L\alpha} W_\lambda^+ \right) \tag{1.17}$$

Here, L denotes left-handed chiral projection, l_α is the charged-lepton mass eigenstate of flavor α, and ν_i is the neutrino mass eigenstate. The constant g is the weak coupling constant, and U is the leptonic mixing matrix. This is often called PMNS (Pontecorvo-Maki-Nakagawa-Sakata) matrix, in recognition of the pioneering contributions of the scientists to the physics of neutrino mixing [8]. Taking into account three active neutrinos, U is a 3×3 unitary matrix, a complex $N \times N$ unitary mixing matrix may contain $N(N-1)$ physically significant parameters in total [9]. So, in the case of Majorana neutrinos, the U matrix contains three mixing angles and three complex phase factors and is usually parametrized as:

$$U = \begin{pmatrix} c_{12}c_{13} & s_{12}c_{13} & s_{13}e^{-i\delta} \\ -s_{12}c_{23} - c_{12}s_{23}s_{13}e^{i\delta} & c_{12}c_{23} - s_{12}s_{23}s_{13}e^{i\delta} & s_{23}c_{13} \\ s_{12}s_{23} - c_{12}s_{23}s_{13}e^{i\delta} & -c_{12}c_{23} - s_{12}c_{23}s_{13}e^{i\delta} & c_{23}c_{13} \end{pmatrix} \times \begin{pmatrix} e^{i\xi_1/2} & 0 & 0 \\ 0 & e^{i\xi_2/2} & 0 \\ 0 & 0 & 1 \end{pmatrix} \tag{1.18}$$

Here, $c_{ij} \equiv \cos\theta_{ij}$ and $s_{ij} \equiv \sin\theta_{ij}$, and θ_{ij} the three mixing angles.

The quantities δ, ξ_1, ξ_2 are CP-violating phases; the ξ_1 and ξ_2, are known as Majorana phases.Thus, if the "neutrino state of the flavor α", $\mid \nu_\alpha\rangle$, is defined to be the neutrino state that accompanies the particular charged lepton $\bar{l}_\alpha$ in leptonic W^+ decay, then it has to be:

$$\mid \nu_\alpha\rangle = \sum_{i=1}^{3} U^*_{\alpha i} \mid \nu_i\rangle \tag{1.19}$$

To understand neutrino flavour change, consider a neutrino ν_α, produced via W decay, together with a lepton l_α, this then propagates in vacuum for a distance L to a detector, where it can interact via W exchange and produce a second charged lepton l_β; α and β could be different, and we refer to this case as neutrino oscillations [9].

The probability for a ν flavor transition is given by: $P(\nu_\alpha \to \nu_\beta) =\mid Amp(\nu_\alpha \to \nu_\beta) \mid^2 =\mid \langle \nu_\beta \mid \nu_\alpha(t)\rangle \mid^2$. The contribution of each ν_i is a product of three factors: the amplitude for the ν_α to be a mass eigenstate ν_i this is $U^*_{\alpha 1}$; the amplitude for the mass eigenstate ν_i to propagate from the source to the detector, $Prop(\nu_i)$; and last, the amplitude for a charged lepton created when ν_i interacts to be a lepton l_β. So it is possible to write:

$$Amp\,(\nu_\alpha \to \nu_\beta) = \sum_i U^*_{\alpha i} Prop\,(\nu_i)\, U_{\beta i} \tag{1.20}$$

The propagation term is obtained applying the Schrödinger-type equation:

$$\mid \nu_i(t)\rangle = e^{-im_i\eta} \mid \nu_i(0)\rangle \tag{1.21}$$

where m_i is the mass of ν_i ant η is the proper time in the neutrino rest frame.

In the laboratory system the phase factor (Lorentz-invariant) can be written as:

$$e^{-im_i\eta} = e^{-i(E_i t - p_i L)} \tag{1.22}$$

where t and L are the time and the distance to the origin of the neutrino, E_i and p_i respectively the energy and momentum of the neutrino. The neutrino is extremely relativistic and it propagates almost at the velocity of light. So, the phase factor of eq.1.22, using $t \simeq L$, becomes $e^{-it(E_i - p_i)}$. If ν_α has been produced with a definite momentum p, all of its mass-eigenstate components have this common momentum, the ν_i component has $E_i = \sqrt{p^2 + m_i^2} \simeq p + m_i^2/2p$, assuming that all neutrino masses m_i are small compared to the neutrino momentum. So the phase factor of eq.1.22 is approximately $e^{-i\left(m_i^2/2p\right)L}$. Combining all factors:

$$\begin{aligned} P(\nu_\alpha \to \nu_\beta) =\mid Amp(\nu_\alpha \to \nu_\beta) \mid^2 = \\ \delta_{\alpha\beta} - 4\sum_{i>j} Re\left(U^*_{\alpha i} U_{\beta i} U_{\alpha j} U^*_{\beta j}\right) \sin^2\left(\Delta m^2_{ij} L/4E\right) + \\ 2\sum_{i>j} Im\left(U^*_{\alpha i} U_{\beta i} U_{\alpha j} U^*_{\beta j}\right) \sin\left(\Delta m^2_{ij} L/2E\right) \end{aligned} \tag{1.23}$$

Where $\Delta m^2_{ij} \equiv m_i^2 - m_j^2$ is the splitting between the squared masses of ν_i and ν_j. Including the omitted factors of $\hbar$ and c, and converting L in km, and E in GeV, it is

possible to write the oscillating phase factor in the usual way:

$$\Delta m_{ij}^2 L/4E = 1.27\Delta m_{ij}^2 \left(eV^2\right) \frac{L\,(km)}{E\,(GeV)} \tag{1.24}$$

If U is not a real matrix, the probabilities for $\nu_\alpha \to \nu_\beta$ will be in general different from $\overline{\nu}_\alpha \to \overline{\nu}_\beta$, showing a clear CP violation effect in the neutrino oscillation.

Due to the fortunate fact (as confirmed by experimental results) that one mass splitting is dominant, $\Delta_{12}^2 \ll \Delta m_{23}^2 \sim \Delta m_{13}^2 = \Delta m^2$, it is possible to simplify the probability expression. For an oscillation experiment with L/E such that $\Delta m^2 L/E = \mathcal{O}(1)$ and $L/2E \ll 1$, using eq. 1.23, the oscillation probability can be expressed like:

$$P(\nu_\mu \to \nu_\tau) = \cos^4\theta_{13} \sin^2 2\theta_{23} \sin^2\left(1.27\Delta m^2 L/E\right) \tag{1.25}$$

$$P(\nu_\mu \to \nu_e) = \sin^2\theta_{23} \sin^2 2\theta_{13} \sin^2\left(1.27\Delta m^2 L/E\right) \tag{1.26}$$

In the special case, where only two mass eigenstates, and the two corresponding flavor eigenstates, are relevant, there is only one mass splitting and one mixing angle, and the oscillation probability is simplified as:

$$P(\nu_\alpha \to \nu_\beta) = \sin^2 2\theta \sin^2\left(1.27\Delta m_{ij}^2 \left(eV^2\right) \frac{L\,(km)}{E\,(GeV)}\right) \tag{1.27}$$

1.3 Experimental results

The main goals of the neutrino experiments are:

- measurement of oscillation parameters
- absolute mass measurement
- determine Majorana or Dirac type property
- determine mass hierarchy.

The first point historically started with the measurement of a deficit in the solar neutrino flux measurement, in the early '70s. A conclusive explanation was found only in the last ten years, thanks to the SNO and KamLAND experiments. Actually, all the existing neutrino data (except for the LSND experiment, which will be mentioned at the end of the chapter), can be explained in the three flavours neutrino mixing framework. Due to the experimental fact that $\Delta m_{12}^2 \ll \Delta m_{23}^2$ and the smallness of θ_{13}, the oscillation experiments, as carried out so far can be divided into measurements of:

- Δm_{12}^2 and θ_{12}, solar parameters
- Δm_{23}^2 and θ_{23}, atmospheric parameters
- θ_{13} mixing angle (limit).

The Majorana or Dirac nature of the neutrino can not be solved by the neutrino oscillation experiments, as these can not yield a measurement of the absolute neutrino mass (if we exclude the lower limit that is possible to derive from the oscillation mass splitting); in fact, it is clearly true that $max(m(\nu_i), m(\nu_j)) \geq \sqrt{\Delta m^2_{ij}})$. Dedicated experiments were developed in the past, and are designed for the future, to figure out these topics.

1.3.1 Neutrino mass limits

Absolute neutrino masses can be measured directly, studing the kinematics of weak decays, the time of flight of the neutrinos produced for example in a supernova collapse, or in indirect mode in astrophysical observations: studing the influence of neutrino mass in the different cosmological models.

In the direct measurement in the decay process (β and π decay), the neutrino mass is reconstructed from the kinematic of the charged particle using momentum and energy conservation. In this process neutrino flavour states are involved, so that different mass eigenstates can not be resolved, it is only possible to measure a superposition of the mass eigenstates, weighted by the unitary mixing matrix.

Investigating the distortion of the energy spectrum in the β-decay of ^3H near the endpoint, it is possible to obtain a limit on the "effective electric neutrino mass", defined as a combination of the neutrino mass eigenstate, weighted by the mixing parameter [10]:

$$m^2_\beta = \sum_i \mid U^2_{e1} m^2_i \mid = c^2_{13} c^2_{12} m^2_1 + c^2_{13} s^2_{12} m^2_2 + s^2_{13} m^2 \tag{1.28}$$

but the individual mass eigenstates are experimentally unresolved.

In any case this measurement, due to the smallness of m_β and the low number of events in the spectrum region of interest, requires an accurate control of the background and of the systematic effects. Up to now the best upper limit on the mass has been reached measuring the tritium β decay spectrum by the Mainz group [11] and is given by:

$$m_\beta < 2.3eV(95\%C.L.) \tag{1.29}$$

The currently upper bound on the ν_μ and ν_τ are:

$$m_{\nu_\mu} < 170keV \ (90\%C.L.) \quad m_{\nu_\tau} < 18.2MeV \ (95\%C.L.) \tag{1.30}$$

The first limit was obtained from the measurement of the muon momentum in the pion decay ($\pi^+ \to \mu\nu_\mu$) [12], and the second one from the measurement of the distribution of the effective mass of the pions in the decay $\tau \to \nu_\tau + 5\pi$ [13].

Indirect limits on the neutrino masses can be obtained from cosmological observations: precise measurements of the cosmic microwave background (CMB) and its fluctuations, can constrain the Hot Dark Matter content of the early universe; this, together with the cosmological prediction on the total number of relic neutrinos, gives a limit on the total neutrino mass: $\sum m_i = m_1 + m_2 + m_3$. The WMAP data improved this constraint to: $\sum m_i < 1.3eV$ [14].

From the observation of the large scale structure (LSS) in the universe, other bounds can be derived due to the neutrino effects on structure formation in the early universe. Combaining CMB anisotropy measurements with LSS data, the upper bound can be reduced to [15]:

$$\sum < 0.71eV \tag{1.31}$$

Other cosmological observations (e.g. galaxy clustering, Lyman α data) can confirm and improve this limit, obtaining better results than the direct measurement. However, all these cosmological limits are model-dependent, so a direct measurement as confirmation is necessary.

Finally, the studies of the neutrinoless double β decay can discriminate on the Majorana or Dirac particle question, and also give a direct measurement of the mass. For some nuclei the "standard" β decay is energetically forbidden, but not the second order weak decay process: $(A, Z) \rightarrow (A, Z+2) + 2\overline{\nu_e} + 2e^-$, the double β decay $(2\nu 2\beta - decay)$. If the neutrino is a Majorana particle, it is identical to its antiparticle, and consequently, neutrinoless $double - \beta$ decay $(0\nu 2\beta - decay)$ is permitted. The $(0\nu 2\beta - decay)$, being a two body decay (only two electrons and a heavy daughter nucleus in the final state), has a clear experimental signature: a peak on the endpoint of the continuous energy spectrum of the two electrons, produced in the four-body decay $(2\nu 2\beta decay)$. This decay gives a direct measurement of the "effective Majorana mass" for the electron neutrino defined as [10]:

$$m_{\beta\beta} = |\sum_i U_{e1}^2 m_i| = |c_{13}^2 c_{12}^2 m_1 + c_{13}^2 s_{12}^2 m_2 e^{i2\phi_2} + s_{13}^2 m_3 e^{i2\phi_3}| \tag{1.32}$$

where $\phi_{2,3}$ are the Majorana phases.

Up to now there is no evidence for the neutrino less double β decay from most experiments, only the most sensitive one claims an observation of such an event. A subgroup of the Heidelberg-Moscow collaboration published [16] a first evidence of $m_{\beta\beta}$ in the range of 0.2-0.6 eV (99.73%) C.L.), clearly, this result is still under discussion.

1.3.2 Solar neutrino parameters

The energy spectrum of the solar neutrino flux, according to the SMM (Standard Solar Model), is reported in Fig. 1.1 [17].

Since the first measurement a significant solar neutrino deficit, with respect to the expectation, was observed, the scientific community had to solve the commonly called solar neutrino problem. First measurements of the solar neutrino flux started in the '60s using a radiochemical technique.

The first one, the Homestake experiment [18], could detect the ν_e solar neutrino through the process $\nu_e + {}^{37}_{17}Cl \rightarrow {}^{37}_{18}Ar + e^-$, with a threshold of 0.814 MeV, which permits to observe mainly the spectrum of ^7Be and ^8B decays. The main contribution to the event rate for this experiment came from the high energy neutrino from ^8B, because the detection cross section increases with energy.

To confirm this unexpected results, other experiments using the radiochemical technique, were built: SAGE (in Russia)[19], GALLEX [20] and GNO[21] (located

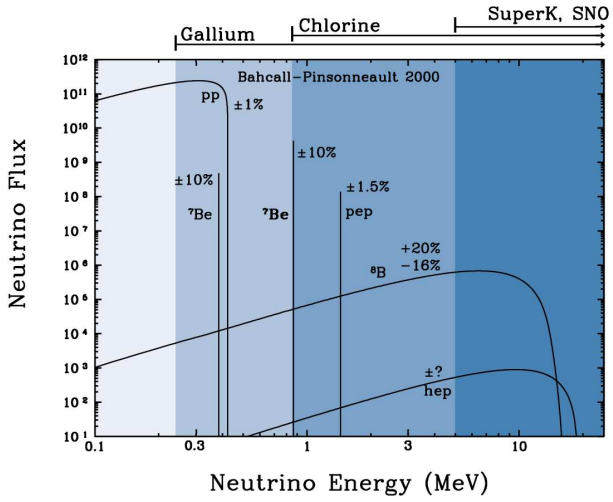

Figure 1.1: Energy spectrum of solar neutrinos.

Experiment	Running time	Flux measured	Flux expected
Homestake	1970-1994	2.56 ± 0.23	7.6 ± 1.3
GALLEX	1991-1997	77.5± 7.7	128 ± 9
SAGE	1990-2003	69.1± 5.7	128 ± 9
GNO	1998-2003	62.9± 5.9	128 ± 9
Kamiokande	1987-1995	2.80± 0.36	5.05 ± 0.9
SuperKamiokande	1996-2003	2.35± 0.036	5.05 ± 0.9

Table 1.1: Solar neutrino experiment's results. Rates measured by radiochemical experiments are expressed in Solar Neutrino Unit: $SNU = 10^{-36}$ interactions per target atom and per second, while Kamiokande and SK report neutrino fluxes in $10^6 cm^{-2} s^{-1}$.

in the Gran Sasso underground laboratory); these used a Gallium target, detecting neutrinos through the process: $\nu_e + {}^{71}Ga \rightarrow {}^{71}Ge + e^-$, with a threshold on E_ν of $0.233 MeV$). This lower threshold makes the experiments sensitive to the pp neutrino spectrum. All the result are reported in Table 1.1.

Another experiment using a different technique tried to solve the solar neutrino deficit problem: Kamiokande [22] was a 3 kton water Cherenkov detector; the big improvement of such an experiment was the possibility to take real-time data, and to reconstruct the direction of the incoming neutrino. This detector was sensitive to the elastic scattering on electrons (ES):

$$\nu_x e \rightarrow \nu_x e \tag{1.33}$$

This process is possible for all neutrino flavours, but the cross section is larger for ν_e, so it is domanited by the electron neutrino scattering. Kamiokande could measure the

energy of the outgoing electron and its direction, this, together with the energy cut, permitted to discriminate solar neutrino events from the background, that contains a comparable number of events. The flux at which the detector was sensitive, was dominated by ^8B neutrinos , and the results are included in Tab. 1.1.

This experiment was replaced by SuperKamiokande (SK) [23], a 50 kton water Cherenkov detector. It consists of two concentric, optically separated Cherenkov detectors; the inner detector was instrumented with more than 10000 PMTs, and the surface of the outer detector with 1885 PMT. The results are reported in Tab. 1.1. The real-time data taking and the possibility to measure the energy event by event permits to have some information about the possible spectral distortion, and the time fluctuations on the flux. The SK signal [24] is consistent with no spectral distortion and the absence of seasonal variations, this disfavours the vacuum oscillation solution, leaving as only unique possibility to fit the solar neutrino oscillation data to include the matter effect.

Matter effects could also affect the day/night ratio of the measured flux, in fact, during the night the solar neutrinos cross the earth before they reach the detector. The measured absence of a day/night asymmetry is compatible with the MSW effect with Large Mixing Angle (LMA) parameter [24].

The final model independent proof of neutrino oscillations as the reason for the solar neutrino deficit came from the SNO [25] experiment, a Cherenkov detector with a fiducial volume of 1 kton filled with heavy-water, surrounded by water, used as shielding. The SNO detects ^8B neutrinos through three reactions:

$$\begin{aligned} &\nu_e + d \to p + p + e^- \qquad (dCC) \\ &\nu_\alpha + d \to p + n + \nu_\alpha \qquad (dNC) \\ &\nu_\alpha + e^- \to \nu_\alpha + e^- \qquad (ES) \end{aligned} \tag{1.34}$$

The last reaction, as in SK, is sensitive to all neutrino flavours and can not distinguish between them; the first one is a charged current (CC) interaction provided only by the ν_e, and is sensitive only to the ν_e flux; the second one is instead provided by all the neutrino flavours with equal cross section, it is sensitive to the total neutrino flux $\Phi_{NC} = \Phi_e + \Phi_{\mu\tau}$. If the Standard Solar Model is correct, the predicted flux Φ_{SSM} must be equal to the total flux Φ_{NC}, and is independent of oscillations; on the other hand, the ratio $\Phi_{CC}/\Phi NC$ is proportional to the survival probability of ν_e, and it is independent of the SSM.

The SNO experiement was running in differents periods and conditions, the results of the last phase (compatible with the oldest result) were published in [26], the neutrino fluxes derived from the CC, NC and ES events are (in units of $10^6 cm^{-2} s^{-1}$):

$$\begin{aligned} \Phi_{CC}^{SNO} &= 1.67^{+0.05}_{-0.04}(stat)^{+0.07}_{-0.08}(syst) \\ \Phi_{ES}^{SNO} &= 1.77^{+0.24}_{-0.21}(stat)^{+0.09}_{-0.10}(syst) \\ \Phi_{NC}^{SNO} &= 5.54^{+0.33}_{-0.31}(stat)^{+0.36}_{-0.34}(syst) \end{aligned} \tag{1.35}$$

and the ratio of th ^8B neutrino flux measured with CC and NC interactions is:

$$\frac{\Phi_{CC}^{SNO}}{\Phi_{NC}^{SNO}} = 0.301 \pm 0.0033(total) \tag{1.36}$$

Finally, the total Φ_{NC} flux is in good agreement with the expected SSM prediction of the flux of ^8B neutrino: $(5.05^{+1.01}_{-0.81} \times 10^6 cm^{-2} s^{-1})$.

A change of the neutrino flavor does not change the total neutrino flux, so the compatibility of the Φ_{NC} flux with the expected one, together with the result on the ratio, are considered as the final confirmation of neutrino oscillations in the solar sector, and they are the proof that the neutrino production chain in the sun is correctly described by the SSM. SNO also confirmed that the strongly favoured explanation of solar neutrino flavor change is the LMA-MSW effect.

The last confirmation of $\overline{\nu}_e$ oscillations, by the distortion of the energy spectrum, was given by the KamLAND experiment, a long base-line anti-neutrino reactor experiment. It is a detector using 1 kton of liquid scintillator, surrounded by inert oil as shielding. It can detect the $\overline{\nu}_e$ emitted by 16 Japanese reactors, at different distances, via the process: $\overline{\nu}_e + p \rightarrow e^+ + n$, the signature of the events is given by the detection of the positron and the 2.2 MeV γ produced by the neutron capture. This experiment reported the first evidence for $\overline{\nu}_e$ disappearance [27]: with no oscillation they expect $2179 \pm 89(syst)$ events from the reactors, and 276.1 ± 23.5 background events in the interesting energy region, (not taking into account geo-neutrino events), they observed only 1609 events. Fig 1.2 shows the prompt energy spectrum of selected $\overline{\nu}_e$ events, and fitted backgrounds: these results and the constraints on the oscillation parameters obtained, are compatible with the solar neutrino experiments, previously described.

More important is that KamLAND has the possibility to estimate the survival probability of $\overline{\nu}_e$, depending on the neutrino energy, to test the oscillation model. The ratio of the background-subtracted $\overline{\nu}_e$ candidate events, including the subtraction of geo-neutrinos, to no-oscillation expectation is shown in Fig 1.2 as function of L_0/E. This rules out an undistorted spectrum at more than 5σ, and shows a clear oscillation pattern (almost two cycles), in excellent agreement with the neutrino oscillation hypothesis.

A complete combined analysis of the solar neutrino oscillation parameters is reported in [43], it includes the latest data of SNO and KamLAND, the results of all radiochemical experiments, and also data from the Borexino experiment [28]. Fig 1.3 illustrates the oscillation parameters obtained by this analysis: from the global three-flavour analysis one finds (1σ errors):

$$\theta_{12} = 0.304^{+0.022}_{-0.016} \qquad \Delta m^2_{12} = 7.65^{+0.23}_{-0.20} \times 10^{-5} eV^2 \tag{1.37}$$

1.3.3 Atmospheric neutrino parameters

Atmospheric neutrinos are generated by interactions of primary cosmic rays with nuclei in the upper atmosphere; the decay of charged π or K generate μ^-, μ^+ and ν_μ, $\overline{\nu_\mu}$; the subsequent muon decays generate muon and electron neutrinos. The absolute

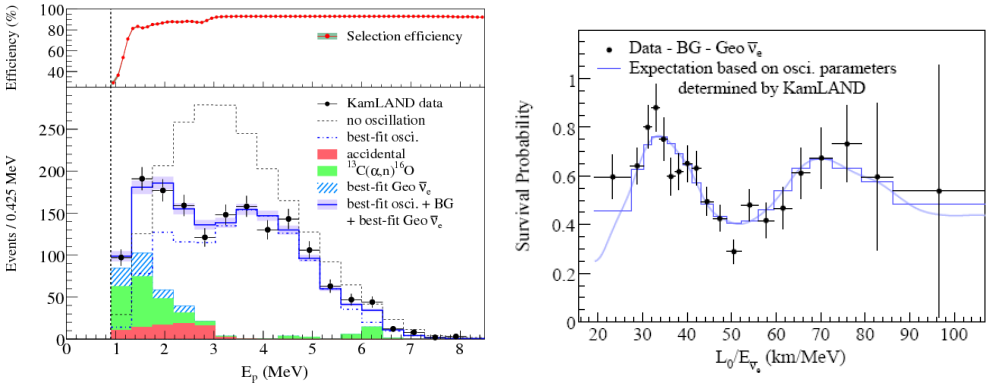

(a) (b)

Figure 1.2: On the left prompt energy spectrum of $\overline{\nu}_e$ candidate events in the KamLAND experiment. All histograms corresponding to reactor spectra and expected backgrounds incorporate the energy dependent selection efficiency(top). On the right: ratio of the background subtracted $\overline{\nu}_e$ spectrum to the expectation without oscillation as a function of L_0/E. L_0 is the effective baseline taken as a flux weighted average ($L_0 = 180\ km$). The error bars include the statistical uncertainty only [27].

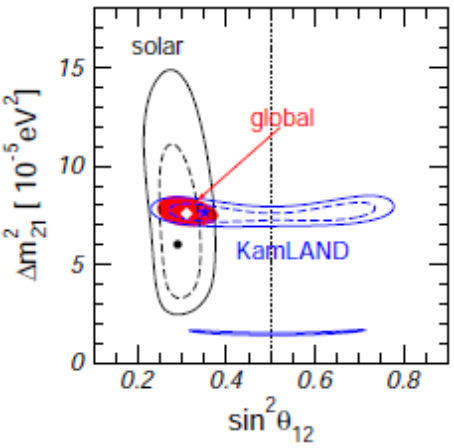

Figure 1.3: Determination of the leading "solar" oscillation parameters from the interplay of data from artificial and natural neutrino sources [43].

flux is not well-known, but the ratio $R = (\nu_\mu + \overline{\nu}_\mu)/(\nu_e + \overline{\nu}_e)$ is expected to be ~ 2 (at low energy $E < 1\ GeV$), with an estimated theoretical uncertainty of 5%, for E_ν $0.1 - 10\ GeV$ [6], and isotropically distributed.

The measurement of the ratio R has been performed by many experiments: Kamiokande [22], IMB [31] and Soudan [32], all of them found an anomalous value of R, showing a deficit of ν_μ with respect to ν_e, but the origin of this deficit was not determined. The

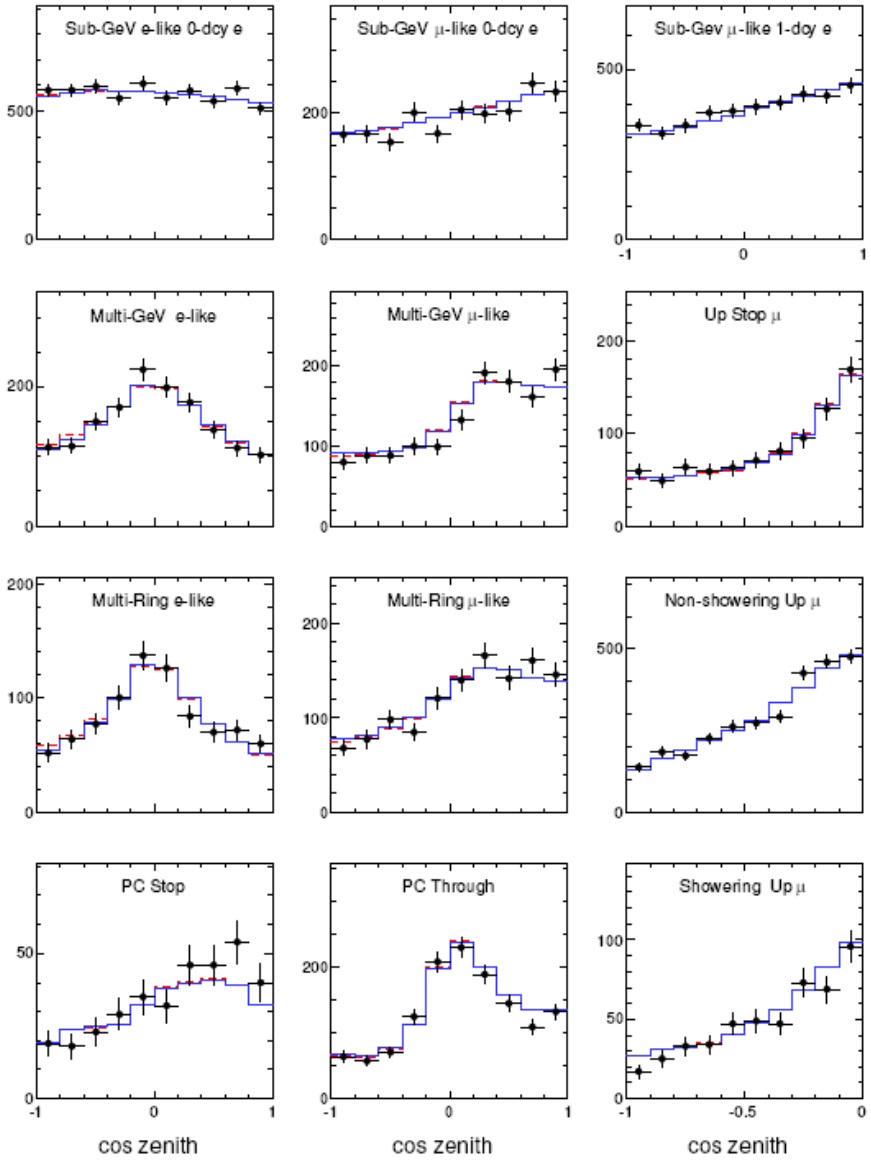

Figure 1.4: SK-I+II+III number of events as function of the zenith angle of the different event samples, black dots represent the data with statistical errors, the solid line the MC expectation at the best fit [33].

crucial results were obtained by the SK experiment, because it is able to reconstruct the most probable direction of the incoming atmospheric neutrino, and its energy. It reported already in 1998 that this low ratio was due to a deficit of ν_μ coming from below, in fact it measured an up-down asymmetry of the muon neutrino flux of [49]:

$$A_\mu^{up-down} = -0.29 \pm 0.048 \pm 0.01 \tag{1.38}$$

Further confirmation came from the observation illustrated in Fig. 1.4 of the neutrino flux as a function of the direction (zenith angle of the incoming neutrino), for the different samples of electron and muon neutrinos and for partially an fully contained events at different total visible energy (the figure reports the latest result of the SK collaboration, including the SK phase I-II-II). The SK collaboration defines as fully-contained the electron or muon events where the scattered outgoing lepton ends inside the fiducial volume of the detector, so it is possible to have a clear measurement of its energy, with a better angular resolution for the high energy events. The muon events not contained in the detector are divided in: partially-contained if they are scattered inside the detector but escape from it; up-going stopping if the μ is produced in the rock below the detector and they stop inside and through-going up if they are produced below the detector and they cross and escape from it.

Looking at the SK results, it is clear that the distributions for the muon events are strongly asymmetric with respect to the cosine of the zenith angle, while the distributions for electron events are symmetric (except PC stopping), and compatible with no oscillation. These data can be explained by the neutrino oscillation theory with a dominant $\nu_\mu \to \nu_\tau$ flavour change and a possible minor contribution due to the $\nu_\mu \to \nu_e$ channel [33].

The atmospheric neutrinos cover a wide range of energy and path lengths, this permits to prove the energy dependence of the oscillation probability and confirms the neutrino oscillation as the reason of the deficit of muon neutrinos. The distribution of the ratio of the data and the MC prediction for no oscillation for the number of μ-events as a function of the L/E, shown in Fig. 1.5, clearly shows the oscillation pattern as a function of L/E.

To confirm and improve the knowledge of the ν_μ-disappearance due to oscillations, two long-baseline experiments were performed, using neutrino beams produced at the accelerators: K2K in Japan [35] and MINOS [34] at Fermilab. For both a small near detector was designed to study the no-oscillation spectrum ($\Delta m^2 L_{near}/E \ll 1$), and to have a good knowledge of the systematic uncertainties. K2K was designed with a ν_μ beam of $\langle E_\nu \rangle \sim 1.4\ GeV$, the far detector was SK at a distance of 250 km. MINOS has a mean beam energy of 4 GeV and a baseline of 735 km. The results of both experiments are consistent with a clear energy dependence of the ν_μ disappearance, compatible with the oscillation expectation.

The definite confirmation of the $\nu_\mu \to \nu_\tau$ hypothesis could be obtained by an appearance experiment, that can measure the appearance of a ν_τ signal in a pure ν_μ beam produced by an accelerator, the OPERA experiment is designed to probe this.

The analysis of the atmospheric neutrino sector gives a measurement of the $\Delta m^2_{13} \sim \Delta m^2_{23}$ and $\sin^2\theta_{23}$ parameters; the most stringent constraints to these parameters are obtained by the SK and MINOS experiments, including the latest MINOS results [36],

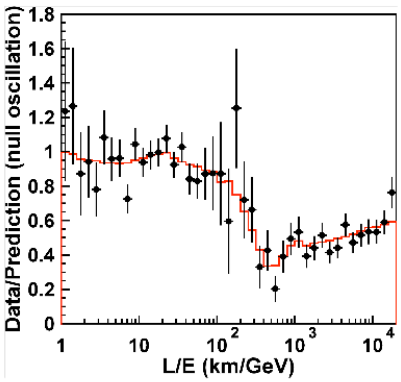

Figure 1.5: The ratio of the observed muon-like events in SK to no-oscillation MC-predictions, versus the reconstructed neutrino path-length-to-energy ratio (L/E)

the best fit of the oscillation parameters for the atmospheric sector gives the following value [43]:

$$\sin^2_{23}((2\theta) > 0.90(90\%C.L.) \qquad \Delta m^2 = \Delta m^2_{23} = (2.43 \pm 0.13) \times 10^{-3} eV^2 \qquad (1.39)$$

The confirmation that the atmospheric neutrino deficit is not due to the $\nu_\mu \to \nu_e$ oscillation is given by the result of SK that did not observe ν_e appearance and by the CHOOZ experiment.

CHOOZ was a short-baseline reactor experiment [37], looking for disappearance of $\overline{\nu_e}$ emitted by two nuclear reactors, with mean energy of few MeV, located at distance of $L \sim 1\ km$. The CHOOZ detector consisted of 5 tons of liquid scintillator in which neutrinos were revealed through the inverse β-decay reaction ($\overline{\nu}_e + p \to n + e^+$) with a threshold of $E_{th} = 1.8 MeV$. The main result of CHOOZ was a strict direct constraint on the θ_{13} parameter, that depends on the value of the Δm^2_{23}.

In the picture of three neutrino mixing, this angle represents the sub-dominant channel of $\nu_\mu$oscillation, if it is null, atmospheric and solar oscillations don't interplay. Due to the fact that the CHOOZ experiment didn't observe disappearance of $\overline{\nu}_e$ (the ratio between measured and expected $\overline{\nu}_e$ events was: $R = 1.01 \pm 0.028 \pm 0.027$), considering $\Delta m^2_{23} > 2 \times 10^{-3} eV$, the mixing angle is confined to be [37]:

$$\sin^2_{13}(2\theta) < 0.1 \qquad (90\%C.L.) \qquad (1.40)$$

LSND and MiniBoone

Many short baseline experiments were developed in the last three decades, to study different neutrino oscillation channels, none found any indication of neutrino oscillations, except LSND. LSND was designed to study the $\overline{\nu}_\mu \to \overline{\nu}_e$ oscillations, it found an excess of $\overline{\nu}_e$ events compatible with a $\Delta m^2_{23} \sim 0.1 - 1 eV^2$ [38].

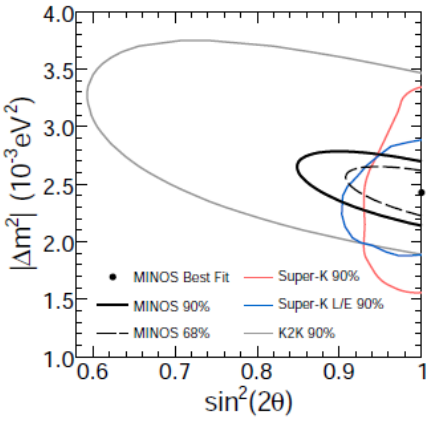

Figure 1.6: The allowed region in the atmospheric oscillation parameter space from SK, K2K, MINOS at 90% (solid black) and 68% (dashed black) confidence level is plotted[36].

Clearly, this mass splitting is not compatible with the other two mass splittings already measured. To include the LSND result in the oscillation picture, it is necessary to add another neutrino, a sterile one, that can not weakly interact. KARMEN [39] was built to verify the result of LSND, it didn't find any signal, but it was not able to exclude completely the oscillation parameter region allowed by LSND.

MiniBooNE [40] is an experiment running at Fermilab, it should solve the LSND-puzzle; it is located at 541 m from the front of the target of the Fermilab neutrino beam. The latest result published by MiniBooNE [41] reported the analysis for the events collected in the neutrino and antineutrino mode; for the first case no evidence for an excess of ν_e candidate events above 475 MeV was found, but they claim a 3.0σ signal of electron-like events observed below 475 MeV. The source of this excess remains unexplained, several hypotheses have been considered, including non-standard reactions and sterile neutrino oscillation. In the antineutrino mode the results are consistent with $\overline{\nu}_\mu \to \overline{\nu}_e$ oscillations from LSND.

1.3.4 Global analysis and future perspectives

The experimental neutrino oscillation data can be described within a three-flavour neutrino oscillation framework, excluding LSND and MiniBoone results. This framework is characterized by two mass-squared differences, that are simply associated to the atmospheric and solar oscillations , and three mixing angles. An analysis of all these neutrino data can be found in [43], the best values for the known parameters are:

parameter	*best fit*	2σ	3σ
Δm^2_{21}	$7.59^{+0.23}_{-0.28} \times 10^{-5} eV^2$	$7 - 22 - 8.03$	$7.03 - 8.27$
Δm^2_{31}	$2.40^{+0.12}_{-0.11} \times 10^{-3} eV^2$	$2.18 - 2.64$	$2.07 - 2.75$
$\sin^2\theta_{12}$	$0.318^{+0.019}_{-0.016}$	$0.29 - 0.36$	$0.27 - 0.38$
$\sin^2\theta_{23}$	$0.50^{+0.07}_{0.06}$	$0.39 - 0.63$	$0.36 - 0.67$

(1.41)

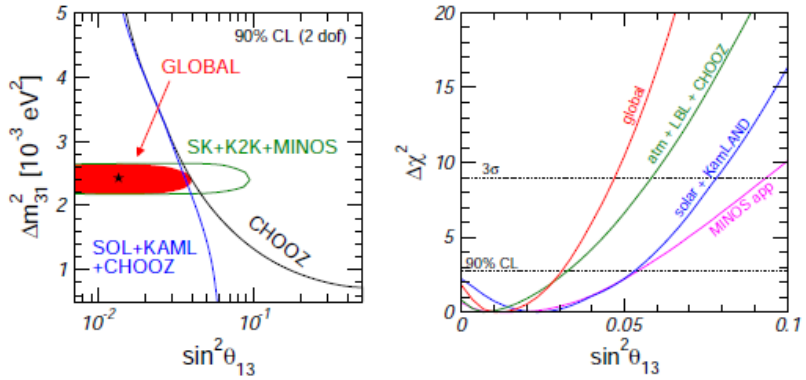

Figure 1.7: Constraints on $\sin 2\theta_{13}$ from different parts of the global data [44].

The most important contribution to the upper limit of θ_{13} comes from the non-observation of disappearance of reactor electron anti-neutrinos at the CHOOZ and Palo Verde [16] experiments. Including solar and atmospheric experiments more strict constraints can be obtained for this angle as we can see in Fig. 1.7; the constraint of θ_{13} can be summarized [43, 44] as:

$$\sin^2\theta_{13} \leq \begin{cases} 0.053(0.078) & (solar + KamLAND) \\ 0.033(0.061) & (CHOOZ + atm + K2K + MINOS) \\ 0.034(0.053) & (global\ data) \end{cases} \tag{1.42}$$

The global analyses about the constraints on the θ_{13} converge to a weak hint of a non-zero value for θ_{13}, the best fit value with 1σ range (see also [45]) is :

$$\sin^2\theta_{13} = 0.013^{+0.013}_{-0.009} \tag{1.43}$$

To prove of a non-zero value of θ_{13} is crucial for the neutrino theory because it is a necessary prerequisite for leptonic CP violation, and to probe the mass hierarchy via ν interactions in the Earth and to discriminate the different theoretical models for the neutrino mass matrix [45].

Up to now, due to the small (still compatible with null) value of the θ_{13} angle, the CP phase δ and the mass hierarchy (see below) are currently not constrained. Since we obtained from the oscillation experiments only measurements of the mass splitting, it is not possible to determine the absolute scale of the neutrino mass; it is still possible to have $m_3^2 \geq m_1^2$ (*normal hierarchy*) or $m_3^2 < m_1^2$ (*inverted hierarchy*), as represented in Fig. 1.8.

Therefore, the determination of θ_{13} and the determination of the mass hierarchy are among the main goals for the future experiments. The most promising way to distinguish these two neutrino mass hierarchies is to search for the matter effect in transitions, involving Δm^2_{31}. The condition for an MSW resonance is:

$$\cos 2\theta_{13} = \pm\frac{2E_\nu V}{\Delta m^2_{31}} \tag{1.44}$$

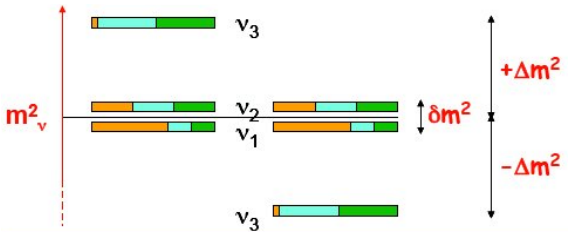

Figure 1.8: The two three-neutrino schemes allowed by the hierarchy $\Delta m^2_{sol} \ll \Delta m^2_{atm}$, called normal ($m_3 > m_{1,2}$) and inverted ($m_3 < m_{1,2}$).

where + (-) holds for (anti)neutrinos. For a given sign of Δm^2_{13} this equation can be fulfilled either for neutrinos or for anti-neutrinos. Therefore, finding out whether the matter resonance due to this mass splitting occurs for neutrinos or anti-neutrinos a determination of the sign of Δm^2 [44] will be provided.

To give an answer to these problems many experiments have been developed. T2K [46] uses a high intensity off-axis (2.5°) neutrino beam, with a peak energy of 700MeV, generated by a 30 GeV proton beam produced at J-PARC (Japan Proton Accelerator Research Complex). The ν_μ beam is directed towards the SuperKamiokande detector, located 295 km from the proton beam target. A near detector has been built at a distance of 280 m from the target, measuring the unoscillated neutrino flux, which can be extrapolated to SK.

The goals of T2K are a more precise determination of the atmospheric oscillation parameters θ_{23} and Δm_{23} from the ν_μ disappearance measurement and the search for ν_e appearance from $\nu_\mu \rightarrow \nu_e$ oscillation to measure θ_{13}.

New reactor experiments are in an advanced state of construction: Double CHOOZ, Daya Bay, RENO. The Double Chooz experiment [47] is being installed near the Chooz two-core nuclear power plant in France. It includes a far detector, at 1.05 km from the two reactor cores, and an identical near one placed 400 m from the two reactors. They consist of concentric cylinders loaded with liquid scintillator.

The Daya Bay experiment [48] in China is installed to observe the neutrino flux from three nuclear plants. The experiment is made of eight identical liquid scintillator antineutrino detectors in three underground experimental halls.

1.4 Neutrino interactions

In the oscillation experiments the monitoring of the neutrino flux and the number of expected interactions is absolutely mandatory; to do this a good knowledge of the neutrino interactions with matter is necessary. For the neutrino oscillation experiments the processes involved are mainly the neutrino-nucleon scattering, and they are well described the by Standard Model [49].

- Charged Current (CC): wherein a charge change of the lepton occurs when a neutron (proton) of the target nucleus changes into a proton (neutron) for ν ($\overline{\nu}$) interactions; the interaction occurs via the exchange of a W-boson. Even though

the generated charged leptons can go in every direction, statistically they point in the direction of the incident neutrino.

- Neutral Current (NC): wherein the neutrino interacts with the nucleons (protons and neutrons) by exchange of a Z-boson.

The cross section for the CC neutrino interaction as function of energy is shown in Fig. 1.9. The main processes in the energy range of about a GeV up to 100 GeV are: quasi-elastic (QE) and resonance (RES) reactions, deep inelastic scattering (DIS) [50, 51, 52].

- *Quasi-elastic*:

$$\begin{aligned} &\nu_\mu + n \to p + \mu^- \quad (CC) \\ &\overline{\nu}_\mu + p \to n + \mu^+ \quad (CC) \end{aligned} \tag{1.45}$$

  This process dominates the low energy region: $E_\nu \approx \ GeV$ (see Fig. 1.9.)

- *Resonance*: the neutrino interactions arise through the excitation of a baryon resonance which then decays to a nucleon-pion final state:

$$\nu_\mu + N \to l + N^* \qquad N^* \to \pi N'$$

  where $N, N' = n, p$. There are seven possible resonant single pion production channels, three CC:

$$\begin{aligned} &\nu_\mu + p \to \mu^- p \pi^+ \\ &\nu_\mu + n \to \mu^- + p \pi^0 \\ &\nu_\mu + n \to \mu^- + n + \pi^+ \end{aligned} \tag{1.46}$$

  and four NC :

$$\begin{aligned} &\nu_\mu + p \to \nu_\mu + p \pi^0 \\ &\nu_\mu + p \to \nu_\mu + n \pi^+ \\ &\nu_\mu + n \to \nu_\mu + n + \pi^0 \\ &\nu_\mu + n \to \nu_\mu + p + \pi^- \end{aligned} \tag{1.47}$$

  Early experiments on these interaction channels involved in particular light targets (deutrium and hydrogen) for the CC interactions, the results for the NC channel were really limited. In the NC channel new measurements come from the MiniBoone experiment. In any case nuclear effects further complicate the description of this kind of interactions, and increase the uncertainties of knowledge of the cross section. The total cross section in the few GeV range, dominated by quasi-elastic and resonance processes, is known with a precison of $\sim 10\%$ [50].

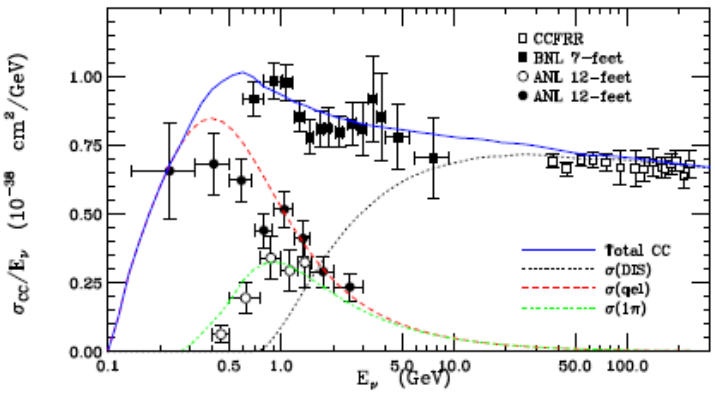

Figure 1.9: Normalized charge current neutrino cross section as function of the energy (in GeV). The contribution of DIS (dotted), QE (dashed) and single-pion(dot-dash) are shown [50].

- *Deep-inelastic scattering (DIS).* The ν scatters off a quark in the nucleon via exchange of a virtual W or Z boson; inducing the break-up of the nucleon. The CC channels are given by the following equations:

$$\nu_\mu + N \rightarrow \mu + X \tag{1.48}$$

and NC channels by:

$$\nu_\mu + N \rightarrow \nu_\mu + X \tag{1.49}$$

The cross section is given by:

$$\frac{d^2\sigma_\nu^{\nu(\overline{\nu})}}{dxdy} = \frac{G_F^2 M E_\nu}{\pi\left(1+\frac{Q^2}{M_W^2}\right)^2}\left[\left(1-y-\frac{Mxy}{2E_\nu}\right)F_2 + \frac{y^2}{2}2xF_1 \pm y\left(1-\frac{y}{2}\right)xF_3\right] \tag{1.50}$$

where G_F is the weak Fermi coupling constant, M is the nucleon mass, E_ν the neutrino incident energy in the laboratoy frame, Q^2 the four momentum transfer, ν the energy transfer in the laboratory frame and x and y the usual Bjoerken scaling variable and the inelasticity defined as: $x = \frac{Q^2}{2M\nu}$ and $y = \nu/E_\nu$. The F_1, F_2, F_3 represent the structure functions and contain direct information on the nucleon structure. Also taking into account the nuclear effects this cross section is well known, with an uncertainty of $\sim 2\%$. The DIS interactions dominate in the neutrino energy range E_ν bigger than a few GeV (see Fig. 1.9).

The total cross section for the CC neutrino interaction as function of energy is shown in Fig. 1.9.

Chapter 2

The OPERA experiment

The result of SK [24] on atmospheric neutrinos, confirmed by the accelerator experiments K2K [35] and MINOS [36], are in agreement with the theory of neutrino oscillations. The OPERA [53] experiment (Oscillation Project with Emulsion-tRacking Apparatus) is a long-baseline neutrino experiment, to search for direct evidence of $\nu_\mu \rightarrow \nu_\tau$ oscillation. The τ neutrino (produced in a charged current interaction), is identified studying the different decay topologies of the τ lepton . The τ decay modes are:

$$\begin{array}{ll} \tau \rightarrow e^- \nu_\tau \overline{\nu}_e & BR \sim 18\% \\ \tau \rightarrow \mu^- \nu_\tau \overline{\nu}_\mu & BR \sim 17\% \\ \tau \rightarrow h^- \nu_\tau (n\pi^0) & BR \sim 50\% \\ \tau \rightarrow 3\pi^{+/-} \nu_\tau (n\pi^0) & BR \sim 14\% \end{array} \tag{2.1}$$

where h^- stands for a negatively charged hadron. The lifetime of the τ is $(290.6 \pm 1.0) \times 10^{-15} s$ ($c_\tau = 87 \mu m$), thus, it has a very short decay length. This means that the τ detection requires a high spatial resolution. On the other hand, the neutrino interaction cross section is really small, so that a large target mass experiment is needed. OPERA is a hybrid detector, described in section 2.2, fulfilling those two different requirements. It is located in the Gran Sasso Underground Laboratory, 730 km far from CERN, where the ν_μ beam is produced, as described in section 2.1.

The placement of the detector in the underground laboratory at LNGS [54], with a mean amount of 1400 m of rock overburden, permits to reduce the cosmic ray background, that is a really important requirement for this kind of experiment.

2.1 The CNGS beam

The CNGS neutrino beam [55, 56] is generated from a 400 GeV proton beam extracted from the CERN SPS, hitting a target consisting of a series of thin graphite rods. As sketched in Fig 2.1 the secondary particles, produced by the proton interactions in the target, are mainly π's and K's. The positively charged particles are energy selected and focused into a parallel beam by a system of two magnetic lenses, called horn and

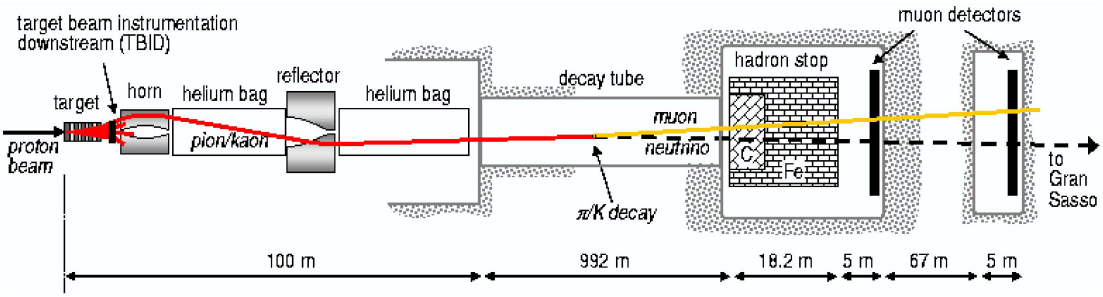

Figure 2.1: Schematic outline of the main components of the the CNGS beam line [55].

ν_μ	$95.9\% \pm 0.07\%$
$\overline{\nu}_\mu$	$3.5\% \pm 0.07\%$
ν_e	$0.5\% \pm 0.003\%$
$\overline{\nu}_e$	$0.1\% \pm 0.001\%$

Table 2.1: Expected contamination of the CNGS beam [55]

reflector. Then, in the 1 km long decay-pipe, the pions and kaons decay into ν_μ and μ. The remaining hadrons (protons, pions, kaons,...) are absorbed by an iron beam-dump. Beyond the hadron stop and after 67 m of rock two silicon muon detectors are placed to monitor and to tune the beam.

The proton beam has a nominal intensity of 4.8×10^{13} $p.o.t$ (proton on target) for each cycle; a CNGS cycle lasts 6 s, including two SPS extractions separated by 50 ms, each one corresponding to a pulse of 10.5 μs.

The neutrino beam reaches Gran Sasso, 730 km from CERN, in about 2.4 ms, and a transverse FWHM about 3 km. Due to the Earth's curvature neutrinos from CERN enter the LNGS halls from below with an angle of about 3° with respect to the horizontal plane.

The average neutrino energy at LNGS is $\langle E \rangle \sim 17$ GeV, the contaminations due to the decay of negative pions and kaons, not selected by the magnetic lens, producing $\overline{\nu}_\mu$, and due to the decay of K^+ ($K^+ \to \pi^0 + e^+ + \nu_e$), producing ν_e, and the decay of K^- producing $\overline{\nu}_e$, are summarize in Table 2.1. The contamination due to decays of D_s^+ producing ν_τ is negligible [55].

The beam is tuned to optimize the detection of τ at the LNGS laboratory, as is illustrated in Fig. 2.2; the number of ν_τ CC interactions in the OPERA target times the τ detection efficiency is optimized:

$$R_\tau = M_{target} \times \int dE_\nu P_{\nu_\mu \to \nu_\tau} \Phi \frac{d\sigma}{dE_\nu} \epsilon_\tau(E_\nu) \tag{2.2}$$

where:

- $P_{\nu_\mu \to \nu_\tau}$ is the oscillation probability. Considering the neutrino oscillations in the

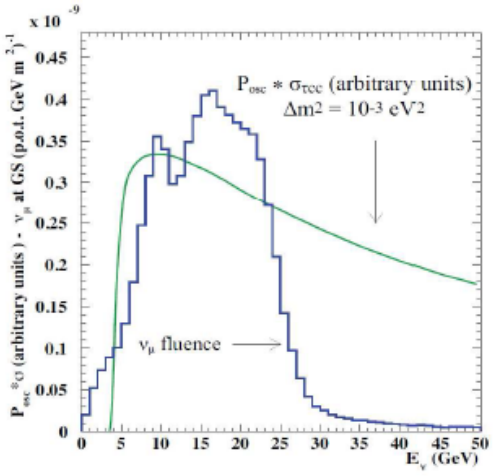

Figure 2.2: Optimization of the neutrino flux energy considering the probability of oscillation and the cross section of $\nu_\tau CC$ interactions, for a baseline of the beam of 732 km and $\Delta m^2_{23} = 3 \times 10^{-3} eV^2$ [55].

two-neutrino approximation it can be written as

$$P_{\nu_\mu \to \nu_\tau} = \sin^2 2\theta_{23} \times \sin^2(1.27 \Delta m^2_{23} L/E) \quad , \tag{2.3}$$

it favours small energies or a long baseline.

- $\frac{d\sigma}{dE_\nu}(E_\nu)$ is the cross section of the ν_τ, for the production of a τ. The threshold of 3.5 GeV is required.
- Φ is the ν_μ flux at LNGS.
- $\epsilon_\tau(E_\nu)$ is the τ detection efficiency of the OPERA detector.
- M_{target} is the mass of the detector.

Given a target mass of 1.25 kt for the OPERA detector and counting the detection efficiencies for τ decay channels, about 10 reconstructed τ events are expected to be observed after 5 years of nominal beam, see section 2.4.

2.2 The OPERA detector

The requirements of the τ decay detection and of a high target mass to increase the number of neutrino interactions are fulfilled by the hybrid detector. It includes active electronic detectors, used to select the beam events and the neutrino interactions, and a high resolution tracking device, which is realized by the ECC modules [53]. The ECC (Emulsion Cloud Chamber) technique was already used in experiments like DONUT [3] and CHORUS [57], and it was implemented in OPERA in the target units, called bricks, as explained in section 2.2.1.

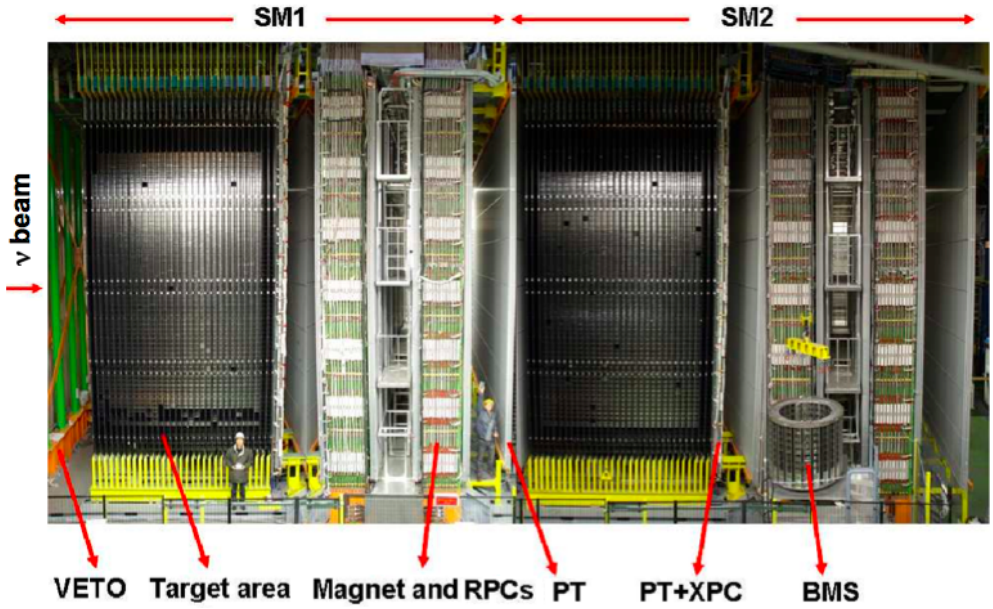

Figure 2.3: View of the OPERA detector. The two identical Super Modules (SM1 and SM2) are visible. The neutrino beam enters from the left side through the so called VETO planes.

The OPERA apparatus consists of two identical Super Modules as shown in Fig. 2.3. Each SM contains about 75000 lead/emulsion bricks, arranged in 31 target planes, each one followed by two scintillator planes (Target Tracker).

A magnetic spectrometer is placed after the target section of each SM, it is composed of two arms, each one with 12 iron slabs, interleaved by 11 Resistive Plate Chambers (RPC). Before, after and between each RPC arm a station of vertical drift tubes (Precision Trackers, PT) permits an accurate measurement of the curvature of the charged particles. Moreover, XPCs, additional inclined RPC planes located directly in front of the magnet, improve the measurement of the angular resolution and resolve ambiguities. Two additional glass RPC planes (VETO) are mounted in front of the detector to tag the charged particles originating from outside the target, due to neutrino interactions in the surrounding (rock) material.

The total detector has a length of 20 m, is 10 m high and 10 m wide; in Fig. 2.3 a picture of the detector with the different components is shown; the neutrino beam enters from the left.

The construction of the experiment started in Spring 2003. The first instrumented magnet was completed in May 2004 together with the first half of the target support structure. The second magnet was completed in the beginning of 2005. In Spring 2006 all scintillator planes were installed. The production of the ECC bricks started in October 2006 with the aim of completing half of the target for the run of October 2007. Since 2008 the target is completely filled and the beam is running in the high-intensity mode.

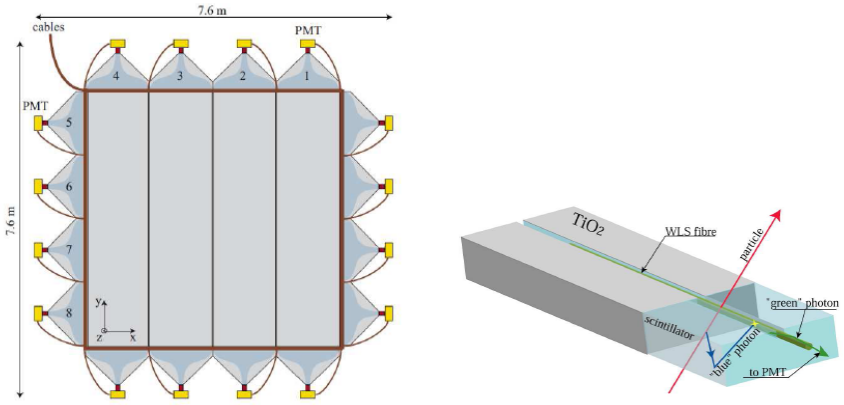

(a) (b)

Figure 2.4: Schematic view of the two scintillator planes of a TT wall on the left, and a schematic view of a scintillator strip with the wave length shifting fibers on the right.

2.2.1 The target

Each target consists of 31 brick walls interleaved with scintillator walls, the Target Tracker (TT). A total amount of 150 036 bricks have been inserted in the OPERA detector, for a mass of ~ 1.25 *kton* of instrumented target for the τ detection.

OPERA bricks are placed inside the target with the Brick Manipulating System (BMS) from each side of the experiment. A dedicated brick support structure was designed to contain the bricks and at the same time to permit their insertion and extraction from the target. The BMS extracts the entire row of bricks, selects the one that has to be analyzed and reinserts the others. The BMS procedures are possible during the beam run.

The Target Tracker

Each TT wall consists of two scintillator planes with strips oriented along the X (horizontal) and Y (vertical) axis, with a total size of $6.7 \times 6.7\ m^2$. A plane is divided into 4 horizontal and 4 vertical units, it is made of a collection of 4 subunits including 16 strips each. The strip has a length of 6.7 m, a width of 2.7 cm and a thickness of 1 cm, see Fig. 2.4. Altogether there are 256 plastic scintillator readout strips for each plane. The unit is read out with a 64-pixel Hamamatsu H7546 multi anode photo multiplier tube (m-PMT), connected to the strips using wavelength shifting fibers. In total the OPERA detector is instrumented with 31'744 strips and 992 m-PMT's. The reconstructed position accuracy reached with the TT is ~ 1 cm.

The main goals of the analysis of the TT data are:

- trigger on the beam events;
- localize the brick in which the neutrino interaction occurred;
- give an estimation of the hadronic energy of the event, using TT as a calorimeter.

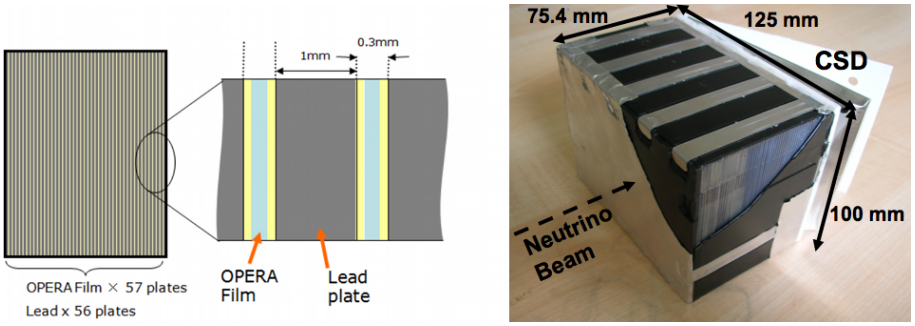

Figure 2.5: The OPERA ECC brick. On the left side a sketch of a lead/emulsion sandwich is shown. On the right side a photograph of an OPERA brick with the aluminium cover partially removed is shown; CSD is the CS doublet (see text).

The ECC

The basic unit of the OPERA experiment is the ECC; it can be considered as a stand-alone detector, that is extracted from OPERA and analyzed when an interaction is found occurring inside it. The brick (ECC) consists of 56 lead plates, 1 mm thick, interleaved by 57 emulsion films, packed together in a plastic box as shown in Fig. 2.5. The total weight of a brick is 8.3 kg with a size of: 12.8 $cm \times 10.2$ cm for the transverse plane (with respect to the beam), and 7.9 cm in the longitudinal direction.

The transverse dimensions have to fit some conflicting requirements: due to the fact that, once analyzed, the brick is no longer usable, the mass of the brick has to be small to limit the loss of target mass during the experiment. On the other hand the electron and γ identification requires about $3 - 4$ X_0 (radiation length) to distinguish the particles, and the measurement of the particle momentum (with multiple scattering) is possible over a length of more than $5X_0$ for a particle with momentum ≤ 6 GeV/c. The length of the brick is 7.9 cm, corresponding to about $10X_0$, and fulfils all the previous requirements. Moreover, this length permits to contain the neutrino events in one brick in most cases, so that it is enough to extract one brick/event.

Inside the brick, lead as passive material has been chosen due to its high density, that permits to have a big detector mass and to contain about 10 radiation lengths in a short distance.

However, lead has some radioactive isotopes that can create tracks in the emulsions, and this increases the background track level in the films, limiting their life-time as good detectors. Hence, a low radioactivity lead has been selected [60], and ~ 10 α and 50 β tracks/$(day * cm^2)$ are estimated as expected background, leading to a mismatch of low energy tracks of $\sim 1/mm^2$.

The main tracker detectors in OPERA are the emulsion films [58, 59], made of two sensitive emulsion layers of 44 μm thickness (respectively called top and bottom layer) on both sides of a transparent plastic base with a thickness of 205 μm; the dimension of the films are 12.5 $cm \times 10$ cm. In total more than 8.8 million films with a total surface of about 112500 m^2 are in the detector; this has required an industrial production,

that was done by the Fuji Film company.[1].

The nuclear emulsions consist of AgBr crystals, with a diameter of 0.2 μm, diffused in a gelatine binder; these can be ionized by the charged particles that cross this material. The radiation length of the nuclear emulsion is 5.5 cm and the energy deposit of a minimum ionizing particle (m.i.p) is 1.55 MeV/cm. The sensitivity of the film for a minimum ionizing particle passing the emulsion is $\sim 30-35$ $grains/100\mu m$.

Until they are developed, nuclear emulsions, as a normal photographic film, can collect all the tracks from charged particle. After the production, during the storage period, they accumulated many track signals due to cosmic rays and radioactivity of the enviroment. A refresh procedure has been developed to clean the films before using them to build the brick. The tracks during the refreshing can be erased without decreasing the sensitivity of the emulsion too much. Refreshing has been applied after the production at the storage place in the Tono mine (Japan), before shipping the emulsions to LNGS.

Two additional emulsion films, packed in aluminium foils inside a plastic box, are then glued externally to the bricks (white plastic box in the Fig. 2.5 on the right), the so-called Changeable Sheets (CS). The CS doublets are attached to the downstream face of each brick to have a confirmation that the brick really contains the neutrino events predicted by the electronic detector before opening and developing it.

Once the brick including the neutrino interaction is found and extracted, the CS are developed and analyzed. The scanning can be done in the LNGS or in the Nagoya laboratory. If in the CS films the predicted tracks are found, the event is confirmed and the brick is exposed to X-rays and cosmic rays for alignment reasons. Then it is developed in the LNGS laboratory and sent to the various scanning laboratories in Europe or Japan.

Two different scanning systems were developed in Japan and Europe; the first, called Super-Ultra Track Selector (S-UTS) [61] can reach a scanning velocity of 72 cm^2/h; the European system, ESS (European Scanning System) reaches 20 cm^2/h. The S-UTS can acquire sixteen photographic images at different depths of an emulsion layer. Each image is then shifted horizontally with respect to the first layer, so that the predicted tracks become perpendicular to the emulsion surface. Micro-tracks are identified by superimposing the 16 digitized images of one layer.

The European Scanning System (ESS) [62] has a different approach for the track reconstruction, it is the result of a joint effort of several European laboratories. It takes 16 tomographic images for each emulsion layer to build the possible micro-tracks. A micro-track consists of a straight line in the emulsion film, along which the clusters are placed in the different tomographic views. To reduce the checks of all the possible combinations of the clusters to form micro-tracks, some cuts are applied: micro-tracks are composed of a sequence of at least 6 grains, and only physically interesting track slopes (< 0.6 $mrad$) are accepted. In Fig. 2.6 the procedure to build the micro-tracks is sketched. Then the coincidence between two micro-tracks corresponding to the same charged particle are looked for. The construction of a base-track is obtained by con-

[1] http://www.fujifilm.com

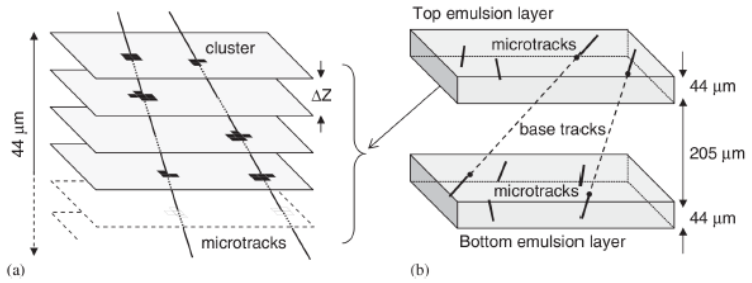

Figure 2.6: Schematic view of image taking and micro-track reconstruction by combining clusters belonging to images at different depth levels (left) and visualization of the linking process that combines micro-tracks from the top and the bottom emulsion layers to basetracks (right).

necting two micro-tracks from the intersection points with the plastic base, validating the connection if the micro-tracks agree within position and angular tolerance, and selecting the best connection after a χ^2 minimization.

2.2.2 The muon spectrometer

A magnetic spectrometer is placed after the target section in each SM. It consists of an inner tracker with a dipole magnet, made of two iron arms instrumented with RPC (Resistive Plate Chambers) planes. The measured magnetic field intensity is 1.55 T. Before, between and after the arms of the spectrometer Drift Tubes (DT) are placed to obtain a precise measurement of the charged particle's curvature in the magnetic field.

The main goals of the analysis of the spectrometer data are:

- trigger on beam data;
- reconstruction and identification of the muon track that leaves the target section, and measurement of the muon momentum and charge sign;
- measure the hadronic energy leaving the target section.

The muon identification is crucial in the OPERA experiment for the following reasons: for the study of the muonic τ decay channel, to suppress the background from the decay of charmed particles and to monitor the neutrino beam with the ν CC interactions.

The Inner Tracker

Each arm of the spectrometer, see Figs. 2.7 and 2.8, is made of 12 iron planes, 5 cm thick and interleaved by 11 RPC planes. The magnet is 8.75 m wide, 10.0 m high and 2.64 m long. The spectrometer is made of two arms, each 0.82 m thick, with a free space of 1.0 m in between allowing the insertion of the Drift Tube station. The total mass of the magnet is 990 t for each SM.

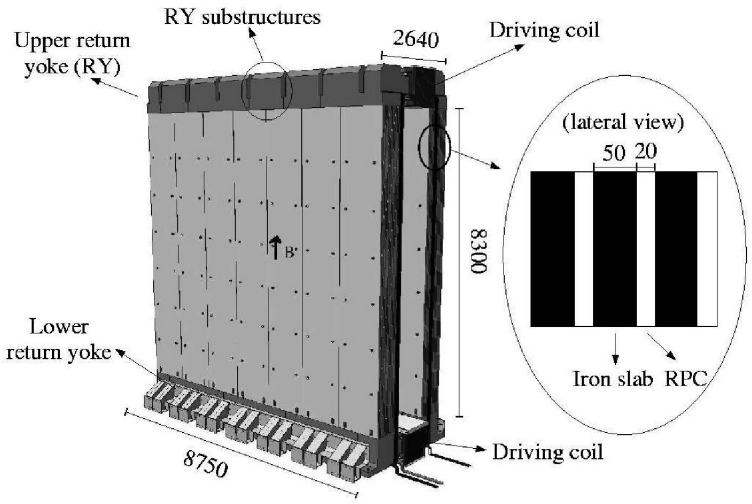

Figure 2.7: Three-dimensional view of one OPERA magnet. Units are in mm.

The magnet of the muon spectrometer is a dipole magnet, having a homogeneously distributed field inside the iron walls, with vertical direction but opposite sign in the two arms, as shown in Fig. 2.7.

The RPC instrumented walls have transversal dimensions of 8 $m \times 8.7$ m, bigger than the target sections to detect and measure the muons exiting from the target. Each single RPC wall is built using 28 separated RPC chambers, composed of two parallel bakelite plates, spaced by 2 mm. The area between these plates is filled with a mixture of argon, Tetrafluoroethylene, Isobutane and Sulfur Hexafluoride gas at the ratio of 75.4:20:4:0.6 [63]. Ionizing particles crossing the gas produce ions and electrons, which are then drifting in the electric field to the corresponding plate and induce a signal in the copper stripes. On each face of the chambers, the induced pulses are collected by 3 cm wide copper strips in the horizontal direction and by 2.6 cm wide one in the vertical direction.

XPC Behind the OPERA target two other walls of RPCs, called XPC (see Fig. 2.3), are placed. The readout strips in these planes have a width if 2.6 cm and are rotated by 42.6°. The RPC modules used to build the XPC are the same as the RPC ones.

DT To have a high precision measurement of the particle curvature in the magnetic field, 6 drift tube stations are placed in each spectrometer, two before two between and two after the spectrometer arms (see Fig. 2.8). Each station is composed of 4 planes of metal tubes, each layer consists of 256 vertical tubes, since the particles are deflected in the horizontal plane. The outer diameter of a tube is 34 mm and it is 8 m long. The transverse dimension of the drift tube station is 8.75×8 m^2 [64, 66].

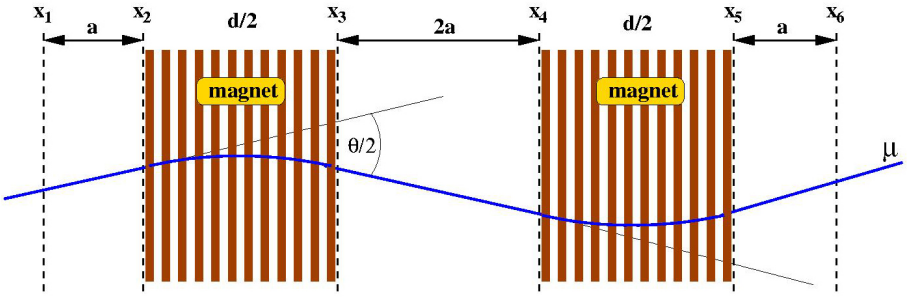

Figure 2.8: Schematic view of the spectrometer, including a skecth of a muon track deflected by the magnetic field. The dimensions called a and d in the text are shown. The x_i indicate the positions of the different drift tube stations.

In each drift tube a gas mixture of 80% argon and 20% CO_2 is used, the argon as drift gas and CO_2 as quench gas. In the center of each tube a 45 μm diameter, gold-plated tungsten wire is used as the anode wire. The ionizing particles crossing the drift tube will produce electrons (and ions) which will drift to the anode (cathode respectively). The drift velocity of the electrons in the tube is a few $cm/\mu s$, thus, a radial measurement of the distance from the crossing particle to the wire is possible. To get the explicit position of the crossing particle, 4 drift tube hits are needed to track the particles with a resolution of a few hundred μm.

Each muon, crossing the spectrometer will be deflected two times by the angle $\theta/2$, see Fig. 2.8, so that the momentum can be calculated as:

$$p = \frac{eBd}{\theta} \tag{2.4}$$

where $B = 1.55\ T$ is the magnetic field and $d = 1.2\ m$ the total iron thickness.

Denoting the measurement error of one coordinate measurement by ϵ, the contribution of the coordinate measurement error to the error of θ is: $\Delta\theta_x = \epsilon\sqrt{6}/a$, see Fig. 2.8. In addition, multiple scattering of the μ in the iron slabs gives an error on the angle of: $\Delta\theta_{ms} = \frac{14MeV}{pc}\sqrt{\frac{d}{X_0}}$, where X_0 is the radiation length of iron. Adding these two sources of error in quadrature and taking in to account eq. 2.4, the momentum resolution of the spectrometer is given by:

$$\frac{\Delta p}{p} \sim \frac{\Delta\theta}{\theta} = \frac{1}{eBd}\sqrt{6\left(\frac{\epsilon p}{a}\right)^2 + \frac{d}{X_0}\left(\frac{14MeV}{c}\right)^2} \tag{2.5}$$

The total thickness of the iron slabs was chosen as 1.2 m to reduce the contribution of the multiple scattering, and also the other parameters are chosen to keep the resolution within: $\Delta p/p < 25\%$ for $p < 25GeV/c$.

VETO The VETO is made of two RPC planes (identical to the ones in the spectrometer), placed before the target section of the first SM, as shown in Fig. 2.3. The

main task of the Veto is to select the events due to neutrino interactions upstream of the OPERA detector (so-called "rock- muon"), i.e. either inside the rock before the experiment or in the BOREXINO experiment (placed before OPERA in the beam direction).

2.3 Data acquisition and analysis

The selection of the events and the analysis chain in OPERA include different steps. It starts with the real-time analysis of the electronic detector, followed by the scanning of the emulsions, and can be split into following steps:

- on-time event selection and trigger
- electronic detector data analysis and brick finding
- CS scanning
- brick scanning
- decay search and topology check

On time event and trigger: Most of the tracks occurring in the OPERA detector are related to cosmic muons, as can be seen in the plot of Fig. 2.9, due to a remaining cosmic muon flux in the hall of $\sim 1/(h * m^2)$. To distinguish between cosmic and the beam induced events, a selection of the events on-time with the beam spill is made. The neutrinos from the CNGS beam spent 2.4 ms to travel from CERN to LNGS; a GPS system is used to synchronize the time-stamp created at LNGS and CERN, using the Universal Time Coordinate, with a precision of 100 ns.

In Fig. 2.10 the time-structure of the beam-induced events is shown, a spacing of 50 ms between the two peaks corresponds exactly to the structure of the SPS proton extraction. Also the duration of the single extraction, observable in the right of Fig. 2.10, is 10.5 μs and corresponds to the proton-extraction time-spill. The detector remains sensitive during the inter-spill time and runs in a trigger-less mode. Events detected out of the beam spill (cosmic-ray muons, background from environmental radioactivity, dark counts) are used for monitoring. The global DAQ is built as a standard Ethernet network whose 1147 nodes are the Ethernet Controller Mezzanines plugged on the controller boards interfaced to each sub-detector specific front-end electronics [83, 84]. A general 10 ns clock synchronized with the local GPS is distributed to all mezzanines in order to insert a time stamp to each data block. The event building is performed by sorting individual sub-detector data by their time stamps.

Electronic detector data analysis and brick finding The electronic detector data, once the on-time events are tagged, are used to reconstruct the event with the OpRec algorithm [74, 75]; its main goal is the identification of the brick in which the neutrino interaction occurred and the classification of the event. Examples of reconstructed events are shown in the Fig 2.11. The reconstruction of the events starts

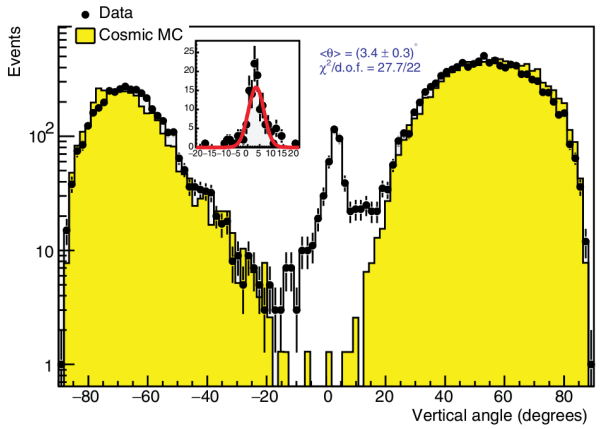

Figure 2.9: Angular distribution of cosmic muons and beam-induced muon events, obtained from electronic detector data. The histogram shows the comparison between data and simulation of cosmic-ray muons. The events coming from the CNGS beam are characterized by an angle of about 3.2° to the horizontal [68].

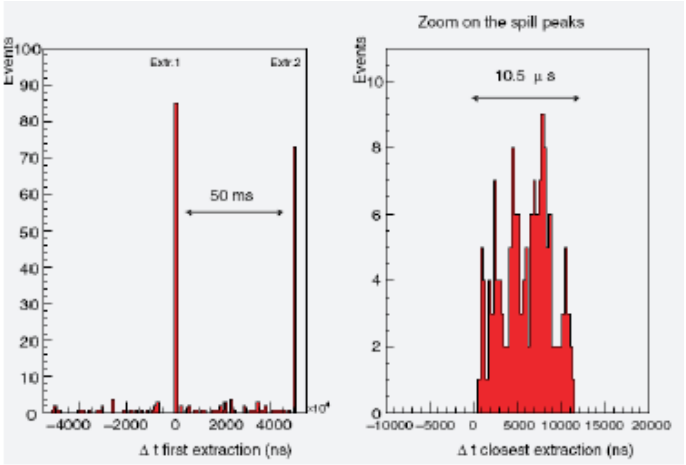

Figure 2.10: CNGS beam time structure seen in OPERA [68].

with the building of the possible tracks, as will be described in the next chapter.The characteristic and the efficiency of the reconstruction will be analyzed in details in the dedicated chapter, emphasizing the difference between the CC QE (quasi-elastic scattering) events, characterized by a clear long muon track, and a small activity in the region of the interaction, and the CC DIS (deep inelastic scattering) characterized by a muon track and a hadronic shower in the interaction region, that makes the reconstruction of the track more difficult.

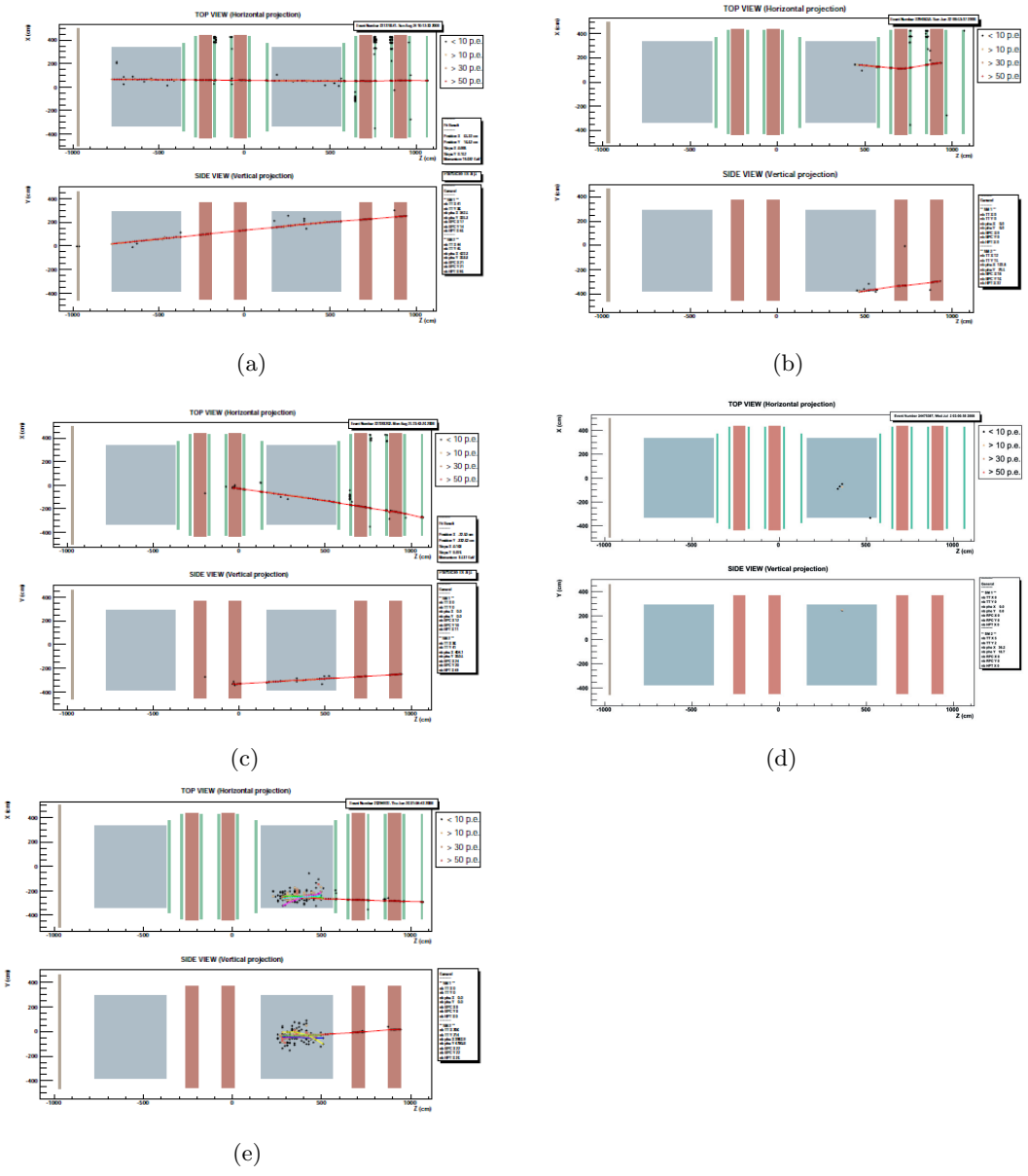

Figure 2.11: Display of events (bottom: side view, top: top view) classified as: a *front muon* in (a), a *side muon* in (b), a *spectro* in (c), a external neutral background in (d) and contained in (e).

The identification of the muon is really important to classify the event and to identify the brick in which the interaction occurred. It is based on the measured charge, done with the drift tubes, and on the length of the track, in particular on the total material crossed by the track in units of g/cm^2. A track is considered as a muon if the crossed material is larger than $660 g/cm^2$. As a consequence of these requirements, a muon with really low momentum can not be distinguished from the tracks in the hadronic shower.

An algorithm, called OpCarac [69], was implemented to classify the reconstructed events [69], this permits to distinguish neutral current (NC) and charged current(CC) events, characterized by the presence of a muon track reconstructed and identified. Moreover, the OpCarac algorithm classifies the on-time events into different categories. The classification categories are:

- *Front muon* These are events occurring in the rock or in the material upstream of the detector. They are charactherized by a muon track entering the OPERA detector in the first SM, see Fig. 2.11(a). They are selected analyzing the VETO signal and the signal in the first two TT planes. Since these planes are not filled with bricks, a track starting in these planes has a high probability to be produced upstream of the target. The events are classified as front muons, if a sufficient number of hits nearby the reconstructed muon track is recorded. However, it happens that CC events with a primary vertex in the lead/emulsion walls quite close to the first two empty walls may also give nearby hits in the backward direction with respect to the muon track due to the back-scattering effect. It is possible to distinguish this kind of event from a single muon track originating upstream of the target because the hadronic shower associated to the CC event in the target will deposit more energy in the TT.

- *Side muon* These events are characterized by a muon track entering the detector from the side, as shown in Fig 2.11(b). In this case the transverse position of the track starts in a boundary area of the target; a geometrical cut is applied on the beginnings of the track to select these events; the width of this border is the thickness of one brick from the external case of the target. To limit the problem generated by the wrong reconstruction of the track, also the hits not included in the track but lying in the border area are considered. Limiting the total number of hits prevents that hits from the hadronic shower and the back-scattering are wrongly added to the muon track in an event occurring near to the border (inside the target), mimicking the beginning of the track in the border area.

- *Spectro event* These events are defined as events produced by a neutrino interaction in the iron of the OPERA spectrometers, as shown in Fig. 2.11(c). If the interaction occurs in the iron of the first spectrometer, there should be no significant activity in the TT. In the case of a CC event, a muon track crosses the target of the second SM, if the interaction occurred in the first spectrometer. If the interaction occurs in the iron of the second spectrometer, there should be no hits in the target (no consecutive TT planes in coincidence).

- *External background* Front_muon and side_muon classes are events that can be

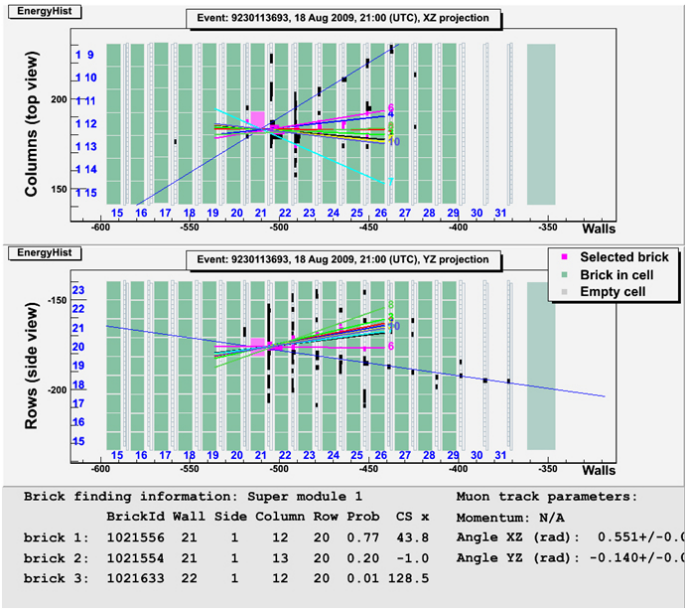

Figure 2.12: Event display with the result of the brick finding procedure.

considered as external background. There is, however, another class of events, where no three dimensional track is reconstructed, with a really difficult topology to select, as shown in Fig. 2.11(d). It is difficult to distinguish this kind of event from the low-energy NC background, especially when these events involve only a few hits. In any case, when they occurred in a region of the target that is empty (no bricks), they have a high probability to be due to external neutral particles reaching the target.

- *Contained events* This category collects all the events with the interaction in the target, NC and CC, that were not previously selected by the other classes. In Fig 2.11(e) an example is shown.

The tracks reconstructed from the electronic detector data are then analyzed to find the brick in which the interaction occurred. To do this a BF (Brick Finding) procedure has been developed. It is based on different procedures, one involved a Hough transformation of the electronic detector signal and the second one includes the tracking [74, 75] and the Kalman filter[81]. The Kalman filter will be discussed in the next chapter, including the resolution obtained in the reconstruction procedure. In both cases the brick finding procedure gives as output a list of possible bricks containing the interaction, with the respective probability, as shown in Fig. 2.12. The most probable brick is extracted with the BMS and its CS are sent to the CS scanning. In case of failure in the CS scanning to find the predicted tracks, discussed in the next paragraph, the next brick in the list is extracted.

CS scanning The placement of the CD doublet with respect to the brick is shown in Fig. 2.3. The extracted brick with the attached CS doublet is X-ray marked to align

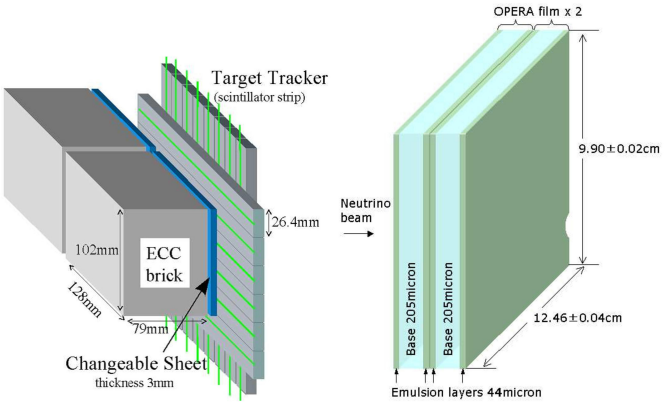

Figure 2.13: Schematic view of the OPERA ECC cell inside the detector, and of the CS doublet.

the CS with the last emulsion of the brick. Then the CS are detached and developed to be scanned, while the ECC remains underground to await the CS scanning result. The scanning area is fixed to 4×6 cm^2 around the muon prediction in case of CC interactions, for NC events a larger area is scanned.

The information of the CS is used also for a more precise prediction (in comparison with the one from the electronic detector) of the position of the tracks in the most downstream films of the brick, for the so-called scan-back vertex-finding procedure.

Brick scanning After the CS scanning gave a positive result, the ECC is first exposed to cosmic rays then disassembled. The emulsions are developed in the LNGS laboratory and sent to one of the various scanning laboratories around the world. The brick scanning procedure is performed in different consecutive steps:

- *Scan-Back*: the tracks found in the CS films are extrapolated to the last emulsion film in the brick, where an area of 3×3 mm^2 is scanned to look for them. Then these tracks are followed moving in the upstream direction with a procedure that is illustrated in Fig. 2.14: the track found is projected to the previous film where a certain region is scanned to look for the consecutive segment. The scan is performed until the stopping point is found.

- *Total Scan*: This step foresees to scan a big area around the stopping point of a track to search for a neutrino interaction vertex. The scanned volume consists of 15 consecutive plates, 10 plates downstream of the stopping point and 5 plates upstream, each scanned in an area of 1 cm^2. In that volume all the tracks are followed, to reconstruct completely the interaction vertex and to collect all the kinematic information for further analysis. In Fig. 2.15 these different steps are illustrated, it is possible to observe the selection of the interesting base tracks that compose a particle track from a big number of base tracks not correlated to the event.

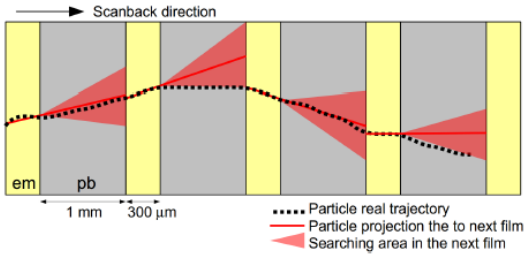

Figure 2.14: Scan Back procedure, the track followed and the searching area are shown.

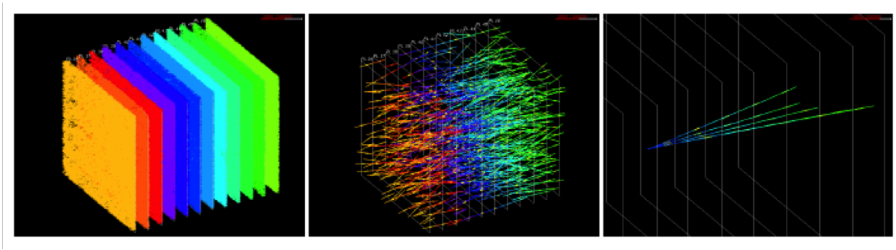

Figure 2.15: Different steps of the scanning procedure. All basetracks that are found in the volume are shown on the left side, in the middle picture only the tracks reconstructed from these Basetracks are shown, and finally on the right side, the tracks correlated with the interaction are shown [56].

- *Scan Forth*: In this step all the tracks from the vertex are followed in the downstream direction (opposite to the Scan Back step), until the stopping point, that could be inside the brick. The aim of this step is to collect all the kinematic informations about the tracks, attached to the vertex.

Decay search After the vertex is located, a special decay search procedure is applied to the vertex to find all possible tracks involved in the interaction and the possible secondary vertices, to fully understand the decay. In this step kinematical cuts are applied to select possible τ and the charm decay candidates. A search analysis of electromagnetic showers, to identify the electron and π^0's is also performed.

2.4 OPERA sensitivity for τ appearance

OPERA expects to have the performance of finding about 10 τ decay events within five years of running, assuming a total of $4.5\times10^{19} p.o.t.$ per year and $\Delta m^2 = 2.5\times10^{-3} eV^2$ and full mixing. Tab. 2.2 shows the expected signal and background in the different decay channels.

The ν_τ observation probability of OPERA, considering five years of data taking at nominal beam, and $\Delta m^2_{32} = (2.43 \pm 0.13) \times 10^{-3} eV^2$ is plotted in Fig. 2.16.

Channel	BR %	Signal (events)	background (event)
$\tau \to e$	17.4%	2.9	0.17
$\tau \to \mu$	17.8%	3.5	0.47
$\tau \to h$	49.6%	3.1	0.24
$\tau \to 3h$	15.2%	0.9	0.17
Total	$BR \times \epsilon$	10.4	~ 1

Table 2.2: Number of expected τ and background events for five years of nominal beam [53].

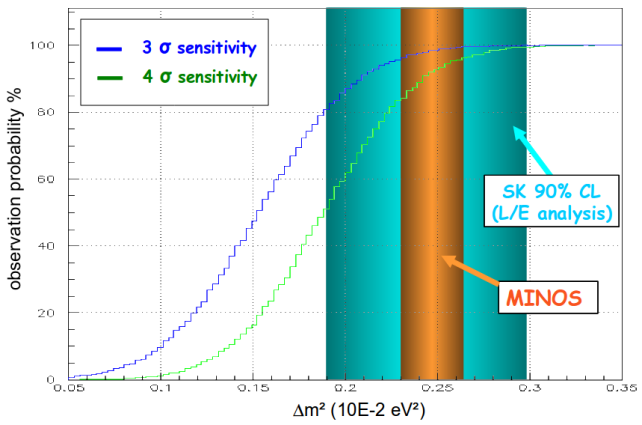

Figure 2.16: OPERA ν_τ observation probability for 22.5×10^{19} p.o.t. .

	p.o.t.	events collected	
2006	0.076×10^{19}	no bricks	Commissioning
2007	0.082×10^{19}	38	Commissioning
2008	1.78×10^{19}	1698	First physics run
2009	3.52×10^{19}	3693	Physics run
2010	4.04×10^{19}	4248	Physics run

Table 2.3: Numbers of events collected in the bricks during the past OPERA runs.

2.4.1 OPERA data taking and first results

The first commissioning run of the CNGS beam and the OPERA experiment was in the year 2006. After a very short run in 2007 with a few events, the first long physics run started in 2008. The number of events collected is summarized in Tab. 2.3. The first CNGS commissioning run took place in 2006, collecting data corresponding to about five days of nominal beam; in this run the target was empty, so only the electronic detectors were tested, with an efficiency more than 95%. The 2007 run was really short due to the CNGS stop at CERN; the target was only partially full, 38 events in the bricks were collected and the ECC analysis chain was fully tested.

In 2008, 2009, 2010 the experiment was running without relevant problems, both for the beam and the detector, it recorded more than 9000 events in the bricks. The scanning procedure and analysis is finished for the 2008 and 2009 events, and ongoing for the 2010 event.

Some main results, which have been obtained until now, are briefly summarized in this section, separately for the electronic detector and the emulsion analyses.

Electronic detector results. The main results obtained with the electronic detectors have been published in [85]: the NC to CC events ratio, the muon momentum spectrum, the reconstructed energy and the hadronic shower proile. The measured NC to CC events ratio is an important cross check , it is taking into account the true NC/CC ratio (= 0.3), the muon identification efficiency, the fraction of the CC misidentified as NC events, and the fiducial volume selection efficiency. The fiducial volume selection is necessary to reduce the background accumulation at the target borders due to particles produced in beam-neutrino interactions outside the target in the rock and surrounding material. Very good agreement is found for this ratio between the MC-expectation and the measurement in the analysis of 2008 and 2009 data:

Data	0.228 ± 0.008
MC	0.257 ± 0.031

In Fig. 2.17 the total reconstructed energy for the events with at least one identified muon is shown. The total energy includes the hadron energy and the muon energy; a

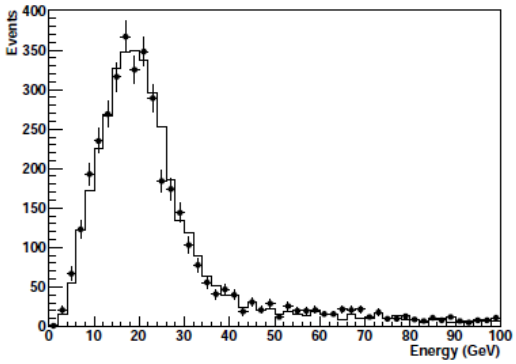

Figure 2.17: Total reconstructed energy for events with at least one identified muon for data (dots with error bars) and MC (solid line). The MC distribution is normalised to data [85].

calibration of the electronic detector (ED) has been performed in order to convert the visible energy into total energy. The agreement between data and MC is quite good.

Analysis of the emulsions. These analyses were reported together with the first τ decay candidate in [72], an were obtained from data collected in 2008 and early 2009: the decay search analysis has been applied to about 35% of the 2008-2009 emulsion data sample, this corresponds to an integrated beam intensity of $1.89^{19} p.o.t$ and 1088 ν_μ events of which 901 were classified as CC interactions.

For this sample the distribution of the position of the interaction vertex in the emulsion films is observed to be uniformly distributed in the transverse plane, confirming that the scanning and anlaysis procedure is not biased. The impact parameter (IP) distribution at the ν_μ interaction vertex is shown in Fig. 2.18, it is well contained within 10 microns. The IP distribution for the daughter tracks from τ decays from a Monte Carlo simulation is also shown, typical τ decay IP values are well beyond the region dominated by the experimental resolution.

The comparison between the muon momentum measured with the electronic detector (spectrometer) and the estimation from MCS in the bricks is important for the further analysis presented in this thesis. This comparison has been made for a sample of stopping muons (muon that stop inside the OPERA detector), and is shown in Fig. 2.19. The agreement is quite good with a resolution of about $\pm 22\%$.

First observed τ candidate In the summer of 2010, OPERA made a first observation of a candidate $\nu_\tau CC$ interaction [72]. The event contains 7 tracks of which one exhibits a visible kink of $41 \pm 2\ mrad$. The τ^- lepton track decays in the hadronic channel: $h^-(n\pi^0)\nu_\tau$: the daughter track has been followed in the downstream bricks and, after crossing 7 walls, it was seen to generate a hadronic interaction, identifying it as a hadron. The other tracks from the neutrino interaction were also followed until they stop or interact, no muon was found. The candidate passes all the selection criteria already described for this decay channel, and (considering the background estimation)

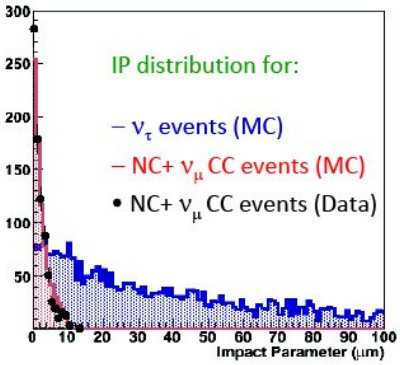

Figure 2.18: Simulated τ daughters impact parameter distribution is shown by the blue shaded histogram, the impact parameter distribution measured for tracks emitted at the primary vertex in MC ν_μ interaction events is shown by the red shaded histogram. The corresponding observed distribution (black dots) does not include the tau and charm decay candidates.

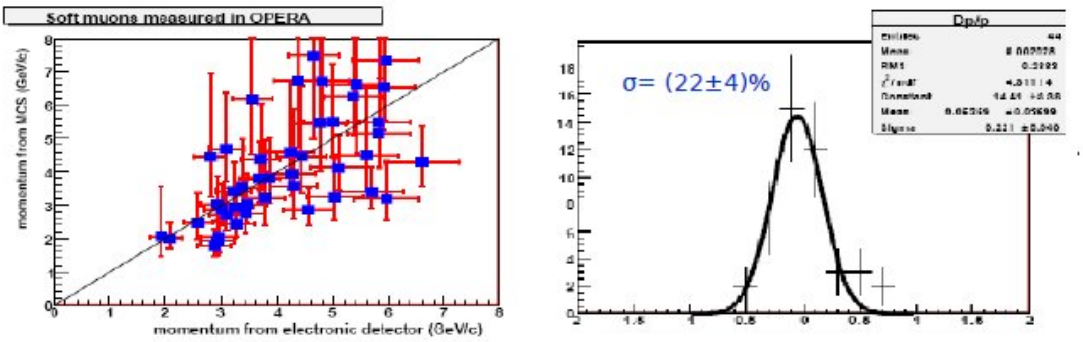

Figure 2.19: Correlation between muon momentum measurements in the brick (using MCS) and by the electronic detector on the left, and normalized difference between these measurements of the momentum on the right.

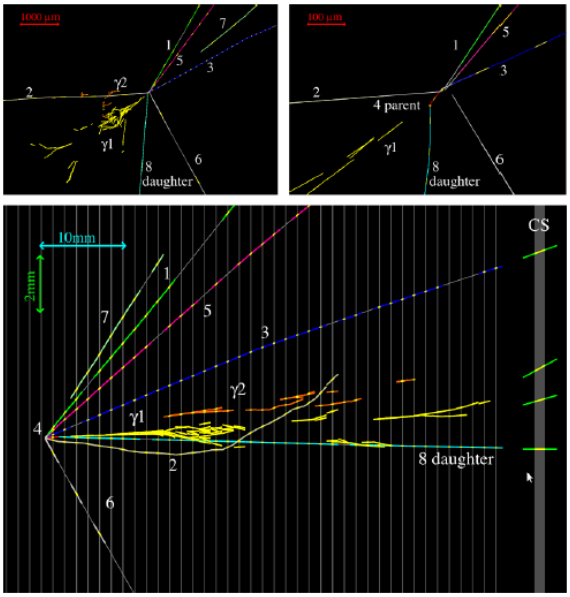

Figure 2.20: First observed τ decay candidate.

has a significance of 2.01σ of not being a background event, if all decay modes are considered.

The expected number of detected ν_τ events in the sub-sample analyzed was $0.54 \pm 0.13(syst.)$ in the hadronic channel.

Chapter 3

Event reconstruction in the electronic detectors and MC studies

As mentioned in the previous chapter, the reconstruction of events using the electronic detector data represents the first step in the analysis chain for the on-time events in OPERA. The first part of the chapter will give a short introduction to the track finding procedure in OPERA, fully described in the PhD thesis [74] and in the OPERA internal notes [75]; once the tracks are reconstructed, a Kalman filter fit is applied to estimate the kinematic variables (position of the starting point, slope, momentum) of the track. The description of the Kalman filter fit, and its application in OPERA, including the possible corrections to the track finding, will be presented next. In the second part of the chapter, MC studies of the track reconstruction software will be presented including both: the track finding and the Kalman filter procedure. This yields an understanding of the performance of the reconstruction software in terms of resolution of the reconstructed starting point position and momentum of the tracks, as well as the purity of the CC interactions analyzed. The MC studies have been done for the different neutrino interactions: CC (quasi-elastic and deep inelastic) and NC and for antineutrino CC DIS interactions; this study will be used to estimate the muon momentum spectrum expected from the neutrino interactions in OPERA, including the contamination due to the NC events and the $\overline{\nu}$ interactions.

3.1 Tracking Finding (Finding procedure)

One of the main aim of the electronic detector (ED) data reconstruction is to find the brick in which the interaction occurred; in the case of $\nu_\mu$charged current events this could be obtained by the reconstruction of the muon track and its identification. The main purpose of this work is to investigate the reconstruction and the identification of μ^- tracks.

The track finding procedure is a software written to analyse the signals from the electronic detector and to find the possible tracks due to charged particles in the

detector target. Due to the geometrical structure of the ED, the particle crossing the detector gives signals in the scintillator strips of the TT, in the strips in the RPC and in the drift tubes. The goal of the track finding is to connect the hits in the different planes of the ED to reproduce the probable path of the particle in the detector.

The complete tracking procedure and all the cuts applied are described in [75], in a short summary, it is possible to divide the procedure in different steps: building of possible couples of hits in adjacent planes, building of the track-segment in each detector, building of the two-dimensional tracks starting with the connection of track-segments, and combining the two-dimensional tracks to build a three-dimensional final track.

The first step of the tracking procedure is to build the track in each detector separately, this part of the track is generally called segment; the procedure starts building the possible couples of hits in the event; a possible couple of hits is the connection between the hits in two adjacent planes. Due to the fact that in OPERA the interesting tracks (from beam events) have a clear structure, with the track developing along the z-axis, some selections on the maximal angle with respect to the z-axis and on the maximal length of the segment are applied on the possible couples of hits; in Fig. 3.1 the allowed and the forbidden couples of hits are shown. The cuts clearly depend on the different detectors. To build the segment of a track in each detector the software tries to combine the hit couples previously created. It starts from the most downstream position, validating each connection using cuts on maximum slope of the track and limiting the different slopes between the connections. The procedure moves upstream along the event until the first hit in the detector is reached. The scheme of the possible segments built is shown in Fig. 3.1; the different possible segments are compared using as criteria: the length of the segment and the mean scattering angle, to find the straightest segment. Once a segment has been built, all the hits included in it are removed from the list and the procedure is applied on the remaining hits in the event to form other segments.

The connections of segments in different detectors, Target Tracker, downstream and upstream RPC, are done starting from the most downstream one. The procedure develops always between a downstream segment and a list of possible connected upstream segments; the first connection validation criterion is the compatibility of the slope of the two segments, as shown in Fig. 3.2; then a cut on the length of the upstream segment is applied. At the end of this step a list of two dimensional tracks is created.

The last step aims to merge, if possible, two two-dimensional tracks from the *(xz)* and *(yz)* projections to obtain a three-dimensional track, that describes the path of the particle in the detector.

3.2 The Kalman filter

In 1960 Kalman described for the first time a recursive solution to the data-filtering problem, well known as the Kalman filter [76]. In his first paper he called this a solution for the problem to find the most probable value to estimate the state of a

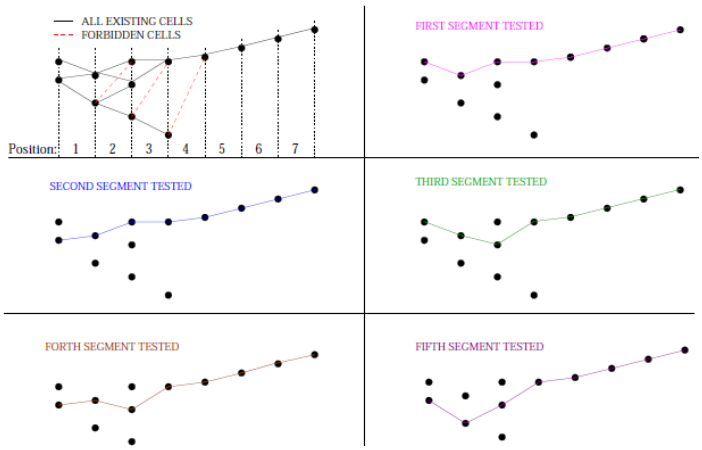

Figure 3.1: Examples of possible connections between hits in the event, and building of the possible track segments [75]; the five shown segments represent the possible segments built with these hits, the procedure chooses between these the best segment, following the cuts described in the text.

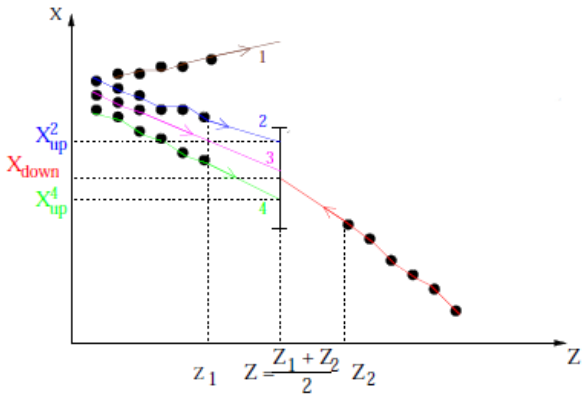

Figure 3.2: Connection step between two segments in different detectors [75].

linear dynamic system:

"An important class of theoretical and practical problems in communication and control is of a statistical nature. Such problems are:

- *Prediction of random signals;*
- *separation of random signals from random noise;*
- *detection of signals of known form (pulses, sinusoids) in the presence of random noise*

This paper introduces a new look at this whole assemblage of problems" [76].

A historical introduction to the Kalman filter can be found in [77], as a natural evolution of the least-squares estimation: *The Gaussian concept of estimation by least squares, originally stimulated by astronomical studies, has provided the basis for a number of estimation theories and techniques during the ensuing 170 years, probably none as useful in terms of today's requirements as the Kalman filter. Since the Kalman filter represents essentially a recursive solution of Gauss' original least-squares problem, it is reasonable to consider the substance of Kalman's contribution and attempt to put it into perspective. It cannot be denied that there has been a substantial contribution, if for no other reason than the large number of theoretical and practical studies that it has initiated. I suggest that the contribution is significant for two basic reasons:*

- *The Kalman filter equations provide an extremely convenient procedure for digital computer implementation.*
- *Kalman posed the problem in a general framework that has had a unifying influence on known results* [77].

3.2.1 Introduction to the Kalman filter

The Kalman filter's aim is to estimate the state of a discrete process, generally represented by a vector describing a dynamic system, from a set of measurements taken at different times. It is an iterative procedure that moves from one measurement to the next, improving the knowledge about the state of the process with each new data. It is an ideal technique for track reconstruction and fitting in particle physics [78], taking into account the energy loss and multiple scattering of the particle generating the track. Considering the evolution of the state of a linear dynamic system, it is described by a linear transformation $\mathbf{F}$ plus a possible random noise w:

$$x_k = \mathbf{F}_{k-1} x_{k-i} + w_{k-1} \tag{3.1}$$

where x represents the true vector describing the process, and k the evolution of the vector, that could proceed in space (as often happens for the track reconstruction) or in time; w_k represents instead the process noise. The measurements m_k of the state k of the dynamic system, are linear functions of the state vector x_k:

$$m_k = \{H\}_k x_k + \epsilon_{k-1} \tag{3.2}$$

where ϵ_k are the measurement errors. The process noise and the measurement error are assumed to be independent and with normal probability distribution, i.e.:

$$\begin{aligned} E\{w_k\} = 0 \quad cov\{w\} = \{Q\}_k \\ E\{\epsilon_k\} = 0 \quad cov\{\epsilon\} = \{V\}_k \equiv G_k^{-1} \end{aligned} \tag{3.3}$$

Taking into account that the evolution of the dynamic system could be in time, in space or simply in the number of repeated measurements of the same state, the past and future of the dynamic system is related to the development of the Kalman fit. For a dynamic system the step k can be estimated including different levels of information given by the measurements:

- *prediction or extrapolation:* is the estimation of the vector at the next step from the knowledge of the past state vector
- *filtering:* estimation of the present state, including all the information given by the measurements until now
- *smoothing:* is the estimation of the state vector at some point in the past, including all the information given by the measurement until now.

Using this notation, the vector describing the dynamic system at time t, $x_{k,t}$, represents the value at step k, x_k^j the estimated value if $j < k$ and the filtered estimated value if $j = k$. In the same notation the covariance matrix and the residual of the measurement k are defined as:

$$\begin{aligned} residual \quad r_k^j = m_k - \mathbf{H}_k x_k^i \\ \mathbf{R}_k^i = cov\{r_k^i\} \\ \mathbf{C}_k^i = cov\{x_k^i - x_{x,t}\} \end{aligned} \tag{3.4}$$

For the state k the extrapolation of the vector is obtained using:

$$\begin{aligned} x_k^{k-1} &= \mathbf{F}_{k-1} x_{k-1} \\ \mathbf{C}_k^{k-1} &= \mathbf{F}_{k-1} \mathbf{C}_{k-1} \mathbf{F}_{k-1}^T + \mathbf{Q}_{k-1} \\ r_k^{k-1} &= m_k - \mathbf{H}_k x_k^{k-1} \\ \mathbf{R}_k^{k-1} &= \mathbf{V}_k + \mathbf{H} \mathbf{C}_k^{k-1} \mathbf{H}_k^T \end{aligned} \tag{3.5}$$

The updating of the system state vector with the k measurement is performed with

the following equation, using the **K** matrix, the so called gain filtered matrix:

$$\begin{aligned}
\mathbf{K}_k &= \mathbf{C}_k^{k-1}\mathbf{H}_k^T(\mathbf{V}_k + \mathbf{H}_k\mathbf{C}_k^{k-1}\mathbf{H}_k^T)^{-1} \quad = \quad \mathbf{C}_k\mathbf{H}_k^T\mathbf{G}_k \\
x_k &= x_k^{k-1} + \mathbf{K}_k(m_k - \mathbf{H}_k x_k^{k-1}) \\
\mathbf{C}_k &= (1 - \mathbf{K}_k\mathbf{H}_k)\mathbf{C}_k^{k-1} \\
r_k &= m_k - \mathbf{H}_k x_k = (1 - \mathbf{H}_k\mathbf{K}_k) r_k^{k-1} \\
\mathbf{R}_k &= (1 - \mathbf{H}_k\mathbf{K_k})\mathbf{V}_k = \mathbf{V}_k - \mathbf{H}_k\mathbf{C}_k\mathbf{H}_k^T \qquad (3.6)
\end{aligned}$$

(3.7)

In the above equation F is a matrix, because the propagation is described by a linear equation. In the case of non-linear systems, it should be linearized, by replacing:

$$\begin{aligned}
\mathbf{F}_k x_k \quad &\rightarrow f_k(x_k) \\
\mathbf{K}_k \quad &\rightarrow \quad \frac{\partial f_k}{\partial x_k} \qquad (3.8)
\end{aligned}$$

where $f_k(x_k)$ is the linearized matrix of F_k. Using the residual calculated in the filtering step, it is possible to calculate the χ^2_F of the filtered step:

$$\chi^2_{F_k} = r_k^T \mathbf{R}_k^{-1} r_k \qquad (3.9)$$

The filtered residual vectors are uncorrelated, and in the Gaussian case also independent.

The global χ^2 of the track gives an estimation of the quality of the track reconstruction, in fact, it is a powerful test against ghost tracks (random association of hits).

The residuals of the fit can be used to detect the outliers. An useful criterion [78] to estimate the "closeness" is the χ^2 of the filtered step. If m_k belongs to the track and the covariance matrix of its Gaussian errors is accurately known, χ^2_F is χ^2-distributed with f degrees of freedom, where f is the dimension of m_k. If χ^2_F is larger than a given bound c, the measurement is rejected as an outlier: c is the quantile $(1 - \alpha)$ of the appropriate χ^2 distribution, the probability of rejecting a good measurement is equal to α.

The state vector at the last point of the fit contains all the information from all the measurements. But it is also possible to have the full information vector for each point of the fit using the smoothing equation; also in this case the matrix A is called smoother gain matrix.

$$\mathbf{A}_k = \mathbf{C}_k\mathbf{F}_k^T(\mathbf{C}_{k+1}^k)^{-1} \qquad (3.10)$$

$$\begin{aligned}
x_k^n &= x_k + \mathbf{A}_k(x_{k+1}^n - x_{k+1}^k) \\
\mathbf{C}_k^n &= \mathbf{C}_k + \mathbf{A}_k(\mathbf{C}_{k+1}^n - \mathbf{C}_{k+1}^k)\mathbf{A}_k^T \\
r_k^n &= r_k - \mathbf{H}_k(x_k^n + x_k) = m_k - \mathbf{H}_k x_k^n \\
\mathbf{R}_k^n &= \mathbf{R}_k - \mathbf{H}_k\mathbf{A}_k(\mathbf{C}_{k+1}^n - \mathbf{C}_{k+1}^k)\mathbf{A}_k^T\mathbf{H}_k^T = \mathbf{V}_k - \mathbf{H}_k\mathbf{C}_k^n\mathbf{H}_k^T \qquad (3.11)
\end{aligned}$$

The smoothing is a recursive operation which proceeds step by step in the direction opposite to that of the filter.

3.3 Kalman filtering in OPERA

To the three-dimensional track reconstructed by the tracking package, described in section 3.1, a Kalman filter procedure is applied to estimate the muon momentum, and the position at the beginning of the track. Each 3-dim track is built as a list of points in two dimensions: *(x,z)* or *(y,z)* coordinates along the z-axis. Since the aim of the track reconstruction in OPERA is to find the brick containing the interaction, the Kalman filter is applied as an iterative procedure starting from the last point of the track (maximum z-coordinate value), to the first point (minimum z-coordinate, interaction vertex region).

The five parameters forming the parameter vector P, which have to be determined with the Kalman fit for each point with fixed z position, are: $(x, y, a = p_x/p_z, b = p_y/p_z, d = p/q)$, where (p_x, p_y, p_z) are the three components of the muon momentum $\overrightarrow{p}$ and q is the muon charge sign. Each measurement is given a weight (w_{x_i}) equal to the inverse spatial resolution squared. Since the measured points in OPERA are two-dimensional *(x,z)* or *(y,z)*, each point is added to the fit in one projection, fixing the weight of the other coordinate to 0.

The parameter vector P is associated with a z-point along the track and can be estimated, as usual for the Kalman filtering, taking into account all the measurements until the z-position considered. The Kalman procedure in OPERA starts from the last point of the track, and each step of the Kalman filtering approaches to the interaction vertex region.

It is defined now, that the vector P_i and the corresponding weight matrix W_i are computed step by step from P_i and W_i, with bigger z-coordinate [81].

The evolution of the parameter vector P is described decoupling the geometrical extrapolation from the energy loss and the multiple scattering due to matter effect. The latter one is correlated to the geometry implementation and will be described in the next paragraph. To include the homogeneous magnetic field B in the spectrometer, the geometrical extrapolation from a point at position z_i to the one at position z_{i-1} uses Taylor expansions ($\delta z_{i-1} = z_i - z_{i-1}$) (the superscript e stands for the extrapolation step) [81]:

$$\begin{aligned} x^e_{i-i} &= x_i + a_i \Delta z_{i-1} + \frac{1}{2} A_i \Delta z^2_{i-1} + ... \\ y^e_{i-i} &= y_i + b_i \Delta z_{i-1} + \frac{1}{2} B_i \Delta z^2_{i-1} + ... \\ a^e_{i-i} &= a_i + A_i \Delta z_{i-1} + ... \\ b^e_{i-i} &= b_i + B_i \Delta z_{i-1} + ... \\ d^e_{i-1} &= d_i * \end{aligned} \tag{3.12}$$

where d is the (constant) curvature for the case without matter. Once taking into account the energy loss in the material, d_i* represents the curvature d at the z-coordinate i, including the energy loss between step i and $i-1$. The curvature is calculated considering the presence (in the spectrometer) or the absence (in the target) of magnetic field. A and B are given by:

$$A = (cos\theta)^{-1} d[bB_z + abB_x - (1+a^2)B_y]$$
$$B = (cos\theta)^{-1} d[-aB_z - abB_y - (1+b^2)B_x] \tag{3.13}$$

where $B_{x,y,z}$ are the three Cartesian components of the magnetic field and $cos\theta = (1+a^2+b^2)^{-1/2}$. In case of no multiple scattering and no error on the energy loss, that will be taken into account later, the weight matrix W_{i-i} of P_{i-1} is calculated, starting from the previuos step as:

$$W^e_{i-1} = (D^{-1}_{i-1,i})^T W_i D^{-1}_{i-1,i} \tag{3.14}$$

with

$$D_{i-1,i} \equiv \left(\frac{\partial P^e_{i-1}}{\partial P_i} \right)_{5\times5} \tag{3.15}$$

Considering that the weight matrix is the inverse of the covariance matrix, this is the usual Kalman extrapolation step. The matrix $D_{i-1,i}$ is given by:

$$D_{i-1,i} = \begin{bmatrix} 1 & 0 & \Delta z_{i-1} + F_1 \Delta z^2_{i-1} & F_2 \Delta z^2_{i-1} & F_3 \Delta z^2_{i-1} \\ 0 & 1 & G_1 \Delta z^2_{i-1} & \Delta z_{i-1} + G_2 \Delta z^2_{i-1} & G_3 \Delta z^2_{i-1} \\ 0 & 0 & 1 + F_1 \Delta z_{i-1} & F_2 \Delta z_{i-1} & F_3 \Delta z_{i-1} \\ 0 & 0 & G_1 \Delta z_{i-1} & 1 + G_2 \Delta z_{i-1} & G_3 \Delta z_{i-1} \\ 0 & 0 & \partial d^e_{i-1}/\partial a_i & \partial d^e_{i-1}/\partial b_i & \partial d^e_{i-1}/\partial d_i \end{bmatrix} \tag{3.16}$$

The coefficients F, G and the partial derived of d_i are reported int the OPERA internal note [81]. Considering the usual vector of the Kalman procedure $P(x, y, a, b, d)$, x and y are the coordinate position, a the slope of the track in the *(xz)* plane, b the slope in the *(yz)* plane, and d the ratio q/p, where p is the muon momentum, and q the charge sign.

If the vector $\overrightarrow{\eta} = \overrightarrow{p}/p$ is considered, its evolution in case of a uniform magnetic field (B) is:

$$\frac{d\overrightarrow{\eta}}{ds} = \frac{q}{p} \overrightarrow{\eta} \times \overrightarrow{B} \tag{3.17}$$

where s is the abscissa along the track path. Hereafter the d-parameter definition $d = q/p$ is used. The $overrightarrow\eta$ vector is also defined as:

$$\overrightarrow{\eta} = \left(\frac{dx}{ds} = acos\theta, \frac{dy}{ds} = bcos\theta, \frac{dz}{ds} = cos\theta \right) \tag{3.18}$$

with $cos\theta = (1 + a^2 + b^2)^{-1/2}$ and $a = p_x/p_z$ and $b = p_y/p_z$. Then, considering a step between two points,with indices 0 and 1, with a path of $\Delta s_1 = (z_1 - z_0)/cos\theta_1$,

the extrapolation obtained with a Taylor expansion of the eq. 3.17

$$\begin{aligned} a_0 cos\theta_0 &= a_1 cos\theta_1 + (cos\theta_1)^{-1}\left(\frac{d\eta_x}{ds}\right) + \Delta z + ... \\ b_0 cos\theta_0 &= b_1 cos\theta_1 + (cos\theta_1)^{-1}\left(\frac{d\eta_y}{ds}\right) + \Delta z + ... \\ cos\theta_0 &= cos\theta_1 + (cos\theta_1)^{-1}\left(\frac{d\eta_z}{ds}\right) + \Delta z + ... \end{aligned} \tag{3.19}$$

Considering the notation used in the Chapter 3, the coefficients A_1 and B_1 are:

$$\begin{aligned} A_1 &= (cos\theta_1)^{-1} d_1 \left[b_1 B_z + a_1 b_1 B_x - (1 + a_1^2) B_y\right] \\ B_1 &= (cos\theta_1)^{-1} d_1 \left[-a_1 B_z + a_1 b_1 B_y - (1 + b_1^2) B_x\right] \end{aligned} \tag{3.20}$$

Hence, the coefficient F_1 is derivateed, e.g. as follows:

$$\left(\frac{\partial P_{i-1(1)}}{\partial P_{i(3)}}\right) = D_{i-1,i}[1,3] = \Delta z_{i-1} + \frac{1}{2}\Delta z_{i-1}^2 \frac{\partial A_i}{\partial a_i} \tag{3.21}$$

and

$$\frac{\partial A_i}{\partial a_i} = \left[(cos\theta_1^{-1} d_1)(b_1 B_x - 2a_1 B_y) + \frac{d(cos\theta^{-1})}{da_1}\frac{A cos\theta}{d1}\right] \tag{3.22}$$

defining $A_1 = A_1' d_1 (cos\theta_1)^{-1}$ the coefficient F_1 is:

$$F_1 = \left[(cos\theta_1^{-1} d_1)(b_1 B_x - 2a_1 B_y) + a cos\theta A_1'\right]. \tag{3.23}$$

To include the multiple scattering and the energy loss fluctuations the weight matrix is modified:

$$W_i \rightarrow \left[W_i^{-1} + Q_{i-1,i}\right]^{-1} \tag{3.24}$$

with

$$Q_{i-1,i} = \begin{bmatrix} 0 & 0 & 0 & 0 & 0 \\ 0 & 0 & 0 & 0 & 0 \\ 0 & 0 & Q_{aa} & Q_{ab} & 0 \\ 0 & 0 & Q_{ab} & Qbb & 0 \\ 0 & 0 & 0 & 0 & Q_{dd} \end{bmatrix} \tag{3.25}$$

and

$$\begin{cases} Q_{aa} = \delta\alpha_{MS}^2 (1 + a_i^2 + b_i^2)(1 + a_i^2) \\ Q_{bb} = \delta\alpha_{MS}^2 (1 + a_i^2 + b_i^2)(1 + b_i^2) \\ Q_{ab} = \delta\alpha_{MS}^2 (1 + a_i^2 + b_i^2) a_i b_i \\ Q_{dd} = \left(\frac{\partial d_i^*}{\partial E_{c_i}^*}\right)\sigma(\Delta E_{c_{i-1},i}) \end{cases} \tag{3.26}$$

where the variance of the scattering angles is :

$$\delta\alpha_{MS} = 2.557\chi_{cc}\frac{\sqrt{L_{i-1,i}}}{E_i\beta_i} \tag{3.27}$$

The χ_{cc} coefficient depends on the material crossed; L is the track-length of the step considered, E the energy of the particle. The addition of the point is performed as usual in the Kalman filtering method.

Matter effects. The matter effects on the curvature d^* are included in the Kalman filter in the following way:

$$\begin{aligned} d_i^* &= \frac{q_i}{[E_{c_i}^*(E_{c_i}^* + 2_{m_\mu})]}^{1/2} \\ E_{c_i}^* &= E_{c_i} + \Delta E_{c_{i-1},i}(E_{c_i}^*) \end{aligned} \tag{3.28}$$

where m_μ is the muon mass. The mean energy loss ΔE is calculated by a GEANT3.21 routine:

$$\Delta E_{c_{i-1,i}}(E_i^*) = L_{i-1,i}\frac{dE}{dx}(E_{c_i}^*, mat_{i-1,i}) \tag{3.29}$$

where mat is meaning all the relevant information about the material crossed, i.e.: density, atomic number and mass number. The different materials crossed by the track in a step, between z_{i-1} and z_i are taken into account, and a mean value of the density, A and Z are provided by the software package OpUtils in each step.

Including DT points in the three-dimensional track. The DT points are included in the Kalman filter after an accurate fit in each DT station (each DT station, as described in the previous chapter, is composed by four planes of DT). A detailed description of this fit and the resolution of it is reported in [64, 65, 82]. Once the results of the fit are known, the procedure calculates the muon momentum and the charge, that are used for the Kalman initialization step (see next paragraph), and in each drift tube station two points, obtained by this procedure, are inserted in the track.

3.3.1 Inizialization of the Kalman filter

The Kalman filter procedure starts fixing the values of the parameters in the state vector and its covariance matrix; the most common choice is to use infinite values. This means, that the values will converge to the most probable values, step by step in the procedure when the measurements are included. This choice of initial values requires a large number of measurements to permit the procedure to have enough steps to converge to correct values. In the case of OPERA, there are quite a limited number of points in the tracks, in particular for the short tracks the procedure can involve less than forty steps, not enough to converge to the correct value. Hence, in OPERA it is important to initialize the fit parameters to reasonable values in order that the Kalman filter converges to the correct values.

The first step of the Kalman filter depends on the topology of the events. In Fig. 3.3 the different event-topologies are illustrated, the events were divided into three categories:

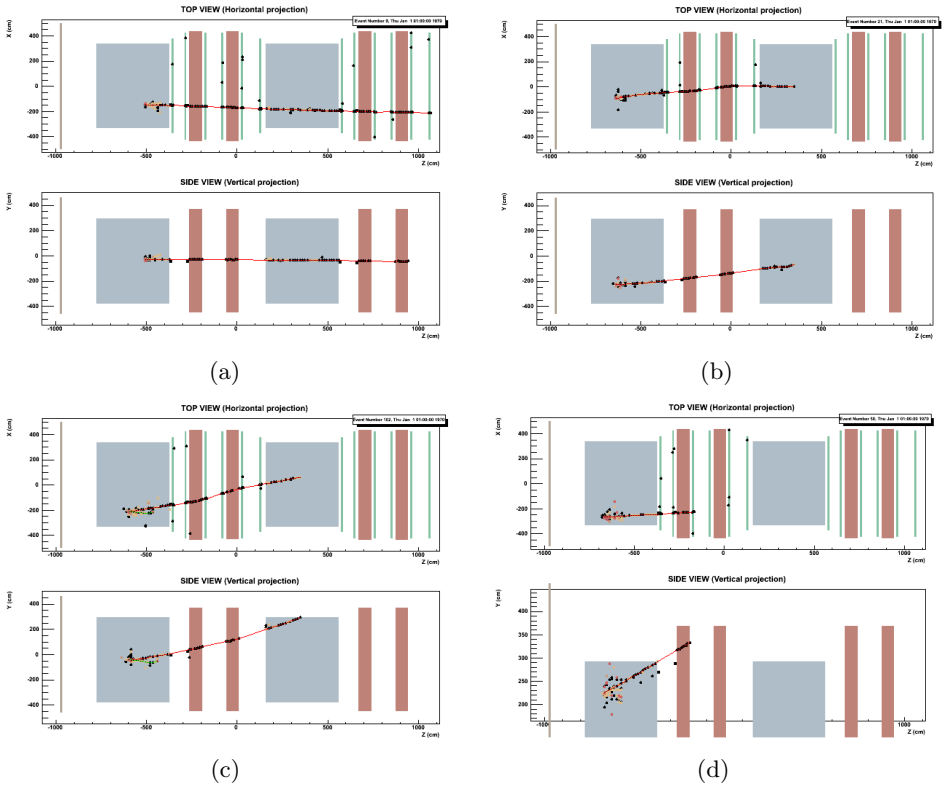

Figure 3.3: Different topologies of the tracks, used in the Kalman initialization step. In (a) a through-going track, in (b) a stopping one, in (c) a target initialization track, and in (d) a track wrongly initialized as stopping.

- *through-going tracks*: tracks exiting the detector after crossing a DT station (in most of the cases, the most downstream DT of the second SM). In this case the analysis of the last two DT stations is used to initialize the first step of the procedure.
- *stopping tracks*: tracks stopping inside the target or the RPC arms.
- *target initialization tracks*: tracks that exit the detector from the target sides, for which the estimation of the momentum from the DT can not be used.

To select the topologies of the tracks, a cut on the x and y coordinates for the last point in each coordinate is applied; the cut is set differently in each detector and also for different planes in the same detector.

For the cut the sensors (scintillator strips or strips in the RPC plane) closest to the edge of the detector on the side walls are used to select tracks stopping in the target; the cut limits the tracks not to have a signal in the last sensor at the border. This cut is used for all the detector planes, except for the first plane in each sub detector (TT or RPC arm); in these planes the geometrical cut is fixed to consider all the tracks with a signal in the last strip of the prevoius plane and a slope less than 15° (in the

through_going tracks	77.9%
stopping track	20.1%
target initial	2 %

Table 3.1: Fractions of the different topologies used to initialize the Kalman filter procedure for tracks reconstructed in the ν_μCC DIS sample of MC events.

(xz) or *(yz)* plane) as exiting the detector.

The selection of the tracks stopping in the detector can fail as shown in the Fig. 3.3(d), due to the inefficiency of the sensor (when the last sensor on the border is missing), or if the track crosses the holes inside of the RPC plane (that aren't considered in this procedure), or if the track at the border of the detectors have a slope bigger than 15°.

The fraction of the different selected topologies is shown in Table 3.1, for a sample of ν_μ CC DIS events.

Stopping Muons. For the track selected as stopping in the detector, the position and slope parameters in the vector P of the Kalman procedure are initialized after a rough linear fit of the last points included in the track, separately in the two views. The position error, in the covariance matrix, is set to the resolution of the coordinate measurement (depending on the detector), the slope errors, in the covariance matrix, are instead set to 45% for the horizontal coordinate and 60% for the vertical ones.

For the last element the charge sign is set to negative values (-1), the momentum to 200 MeV/c, corresponding to a muon range of half a brick for a muon, and the error in the covariance matrix to 60%. In Fig. 3.4 the distribution of the initial momentum p_{rec} relative to the true (MC) momentum p_{true} is shown; plotted is the variable called relative momentum difference or normalized momentum resolution, defined as:

$$(1/p_{rec} - 1/p_{true})/(1/p_{true}) \tag{3.30}$$

As we can see from this plot, due to the fact that the energy loss of the muon in half a brick is not Gaussian distributed, the distribution is slightly shifted, but this doesn't affect the final resolution of this sample, see section 3.4.1.

A problem for the reconstruction resolution are the tracks misidentified as stopping. Those tracks overlap with the events in overflow in the plot 3.4 . If the track is fully contained in the target of one SM (not crossing a spectrometer), there is no momentum measurement available for the initialization, which the Kalman procedure can correct (p is set to $200 MeV/c$). For tracks leaving the target, that are misidentified as stopping, the momentum obtained by the Kalman procedure will be wrong. The stopping point of these misidentified tracks is shown in Fig. 3.5: most of the tracks ended in the last plane of the subdetectors (TT or RPC), due to errors of the tracking procedure (bad connection between subdetectors) or due to the fact that the track crosses the holes between the chambers form the RPC plane. In this last case the track really disappeared for the detector.

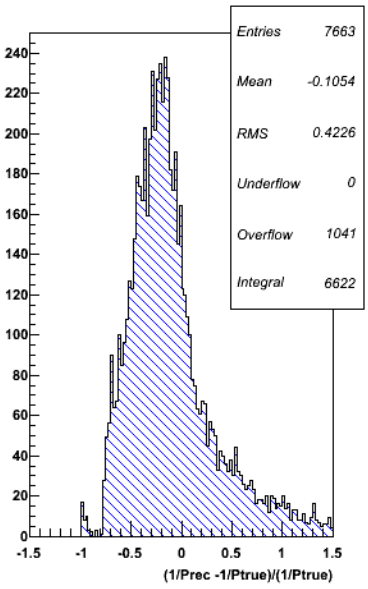

Figure 3.4: Distribution of the normalized resolution of the muon momentum p_{rec} used to initialize the stopping tracks.

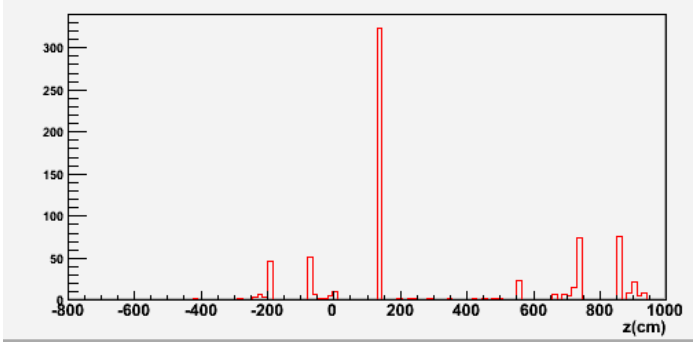

Figure 3.5: Z-coordinate of the stopping points for the wrongly inizialized stopping tracks.

Through-going muons. The initialization step of those tracks uses the result of the data analysis of the spectrometer arm to get a momentum estimation and the charge sign of the particle [64, 65, 82]. The momentum in the *(xz)* plane is obtained from the measurement of the $\Delta\phi$ angle (in the plane *(xz)*) between the last DT station included in the track and the prevoius one, due to the magnetic field of the spectrometer arm. Then, the total momentum of the particle is calculated with the slope of the track in the two planes *(xz)* and *(yz)*. If this method fails, a parabolic fit on the segment of the track inside the last RPC arm is performed. The error on the momentum is set to the resolution of the DT data fit: 30%.

The procedure has been tested for the ν_μCC-DIS events, as a function of the momentum, dividing the events into bins with a width of 2 GeV/c momentum; the resolution of all tracks is shown in Fig. 3.6(a) , and the mean and the sigma of the Gaussian fit made on each bin is shown in Figs. 3.6(b) and 3.6(c). The RMS of the normalized resolution of the momentum is about 30% for tracks with momentum in the range $3 - 30 GeV/c$ and the distribution is not shifted.

To get the sign of the charge, the sign of the angle difference $\Delta\phi$ of the track segment of two consecutive DT stations is used, relating it to the direction of the magnetic field. If the segment in the DT station between the two spectrometer arms is missing, it is not possible to apply this method (this happens in the MC in less than 0.1% of the cases), and a secondary approach has been developed. In fact, the displacement in the *(xz)* plane between the first and the last straight segment of the DT station, measured at the z-point in the middle of the DT missing station, has to be positive or negative, depending on the particle charge signs.

The efficiency of the charge sign determination is defined as the fraction of all reconstructed longest tracks, with the charge sign correctly inizialized (by default it is negative). This efficiency was studied with the MC muon sample, depending on energy and direction of the track [82], it is bigger than 99% for $p_\mu > 3GeV$. For the sample of ν_μCC-DIS events it has also been verified as a function of the momentum of the track, and the result is shown in Fig. 3.7.

Also the slope in the plane *(xz)* and the coordinate x is initialized using the result of this fit on the DT data, with the resolution of the DT (0.3 mm); the position y and the slope in the plane *(yz)* is obtained by a rough linear fit in the last segment of the track.

Target initialization tracks Different topologies of events are included in this group, so the procedure to inizialize them can be different; the position and the slope are initialized after a rough linear fit of the track, and for the momentum the curvature measured by the drift tube or from a parabolic fit on the last segment in the spectrometer is used.

3.3.2 Correction of bad points using the χ^2 of the filtered points

The Kalman filter is also used to correct possible reconstruction errors which happened in the tracking step. For this corrections the filtered χ^2_F, see eq. 3.9, of each point is used to determine the quality of the point in the track and to determine whether to

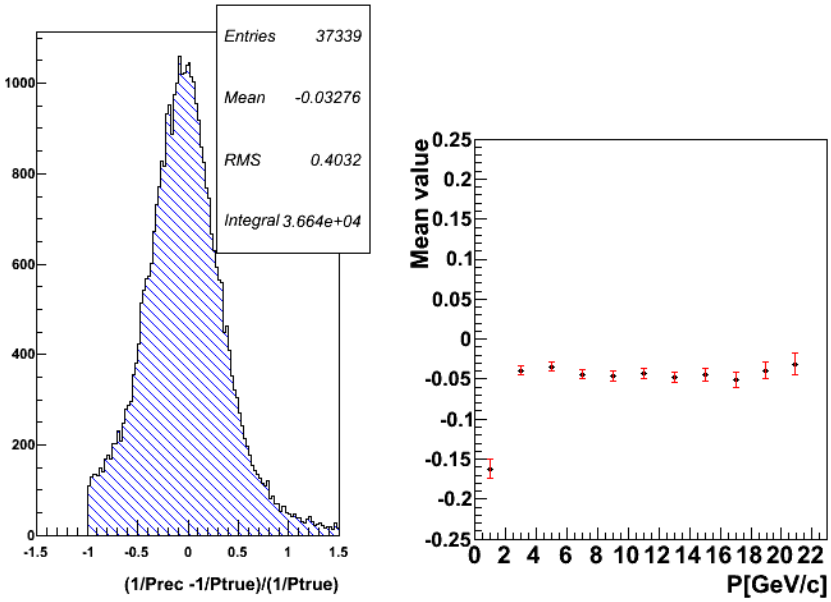

(a) (b)

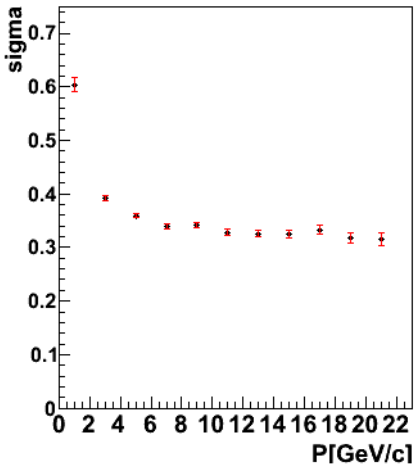

(c)

Figure 3.6: Distribution of the normalized resolution of the momentum for the tracks initialized as through-going; in (a) the resolution for all the tracks, in (b) the mean and in (c) the sigma (RMS) of the resolution distribution for differrent muon momenta (bin width of 2 GeV/c).

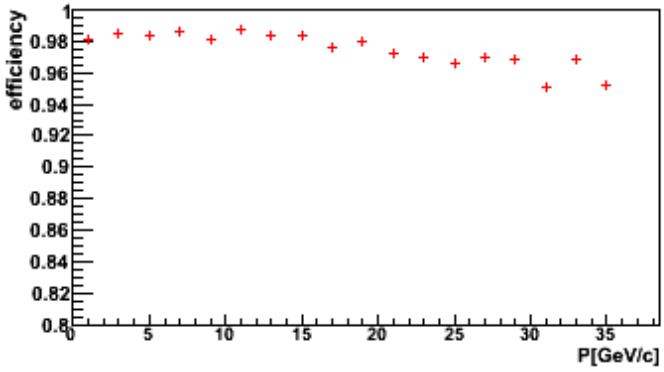

Figure 3.7: Efficiency of the charge identification for the through-going muon tracks as a function of the momentum.

keep it in the track or to try to substitute it: the cut on the χ^2-filtered point has been set to 5.

The procedure foresees that always at the end a point is inserted in the track, also in case the χ^2 is > 5, the "wrong" point is kept in the tracking prodecure; this is to avoid the possible loss of the track.

This procedure can be applied only to the RPC and TT points, due to the fact that the points coming from the DT detectors are not measured hits, but the reconstructed points obtained from the analysis of the DT data (see the dedicated paragraph).

The procedure to control and substitute the possible hit-point with large χ^2 in the track can be split into four steps:

- First of all, a list of possible points to be substituted is created from the list of all the hits in the event: with respect to the bad hit, all the points in the same plane and detector are selected, applying a cut on the distance between this point and the expectation obtained by the extrapolation step at this z position.
- For all the points in this list the filtering step is performed and the χ^2 of each point is calculated.
- From the list, including the point originally chosen by the tracking procedure, the point with the best χ^2 is selected; this is substituted in the track at the same z position. The choice to insert a point in the track also when the χ^2 is bigger than 5, if a better point doesn't exist, allows to keep the tracks reconstructed by the tracking package, and prevents to build tracks with a large number of hits missing, that corresponds to a large number of planes missing (due to the fact that almost one point for each plane is inserted in the track).

Step by step to improve the reconstruction, three additional procedures can be applied, depending on the topologies of the track:

- First of all a test is performed to look for hits in missing planes in the track. For each point it is verified if one plane, in the horizontal or vertical view, is

missing between this point and the previuos one in the track. In case of a missing point/plane a list of possible points belonging (to this plane), near to the expected track position is produced. To this list the procedure of slection of the best point is applied; the point with the best χ^2 is inserted in the track if its χ^2 is less than 5.

- A second procedure has been implemented to delete a hit in the track, also if no good substitute point exists. Before deleting the point, the procedure checks that by deleting this point the track will not be lost, by trying to delete the point and following the track with the next Kalman step: if there is a sufficient number of points in the track, also after deleting the bad point, the procedure can continue, with the bad point deleted; otherwise the procedure comes back to the problematic point, and proceedes without deleting it.

- A problem for the reconstruction of a track in the vertex region are hits from backscattering particles, which can wrongly be added to the track. To reduce the hits associated with back-scattering, a whole plane is removed from the track in case the first two points of the track belong to the same plane, but in two different views, and both have a χ^2 larger than the cut. Also, if the first point of the track is only seen in one view and has a large χ^2_F, it is deleted from the track.

3.4 Results of the track finding procedure and the Kalman filter

To test the reconstruction procedure, including tracking pattern and the Kalman filter, different MC samples have been simulated. The analyses of the reconstruction described in this and the following section have been done with the following samples:

- 50k ν_μ DIS CC events
- 50k ν_μ QE CC events
- 50k ν_μ NC events
- 10k $\overline{\nu}_\mu$ DIS events

The events are simulated with a random vertex in the lead target of OPERA; the geometry has been set to the filled target, except the first two planes in each SM, which corresponds to the official configuration at the beginnings of the first run. The neutrino energy spectrum is estimated taking into account the expectation of the CNGS, and the muon momentum depends on the simulated interaction considered.

The goal of the analysis is to verify the possibility of the software to reconstruct the muon track, i.e. for each event the muon (positive or negative charged) track identified by the OpRec routine is selected and analysed. In the NC events , the muon track reconstructed will be a fake, and it will give an estimation of the contamination of NC events in the CC real data. For the events with more than one muon track

reconstructed, only the longest one in each event will be selected. For the following analysis this selection will always be applied, unless clearly specified.

The reconstruction of the ν_μ CC events is discussed in section 3.4.1, includingwill be discussed in section first in this section, including the efficiency. FIrst the CC DIS sample is studied, then the main differenve to the CC QE events and the reconstruction capability for the QE events will be discussed. The contamination of the μ^- sample from NC and $\overline{\nu}_\mu$ CC events is presented in section3.4.2 and 3.4.3 respectively.

3.4.1 MC studies of the ν_μ CC sample

For the CC DIS sample the software obtains:

events simulated	50k
events with at least one 3-dim track reconstructed	96.6%
events with a $\mu-$ track reconstructed and identified	90.9%
events with a $\mu+$ track reconstructed and (mis)identified	2.3%

As shown in the table, in 3.4% of the analyzed events, no three-dimensional track could be reconstructed. There are several reasons for this failure: a low-energy event is contained in only a few planes, as is illustrated with the event of Fig. 3.8, or the procedure to merge the segments of the two views (*(xz)* and *(yz)* planes) fails. Especially, the merging procedure can fail, if in one view the track segment in a detector is not reconstructed, so that the lengths of the two-dimensional tracks are too different to be merged in a single track.

The identification of the muon track is based on the total material crossed by the particle; the variable used for this selection is the integrated track step length times the density of the material crossed in this step. A lower cut of $660 g/cm^2$ is applied to select the muon tracks. In 90.9% of the events a muon track is correctly reconstructed, and with respect to the events with at least one 3-dim track reconstructed, in 94.1% of the cases a muon track is identified.

This analysis has been made with the ν_μ CC DIS interactions in the OPERA target, so it is obvious that for the tracks identified as μ^+ the charge is misidentified. The misidentification of the muon charge is limited to 2.3% of the total number of events, and to 2.4% of the three-dimensional tracks reconstructed.

As already mentioned, the track is set to negative charge in the case of a stopping muon inside the detector (the Kalman procedure is initialized with negative charge by default). In the case of a stopping muon it is clear, that the charge identification is not accurate, hence we limited the sample to the tracks that cross the spectrometer (in the procedure applied to the tracks with the Kalman filter initializazion step, the value for the muon charge obtained by the DT measurement is used):

$\mu-$ tracks reconstructed and identified crossing the DT	98%
$\mu+$ track reconstructed and (mis)identified crossing the DT	2.0%

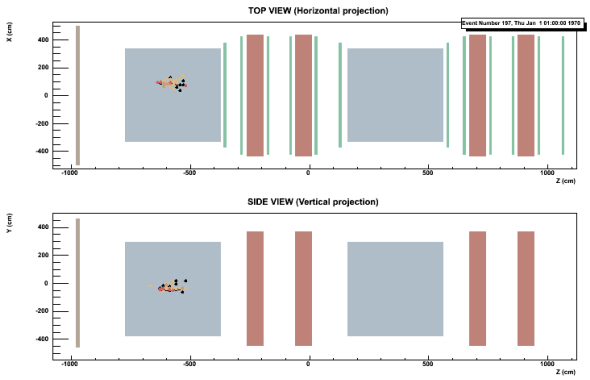

Figure 3.8: Low energy CC-DIS event without three-dimensional track reconstructed.

For these tracks the misidentification of the muon charge is limited to 2%.

In the following part of the section, the resolution for the five parameters estimated by the Kalman filter will be described, separately for each parameter. The estimation of the momentum, the slope and the position is made at the beginning of the track, in the vertex region; this is because in OPERA the goal of the reconstruction with the elctronic detector is to have a monitoring of the beam and to identify the brick in which the interactions occurred. All the comparisons have been made considering the true MC value of the muon track exiting from the primary vertex and the reconstructed MC track.

Resolution of the reconstructed position. The first two parameters of the vector P (the state vector of the Kalman filter) are the coordinates x,y of the track position at the beginning of the track; these correspond , if the track is correctly reconstructed, to the first hits in the electronic detector after the interaction vertex, given by the muon. This point *(x,y)* is considered as the origin of the track, at the z position of the first TT plane included in the track. These estimated coordiantes are used to extrapolate the position of the track on the CS, to set the region that has to scanned.

The position on the CS from the extrapolation of the reconstructed muon track is compared to the muon position on the CS from the MC truth. The comparison is only made with three-dimensinal tracks identified as muons with the correct first plane of the track reconstructed. The extrapolation is done using the slope of the track in the *(xz)* and *(yz)* planes estimated by the Kalman filter at the beginning of the track. The errors on the position are obtained from the covariance matrix of the Kalman filter at this point, including the error of the slope and its correlation with the position.

Fig. 3.9 shows the difference between the first TT plane of an identified muon track and the first TT plane hit by the muon from the MC truth, for muon tracks with a wrong reconstructed first TT plane (15.5%). The failure to reconstruct the correct first TT plane is mainly due to backscatttering points added to the track (negative difference in Fig. 3.9) and to tracks where the reconstruction stops before reaching the true starting point, in the latter case the difference is positive and in most cases the

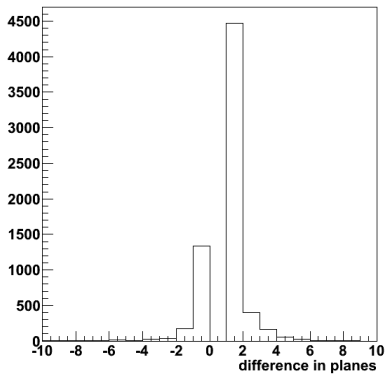

Figure 3.9: Difference in TT planes between the true first TT plane after the interaction and the TT plane of the first point of the muon track for the 15.5% of muon tracks with a wrong first TT plane reconstructed.

difference is one plane.

Considering the sample of positive muons reconstructed and identified, the following results were obtained:

muon track with correct first plane reconstructed	84.5%
muon track with wrong first plane reconstructed	15.5%

The difference between the true position on the CS and the position on the CS extrapolated from the Kalman prediction are reported in Figs. 3.10(a) and 3.10(b), for the coordinates x and y, and for the the distance in the xy plane between the true point and the extrapolated is shown in Fig. 3.11.

The estimated postion on the CS is not shifted, and the resolution (RMS) is better for the x-coordinate (about $7.5mm$), than for the y-coordinate, (about $9.5mm$), due to the fact that the x coordinate is estimated including the DT measurement, with very good resolution. This explains also the non-Gaussian distribution and the difference between the distribution for the x-coordinate with respect to the y-coordinate. From the plot on the right of Figs. 3.10(a) and 3.10(b), it follows that the position errors are underestimated for both coordinates. In Fig. 3.12 the resolution (RMS) of the position is plotted as a function of the TT plane, for both coordinates; it doesn't depend on the z position for the y-coordinate, however for the x it decreases in the last planes of the TT due to the effect of the better DT resolution. The same behavoiur is seen in Fig. 3.13, for the position errors: the errors of the x position decreases in the last planes of the TT.

Due to the fact that the scanning region in the CS is fixed to $2 \times 3cm^2$ for the CC events, in Fig 3.14 the distance between the estimated position and the true position is plotted in the region limited by the scanning; 82% of the selected tracks (muon track reconstructed and identified, with true MC signal on the CS and first plane correct reconstructed), are found in the scanning region, these events correspond to 60% of

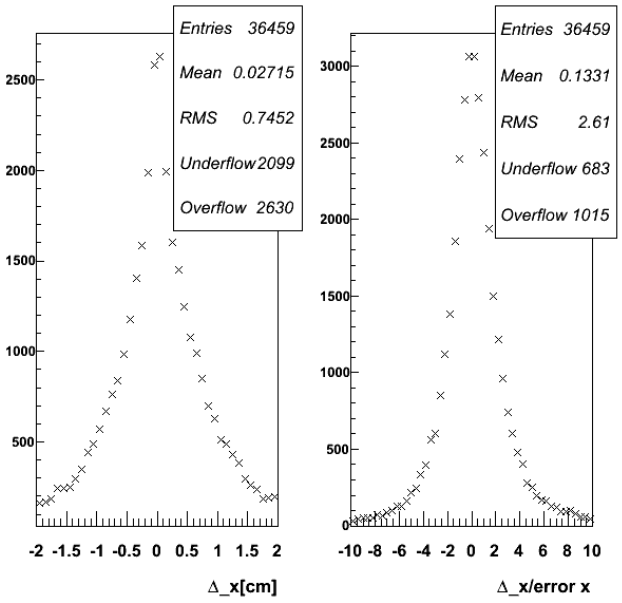

(a)

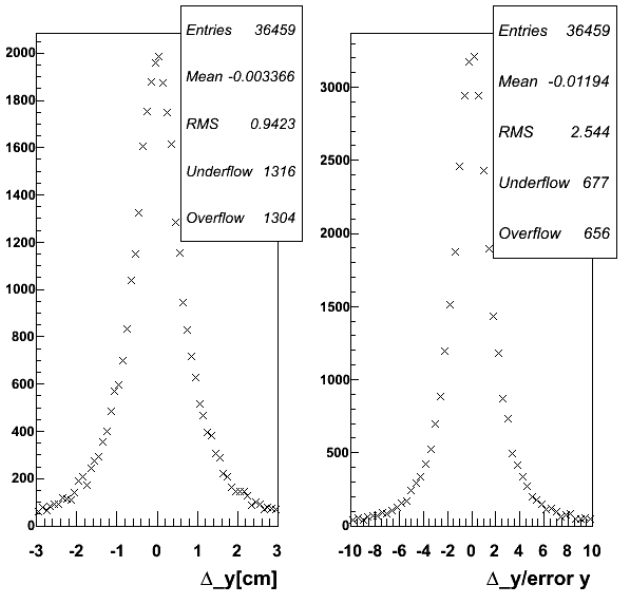

(b)

Figure 3.10: (Left): difference in position (cm) between the true position and the postion extrapolated from the Kalman filter on the CS, and (right): the ratio between this difference and the estimated position error; in (a) for the x coordinate and in (b) for the y coordinate.

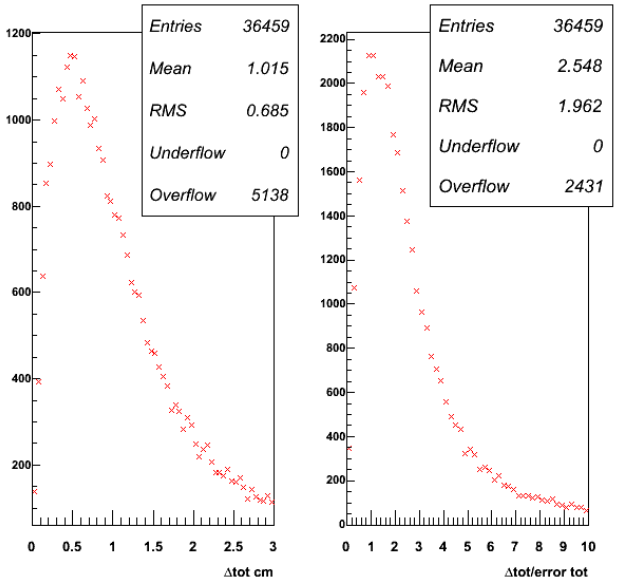

Figure 3.11: Distance in cm between the true position and the position extrapolated from the Kalman results on the CS on the left, and the ratio between this distance and the estimated position error on the right.

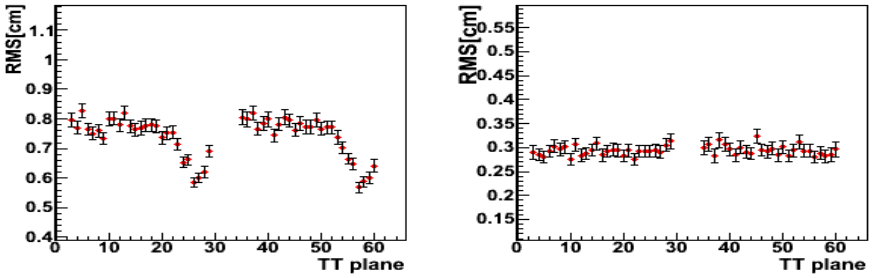

Figure 3.12: RMS of the distribution of the difference between the true position on the CS and the extrapolated position from the Kalman results as function of the TT plane, on the left for the x-coordinate and on the the rigth for the y-coordinate. The error bars are the fit errors of the RMS value.

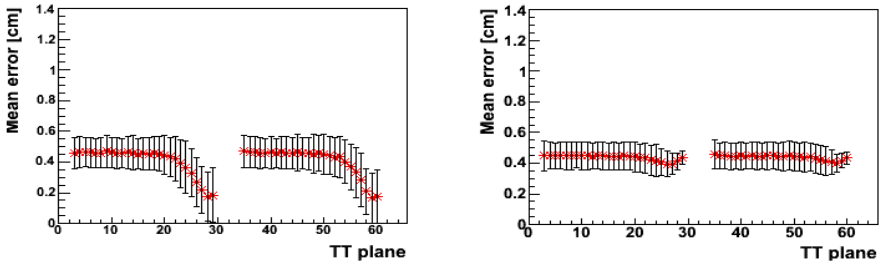

Figure 3.13: Error of the estimated position on the CS obtained by the Kalman filter; on the left for the x-coordinate and on the right for the y-coordinate.

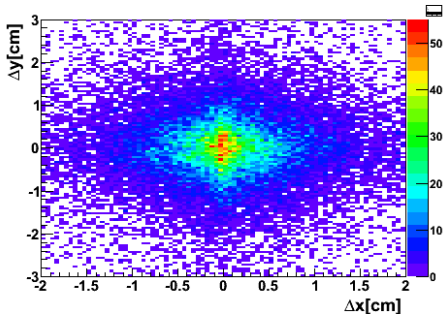

Figure 3.14: Scatter plot of the true hits on the CS relative to the position predicted by the Kalman filter.

all ν_μ DIS CC interactions simulated. However, part of the events can be recovered by the fact that a specific procedure to correct the wrong first plane of the track (wall finding) is applied in the brick finding procedure.

Resolution of the muon slope. The resolution of the angle in the *(xz)* and *(yz)* plane for the reconstructed tracks identified as a muon are plotted in Fig. 3.15(a) and 3.15(b). The angle is quite well reconstructed in both planes, with a RMS of both distributions of about 15 *mrad*. The reconstructed angle is not shifted. The incoming neutrino beam is simulated to have an angle of 3° to the horizontal plane, to be consistent whit the CNGS features; the mean of the angle distribution of the muon track in this projection is 2.8°, confirming the good reconstruction. The errors of the angle (obtained from the Kalman covariance matrix) is slightly underestimated, as is seen in the right plots of Fig. 3.15(a) and Fig. 3.15(b): the RMS of the normalized slope difference is about 1.6.

Normalized resolution of the momentum The normalized resolution of the momentum is defined in eq. 3.30, the MC true value of the momentum is taken at the interaction vertex, the reconstructed momentum is estimated at the first electronic detector plane of the reconstructed track. This means that a small bias is introduced for the momentum determination, due to the energy loss of the muon in the brick in which the interaction occurred. The resolution is plotted separately for stopping and through-going muons (following the definition given in section 3.3.1), and for the through-going muons as function of the track momentum.

For the through-going tracks, the resolution is shown in Fig. 3.16(a), a small bias in the reconstructed momentum is observed, that decreases with decreasing momentum, and remains, in any case, below 5% for the interesting momentum range. The RMS remains under 20% in the interesting region, and improves for low momentum tracks. The error of the momentum is reported in Fig. 3.17, it is underestimated.

In Fig. 3.18 the muon momentum resolution for stopping tracks is reported for all the momenta; the resolution is clearly better than for the through-going events, due to the fact that the initial momentum in this case is well known; the RMS of the distribution is about 9%. The large number of events with a momentum not well

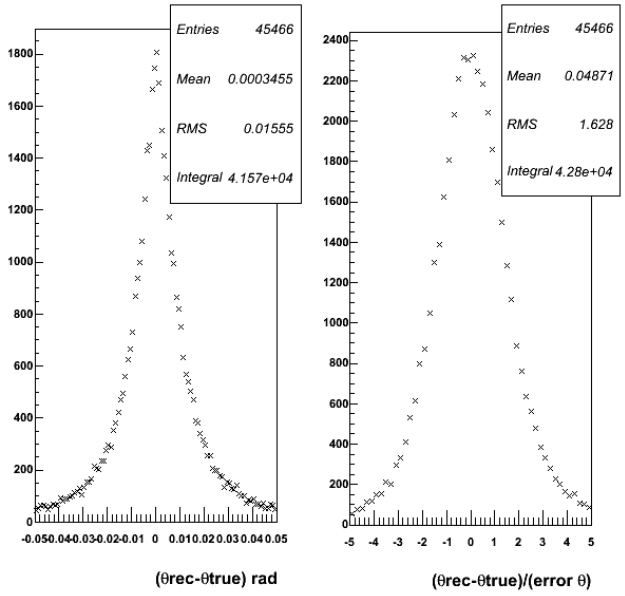

(a)

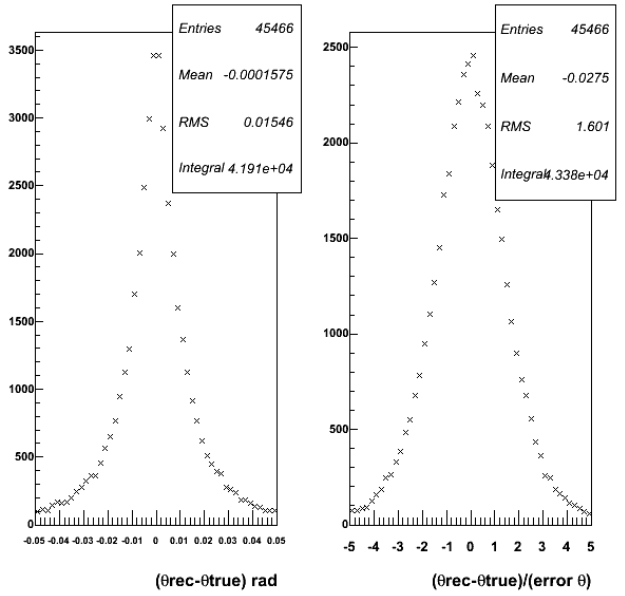

(b)

Figure 3.15: Resolution of the slope measurement of muon tracks. (left) Difference of the true (MC) and the reconstructed slope, (right) difference of the reconstructed and the true slope, normalized to the error of the slope, in (a) for the *(xz)* plane and in (b) for the *(yz)* plane.

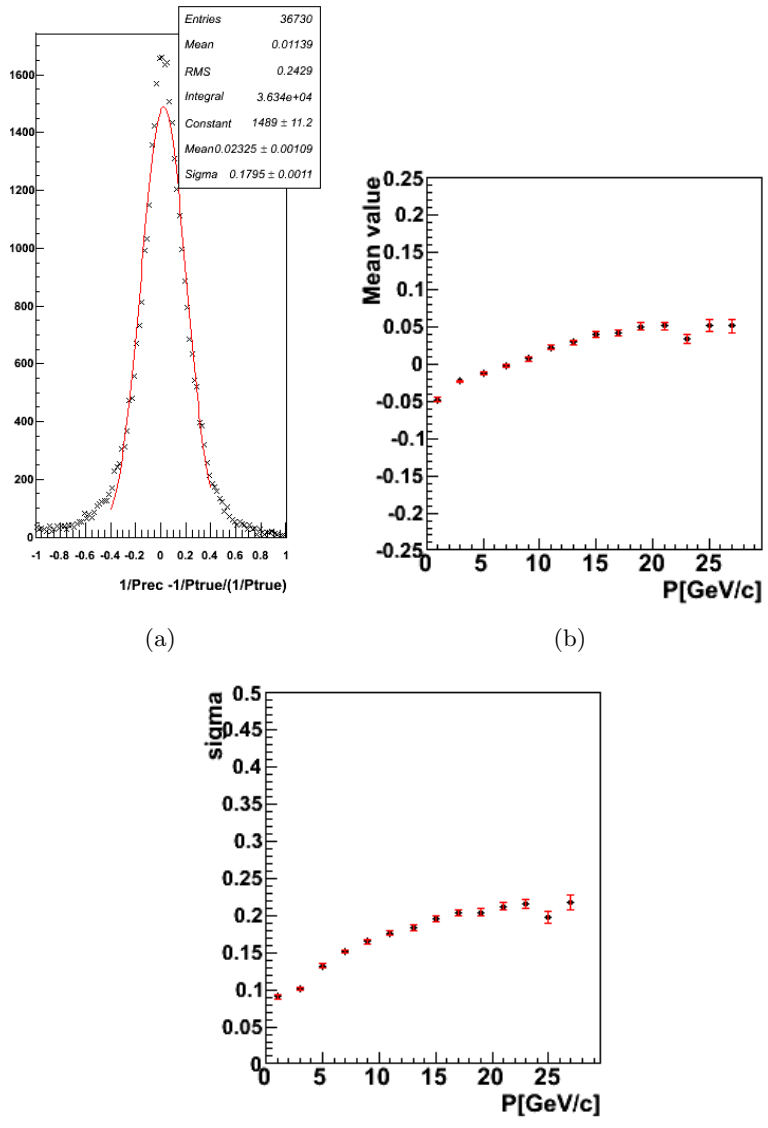

(a) (b)

(c)

Figure 3.16: Muon momentum resolution for through-going tracks, in (a) for all through-going muon tracks, in (b) the mean value and in (c) the sigma (RMS) of the resolution as a function of the muon momentum (the bin width is 2 GeV/c).

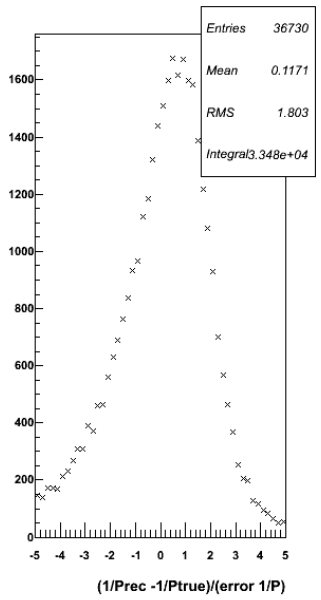

Figure 3.17: Muon momentum resolution normalized to the momentum error (obtained from the Kalman filter covariance matrix) for through-going tracks.

reconstructed is due to the tracks wrongly identified and initialized in the Kalman filter as stopping, that are in fact muon tracks exiting from the detector, as explained in the paragraph on the Kalman filter initialization. The error in this case in not well estimated (see Fig. 3.18), due to the bigger effect of the multiple scattering.

Muon track length. Another important parameter to check the capability of the track reconstruction, is the length of the track, especially because the length $\times$ density is the main parameter used to identified the muons. In Fig. 3.19(a) the distribution of longitudinal lengths of the tracks identified as muons is shown; where the longitudinal length is defined as the difference between the z position of the last and the first hit of the track.

The distribution of the density $\times$ length crossed by the muon is shown in Fig. 3.19(b), the length in this case takes into account the path of the three-dimensional track in space, and the density of the material crossed, taken into account by the Kalman filter.

Both distributions show a clear structure with two bumps, associated with the tracks generated in the target of the two SM; the MC events were in fact generated only inside the lead target.

Muon track reconstruction efficiency

Two different efficiencies for the track reconstruction have been defined to get an estimation for the goodness of the reconstruction: the hit efficiency and the track efficiency. Both these efficiencies have been studied for all the tracks reconstructed

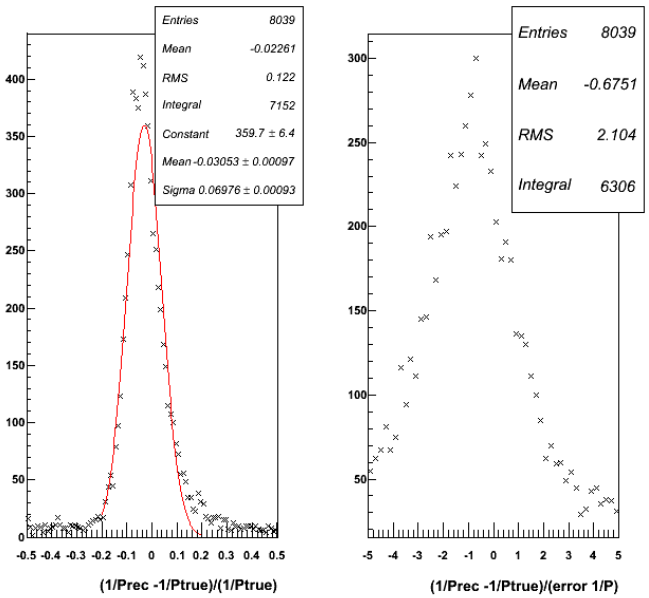

(a) (b)

Figure 3.18: On the left the normalized resolution of the momentum for stopping muon tracks, on the right the resolution normalized to the momentum error for the same tracks.

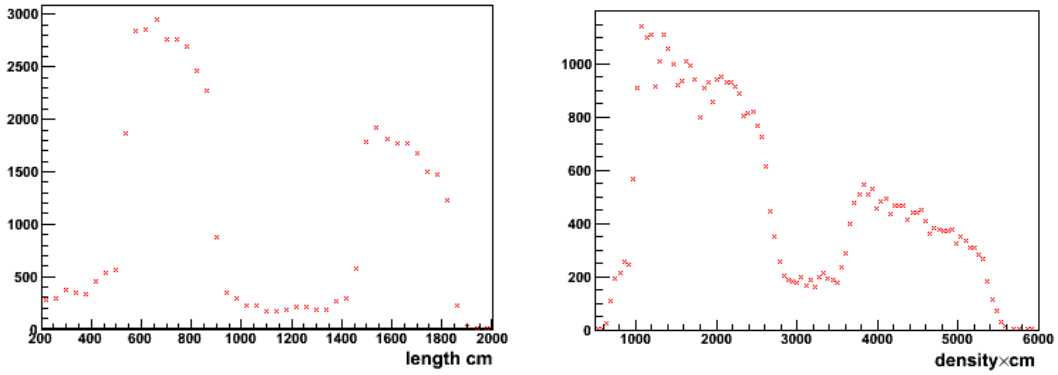

(a) (b)

Figure 3.19: In (a) the track length distribution of the tracks identified as muons for the CC DIS sample is shown, and in (b) the length × density for the same tracks $[g/cm^2]$.

and identified as muon, the missing tracks (tracks not reconstructed), and the missing points in the reconstructed tracks have not been taken into account.

For the hit matching of all the reconstructed tracks, the MC true information has been compared for each hit included in the muon tracks, to verify that the hit was really generated by the muon. It will be referred to as *hit efficiency* and has been defined as:

$$\epsilon_{hit} = \frac{total\ number\ of\ points\ generated\ by\ the\ muon\ in\ all\ the\ muon\ tracks\ identified}{total\ number\ of\ points\ on\ all\ muon\ tracks\ identified} \tag{3.31}$$

This efficiency is clearly not related to a single track, and has been calculated for different samples of tracks, as will be shown later. Due to the track building procedure, only the hits from TT and RPC are included in this analysis.

A second efficiency is used to estimate the goodness of the reconstruction, called track efficiency:

$$\epsilon_{track} = 1 - \frac{total\ number\ of\ wrongly\ identified\ muon\ tracks}{total\ number\ of\ identified\ muon\ tracks} \tag{3.32}$$

where a track is defined as wrong, if it has less than 70% of correct hits, following the definition of correct hit given for the previous efficiency. A track wrongly reconstructed is defined as ghost track.

These efficiencies have been plotted for the CC DIS sample, the mean hit efficiency for the identified muon tracks is 94.1%. In Fig. 3.20 both efficiencies are plotted for different values of the track momentum, about 98.5% and 99.5% for the hit efficiency and the track efficiency are reached for momenta bigger than 10 GeV/c.

The low momentum tracks are not really well reconstructed, in fact, the efficiency drops to less than 60%; those tracks in the CC DIS sample are generally short and contained inside the hadron shower around the vertex, so that it is generally difficult to distinguish the muon track from the other hadronic short tracks.

This is also confirmed analysing both efficiencies as a function of the longitudinal length of the track, plotted in Fig. 3.21(a); the efficiencies drop for the short tracks. The long tracks are in general more simple to reconstruct, also because they cross the RPC, which have less hits.

The efficiencies are plotted also as function of the starting point of the muon track reconstructed, see Fig. 3.21(b), no bias correlated to the starting position is visible, they depend mainly on the length of the track and not on the starting point. The efficiencies are slightly smaller for the tracks starting in the first target tracker planes, especially in the second SM, this is due to some inefficiencies of connection between the different parts of the track in the two SM.

Reconstruction of CC QE events

To understand the reconstruction capability for all the event topologies in OPERA, the same analysis as for the CC DIS events, has been applied to the CC QE events. These

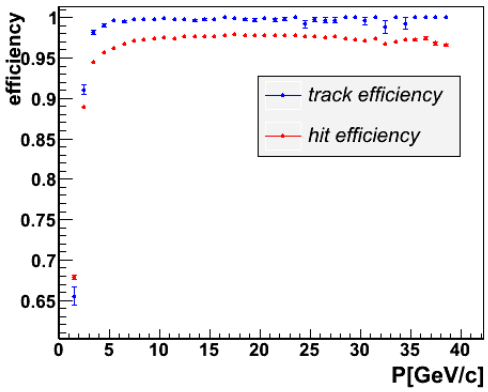

Figure 3.20: Hit efficiency (red) and track efficiency (blue) for the identified muon tracks, as a function of the muon momentum of the track for CC DIS events.

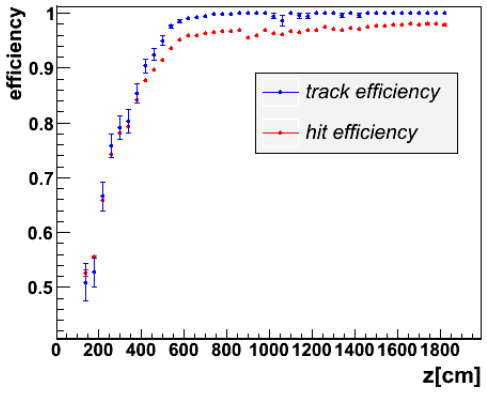

(a)

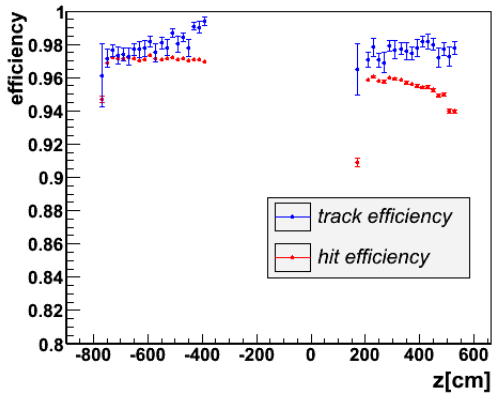

(b)

Figure 3.21: Hit efficiency and track efficiency for the muon identified tracks as a function of the longitudinal length in (a) and as function of the starting point of the track in (b), for the ν_μ CC DIS sample.

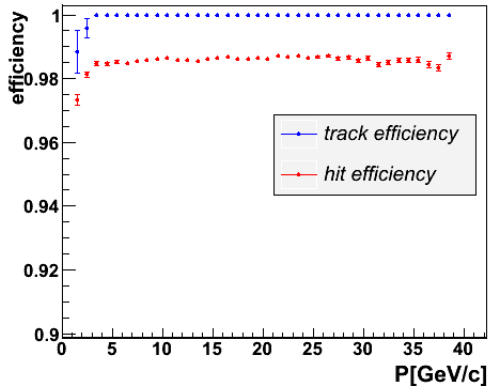

Figure 3.22: Hit efficiency and track efficiency for the identified muon tracks as a function of the muon momentum for the ν_μ CC QE events.

events are characterized by a muon track and no hadronic shower or low deposited energy in the interaction vertex region.

The reconstruction of the ν_μ CC QE events is simpler than the ν_μ CC DIS events, and this implies a better muon identification, in fact, for this sample the reconstruction software package obtains:

events simulated	50k
events with at least one μ track reconstructed	98.8%
events with a $\mu-$ track reconstructed and identified	98.5%
events with a $\mu+$ track reconstructed and (mis)identified	0.9%

Limiting the sample to the tracks that cross the spectrometer (selected as through-going tracks in the Kalman filter initializazion step):

$\mu-$ tracks reconstructed and identified crossing the DT	99.1%
$\mu+$ track reconstructed and (mis)identified crossing the DT	0.9%

For these tracks the misidentification of the muon charge is limited to 1%; the reconstruction software works really well, due to the fact that the events are in most cases characterized only by the muon tracks. The efficiencies, as previously defined, are shown in Figs. 3.22, 3.23(a) and 3.23(b). For these events the mean hit efficiency for all the sample is 98.5%, in general the efficiencies are both bigger than 95% for all the muon momenta, and track lengths.

The muon normalized resolution of the momentum for the through-going tracks from QE events is plotted in Fig. 3.24(a), it is compatible with the ν_μ CC DIS sample.

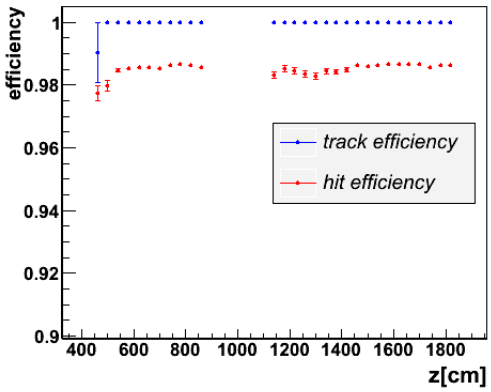

(a)

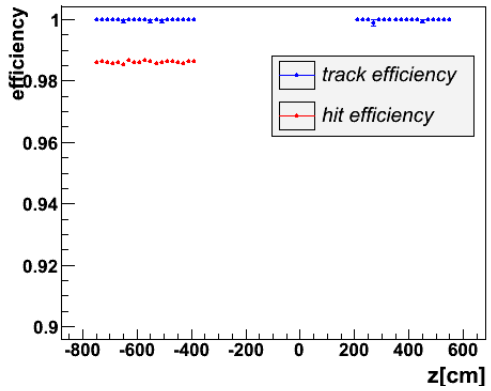

(b)

Figure 3.23: Hit efficiency and track efficiency for the identified muon tracks as a function of the longitudinal length on the left and as function of the starting point of the track on the right, for the ν_μ CC QE sample.

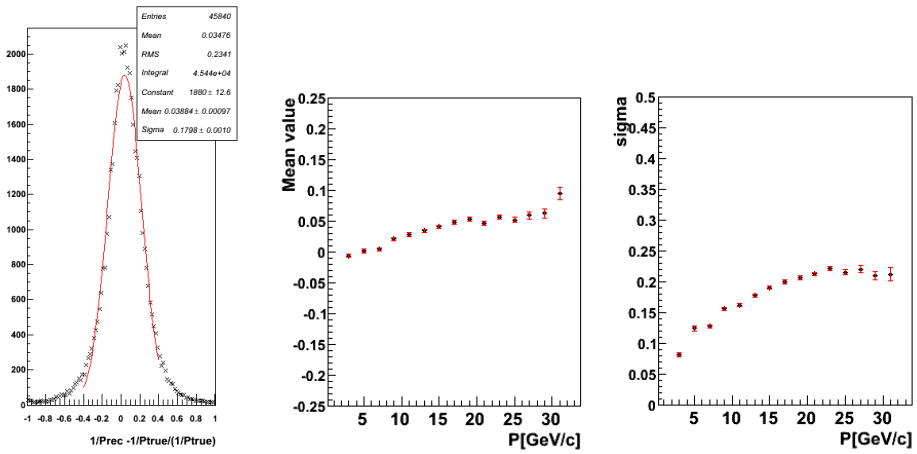

(a) (b)

Figure 3.24: Muon normalized resolution of the momentum for through-going tracks, in (a) for all the muon tracks and in (b) the mean and the sigma of the resolution distribution for different track momenta for CC QE events is shown.

3.4.2 MC studies of the NC sample

A sample of 50k ν_μ NC events was studied to understand the possible misidentification of NC events as CC events due to the software reconstruction. The analysis of this sample shows that the neutral current contamination is quite big, in fact in 10% of the NC events at least one muon track is (mis)identified and they are classified as CC events:

events simulated	50k
events with at least one 3-dim track reconstructed	39.6%
events with a $\mu-$ track reconstructed and mis-identified	10.9%
events with a $\mu+$ track reconstructed and mis-identified	3.5%

The muon momentum spectrum of the misidentified tracks is plotted in Fig. 3.25, all the events are well contained in the range $p < 6$ GeV/c, as was predicted. The length of the misidentified tracks is shown in Fig. 3.26(a) and also the length $\times$ density in Fig. 3.26(b).

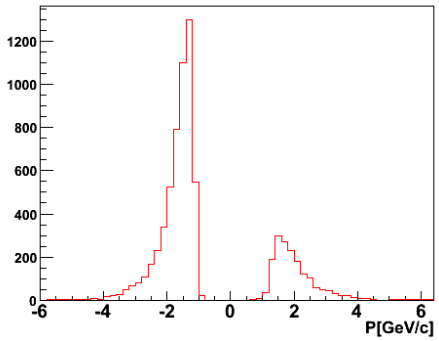

Figure 3.25: Muon momentum spectrum × charge sign of the tracks misidentified as muons in the NC sample (MC).

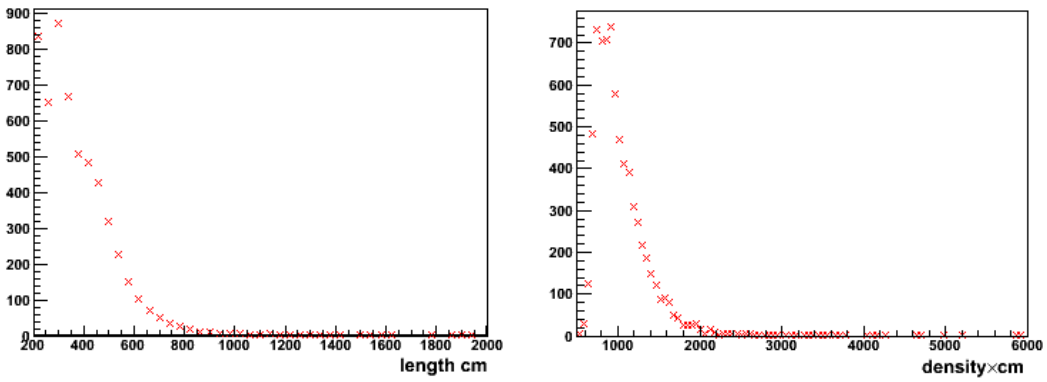

(a) (b)

Figure 3.26: In (a) the track length distribution of the (mis)identified muon tracks for the NC sample, and in (b) the length × density for the same tracks is shown.

3.4.3 MC studies of the $\overline{\nu}$ CC sample

The same analysis has been applied also on a sample of 10k $\overline{\nu}_\mu$ DIS events, obtaining:

events simulated	10k
events with at least one 3-dim track reconstructed	88.6%
events with a $\mu-$ track reconstructed and mis-identified	3.9%
events with a $\mu+$ track reconstructed and identified	84.0%

The contamination of negative misidentified muon tracks due to the $\overline{\nu}$ CC interaction is limited to 3.9% of the total antineutrino events, and decreases to 3.2% when only tracks crossing the DT are taken into account:

$\mu-$ tracks reconstructed and (mis)-identified crossing the DT	3.2%
$\mu+$ track reconstructed and identified crossing the DT	96.8%

Chapter 4

Data analysis and comparison with MC simulations

The OPERA experiment is running since 2008, the short runs in 2006 and 2007 were only commissioning runs, 2006 without and 2007 with very few bricks inserted in the target. The CNGS beam during three years of data taking (2008, 2009, 2010) didn't reach the official goal of $4.5*10^{19}$ $p.o.t/year$, however, it runs with quite high efficiency, in different ranges of p.o.t per extraction. The total efficiency of the CNGS beam in the last year reached 79.5%, the highest one reached in the OPERA data taking. The previous years, due to some weeks of stop for technical problems, CNGS collected $1.78 \times 10^{19} p.o.t$ during the year 2008, and $3.52 \times 10^{19} p.o.t$ during the year 2009, with an average CNGS efficiency of 60.9% and 72.9% respectively.

The DAQ system [83, 84] was running without problems during these three years, with a lifetime efficiency near to 100%. The trigger for data taking depends on the run-condition. During the CNGS beam spill the detector runs in a so-called triggerless mode: a filter at the level of the subdetectors is applied to reduce the noise. The filter consists of two main parts, the TT and the muon spectrometer filter; in the muon spectrometer the signal in at least two stations is required, where a station consists of three planes; and in the TT hits in the x and y projections of at least two TT planes or a TT plane with the sum of the photomultiplier signals exceeding 1500 ADC counts are required. As already mentioned, the selection of the on-time events is made using the GPS time-synchronization with the beam spill. In the case of ν_μ events, with a muon track in the final state, the trigger efficiency of the DAQ system, estimated with MC methods, exceeds 99 %.

The CNGS beam p.o.t integrated during the run and the events collected in the bricks are summarized in Tab. 4.4, and reported in Fig. 4.1; the selection is explained in the next section.

4.1 Selection of the ν_μ CC events

Only the events on-time with the CNGS beam spill are taken into account for the analysis, their selection has been discussed in section 2.3; they are reconstructed with

year beam	days	p.o.t.	CNGS eff	events in the bricks
2008	123	1.78×10^{19}	60.9%	1698
2009	155	3.52×10^{19}	72.9%	3693
2010	187	4.04×10^{19}	79.5%	4248

Table 4.1: Events collected by the OPERA experiment in the three years of data taking.

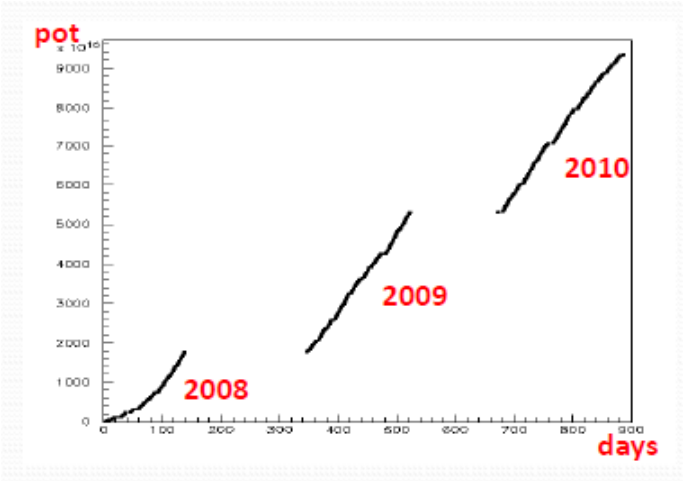

Figure 4.1: The *p.o.t* collected by CNGS in the three years of OPERA data taking.

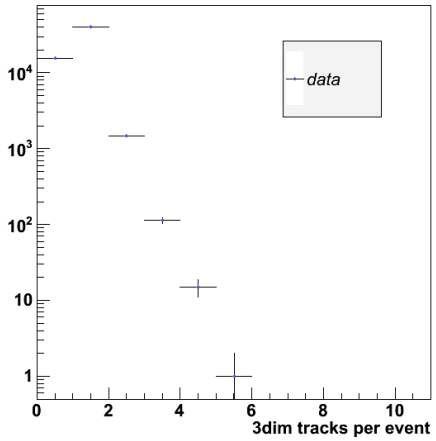

Figure 4.2: Number of three-dimensional tracks reconstructed for each on-time event collected in OPERA.

the software explained in the previous chapter. Then, the events are analysed to separate the events with the interaction in the OPERA target from the muon tracks due to interactions in the rock surrounding the detector and the events having the vertex in the spectrometer material.

The following table summarizes the events on-time collected by the DAQ system and the events in the OPERA target in the three years of data taking:

year	on-time events collected	CC events	target events	MC expectation
2008	10141	7276	1709	1848.4
2009	21455	15185	3559	3655.2
2010	25492	17443	4201	4195.2

The following analysis will be focused on the three-dimensional tracks reconstructed, in particular on the longest track identified as a muon in the event. The events without a three-dimensional track will not be considered. In Fig. 4.2 the multiplicity of the reconstructed three-dimensional tracks per event is plotted. As expected, most events have one three-dimensional track reconstructed.

In Fig. 4.3 the starting point of the longest three-dimensional track reconstructed in the event is plotted: most of the events have the starting point of the track in the first TT planes in the SM1. The events due to interactions with the vertex external to the OPERA detector are reconstructed in the first part of the SM1, and this leads to the distribution in Fig. 4.3, with a lot of events in the first part of the detector; this will become clear comparing this plot with the same distribution made for the selected contained events, shown in the next sections. Most of these events in the first TT planes of the first SM are clearly muon tracks produced in neutrino beam interactions in the rock and in the material placed before the detector, in which a muon track is produced and triggered the detector.

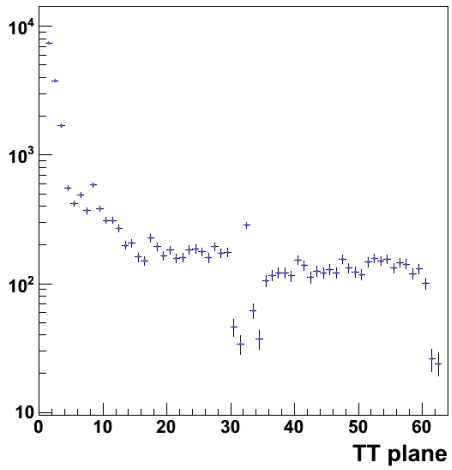

Figure 4.3: TT plane (z-position) of the starting point of the longest track reconstructed and identified as a muon for the on-time events.

The starting point of the muon (longest track reconstructed in the detector) in the transverse *(x,y)* plane is plotted in Fig. 4.4, and in Fig. 4.5 for the two coordinates separately. The *x,y* positions are obtained by the Kalman filter fit at the position z of the first point inserted in the track. The starting points reconstructed in the *x,y* coordinate view occupy a transverse plane bigger than the TT planes, and cover the RPC transverse dimension plane. The events with the interaction vertex in the rock and entering the detector in the spectrometer, have the starting point of the track reconstructed at the edge of the RPC plane.

The x-position can be considered uniformly distributed, as expected, inside the dimension of the TT plane; the entries near ± 400 cm represent the tracks entering in the spectrometer; the muon tracks entering the detector from the side of the TT occupy the two peaks around ± 350 cm. In the plot of the y-coordinate the two peaks near 400 cm represent, respectively, the lower limit of the TT plane and the RPC plane; due to the slope of the beam of $\sim 3^\circ$ to the horizontal, the muon track generated in an external interaction enters the detector from the bottom, so that the two peaks contain the tracks generated in the events occurring outside the target.

The events expected in the OPERA target are simulated taking into account the different fractions of CC-DIS, CC-QE and CC-RES, in the lead of the bricks and in the plastic scintillator of the TT. The same expectations in lead and plastic scintillator have been calculated for the NC ν_μ events, and for those the fraction of events mis-identified as CC. The fraction of CC-DISevents expected, taking into account the non-isoscalarity of the target, is more than 90% [85] of the CC events; the NC events are expected to be 29% of the $\nu_\mu CC$ events, and the CC $\overline{\nu}_\mu$ contamination is 2.1%. The expected number of $\nu_\mu CC$ interactions (without contamination) is $614 CC/kton/10^{19} p.o.t.$ [55]. The expected number of events, for each year separatly, has been normalized to the collected p.o.t.. The error on the expected number of ν_μCC events is due to the uncertainty on the total beam flux [86] and on the ν_μCC cross section, and can be considered to be

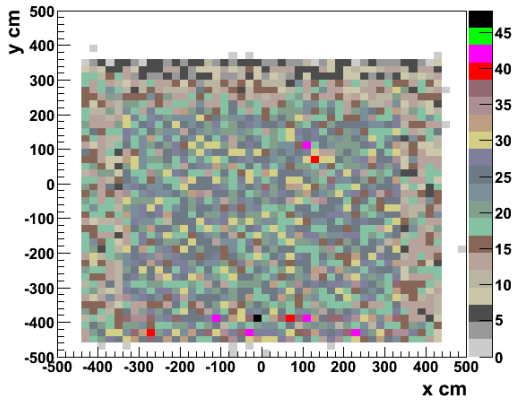

Figure 4.4: X-Y position for the starting point of the longest track reconstructed and identified as a muon for the on-time events.

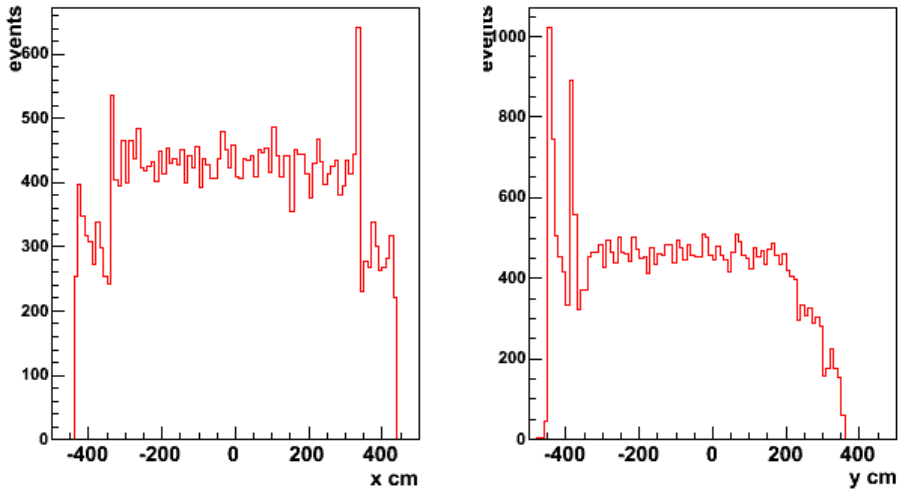

Figure 4.5: X-Y distribution for the starting point of the longest track reconstructed and identified as a muon for the on-time events, separately for the two coordinates, x(horizontal) on the left and y (vertical) on the right (see text).

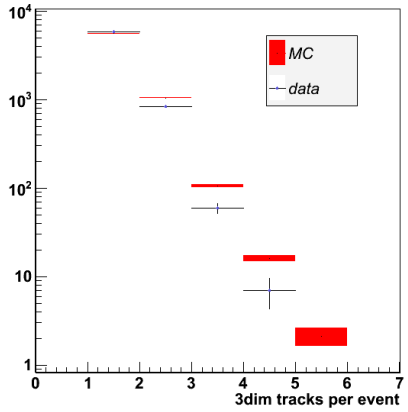

Figure 4.6: Number of three-dimensional tracks reconstructed for each on-time event identified as CC contained event. Red bares are MC results, points with errors are the data.

within ±10%. In the Tab. 4.4 the expected number of events calculated is reported for each year of data taking and compared to the data. The expectations are in good agreement with the data.

4.2 Analysis of contained CC events

The following analysis has been performed for the CC contained events, with at least one muon track identified. The MC expectation plot will be normalized to the events expected for the collected p.o.t in the respective plot; the errors, when not specified differently, are the statistical errors only.

In the Fig. 4.6 the number of three-dimensional tracks per event is plotted, the number of reconstructed tracks in the data is slightly smaller than in the MC simulation. The mean number of three-dimensional reconstructed tracks per event is 1.13 for the data, compared to 1.17 expected by the MC analysis.

The TT plane of the starting point of the reconstructed contained muon track is plotted in Fig. 4.7, together with the MC expectation, the errors reported are the statistical ones. As expected, the distribution is flat, except for missing events in the first two planes of both SM, which is due to the fact, that they are not filled with bricks. For the same reason the vertex of the track should not be reconstructed in the last TT planes in both SM. For the last two TT planes in both SM the reconstruction software has an inefficiency due to the fact that the track is formed by adding different segments in the sub-detector, if in one detector the number of hits is not enough to form a segment (< 3), the points in this detecor are not added to the track; to solve this problem, a procedure to add a point to the track, if its position is compatible with the slope of the track, has been added.

The reconstructed position in the transverse (x,y)-plane is obtained by the Kalman filter fit at the beginning of the track (z position of the first point included in the track

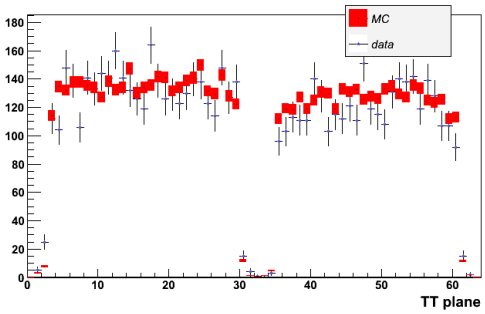

Figure 4.7: TT plane of the starting point of the muon track reconstructed in the CC contained events. Red boxes are MC expectation, points with errors bars are the data; the errors are statistical only.

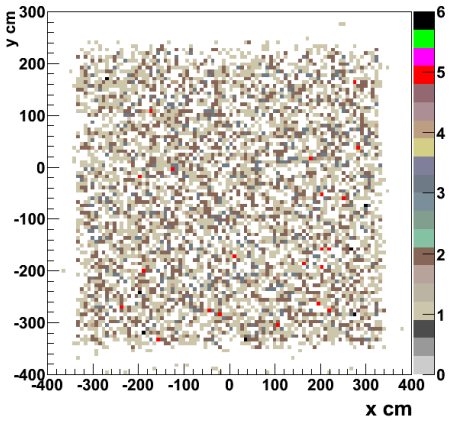

Figure 4.8: The x-$y$position of the starting point for the muon track in CC contained events.

near the vertex), it is plotted in Fig. 4.8; there isn't any bias in the data, as expected by the MC simulation.

The reconstructed momentum is plotted in Fig. 4.9 for all the longest contained tracks in the event, identified as a muon. Due to the mentioned uncertainty in the expected number of interactions, and to the uncertainty of the value of the magnetic field (that affects the momentum with an uncertainty of 3% [85]), the error on the number of events expected per bin in the spectrum of the momentum is set to ±10%. The number of MC events is still normalized to the events expected for the collected p.o.t in the respective plot.

The spectrum includes the contamination from NC events with a long hadronic track that is reconstructed and misidentified as muon; from the MC analysis this contamination is expected to be in the lower momentum range ($p < 6$ GeV/c). The events with positive charge sign are due to the contamination from $\overline{\nu}_\mu$ interactions. The agreement between data and MC expectation is quite good. Also for the number of events with high reconstructed momentum (> 60 GeV/c, not included in the plot),

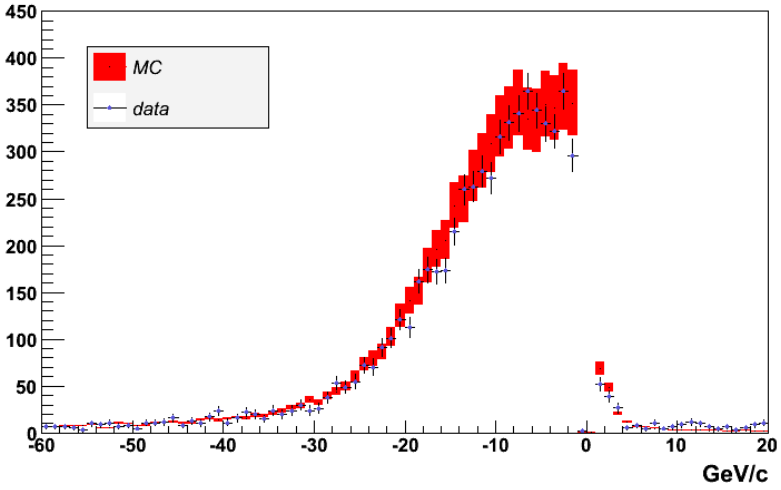

Figure 4.9: Spectrum of the momentum × the charge sign for the tracks identified as muon in the CC contained events. Red boxes are the MC expectation, points the data, the errors of the MC is set to the ±10%.

there is a good agreement with the MC expectation; infact, the events with a negative muon reconstructed and a momentum bigger than 60 GeV/c are 3.5% of the total, with a MC expectation of 3.5%.

The data-MC comparison is also shown in the Fig. 4.10, where the ratio between the momentum spectrum of the data and the one of the MC expectation is reported. This ratio will be used in the next section to estimate the number of expected τ events.

In Fig 4.11(a) and 4.11(b) the slope distributions of the tracks identified as muon in the *(xz)* and *(yz)* planes are plotted. The agreement between data and MC expectation is quite good, the MC normalization is done on the expected number of events for the respective collected p.o.t. The percentage of events with slopes bigger than 60 mrad is for both projections smaller than 0.5%, with a MC expectation of 0.2%. The mean value of the angle will be analysed in the next section, for each year of data taking separately.

As already mentioned, the length of the track and the density of the material crossed by the track are the important parameters to identify the muon. To evaluate these parameters, the length of the three-dimensional track and the density of the material crossed by the track are taken into account by the Kalman filter to estimate the energy loss (and Multiple scattering). In Fig. 4.12 the integrated density of the material crossed, multiplied by the step length is plotted; the data and the MC expectation are in good agreement; the same can be observed in Fig. 4.13, where the total track length is reported.

The first peak in Figs. 4.12 and 4.13 contains the tracks (muons) stopping in the same target module as they started and the exiting muon with vertex in the SM2, the second bump contains the tracks starting in the target of SM1 and stopping in SM2, and the tracks exting the detector with vertex in the SM1; only few tracks stop in the

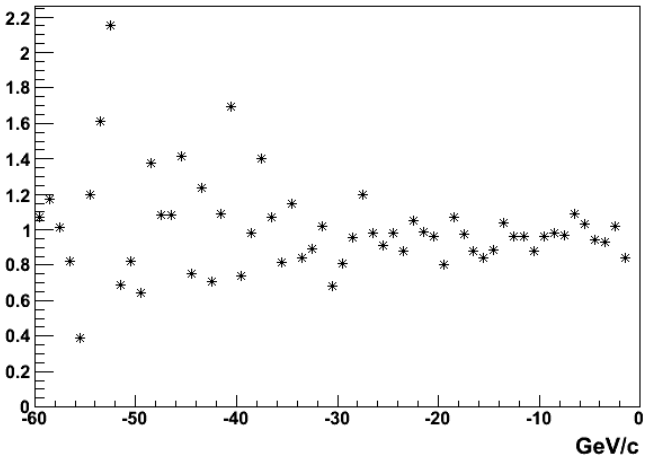

Figure 4.10: Ratio between data and MC expectation of the momentum spectrum reported in Fig. 4.9.

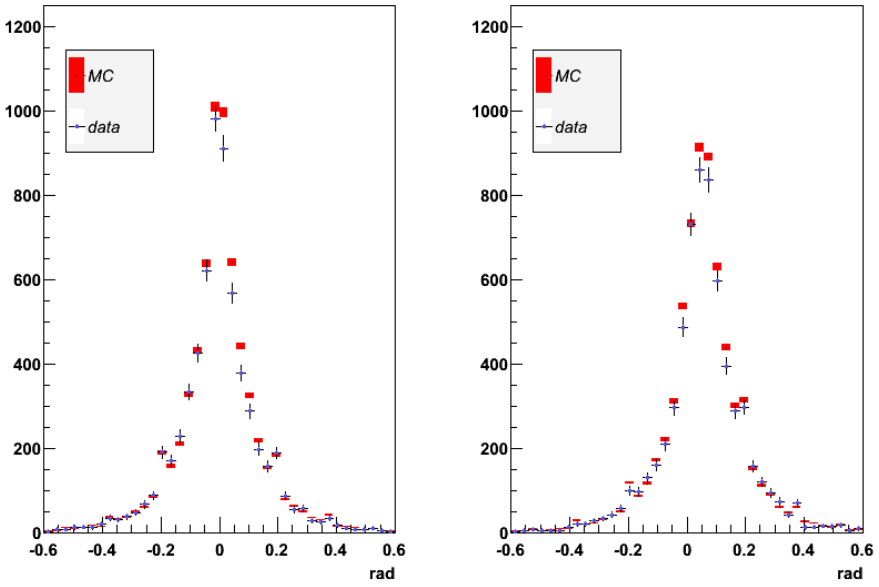

Figure 4.11: Distribution of the slopes in the *(xz)* plane left and *(yz)* plane right, of the tracks identified as contained muon. Red boxes are the MC expectation, points the data; the errors are statistical only.

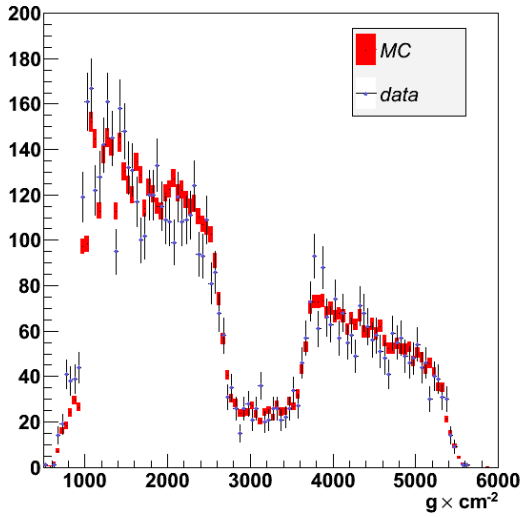

Figure 4.12: Integrated track lenght weighted with the crossed material for the tracks identified as contained muon; red boxes are the MC expectation, points the data; the errors are statistical only.

spectrometer between SM1 and SM2.

4.2.1 Analysis for each data taking year

The data of contained CC events have been analyzed for each year separately to verify that the reconstruction capability is stable.

In Fig. 4.14 the momentum spectra are reported separately for the three years of data taking. As can be seen, the three spectra are all in good agreement with the MC expectations (all the spectra, MC expectation included, are normalized to one). Also for the different data taking periods the percentage of events with a muon track with negative charge and momentum bigger than 60 Gev/c have been calculated: for the 2008, 2009 and 2010 data taking respectively, the percentage of negative muons reconstructed is 95.2%, 94.8%, 95.5%, with a MC expectation of 96%. The percentage of negative muons with a momentum bigger than 60 GeV/c are for the three years: 3.5%, 3.6% 3.5% with an expectation of 3.5%.

In Fig. 4.15(a) and 4.15(b) the mean value of the angle of the muon tracks in the two coordinate views is plotted, the error is given by the RMS of the slopes. The angle is reported in degrees, and, as expected, it is compatible with the null value for the *(xz)* plane, and in the *(yz)* plane it is compatible with the slope of the neutrino CNGS beam of 3.2°.

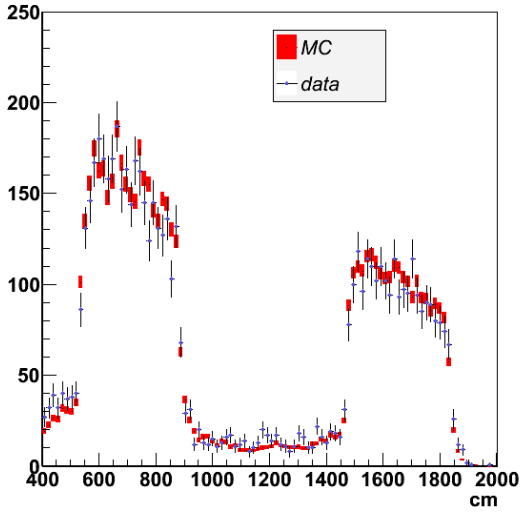

Figure 4.13: Total length of the tracks identified as contained muon; red boxes are the MC expectation, points the data; the errors are statistical only.

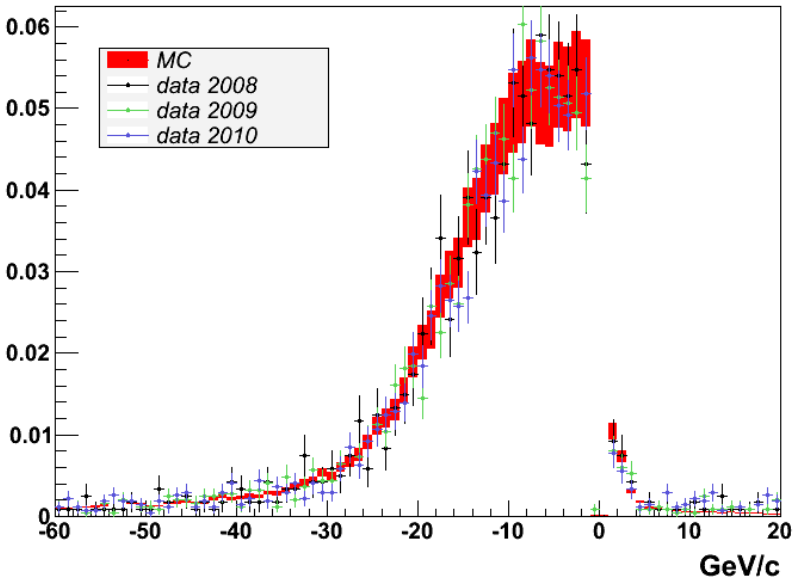

Figure 4.14: Muon momentum spectra for the muon tracks identified as the CC contained events, for the three years of data taking. Red boxes are the MC expectation, points the data in the different years of data taking, as reported in the legend; the errors of the MC expectation set to $\pm 10\%$. The sum of entries in all spectra is normalized to 1.

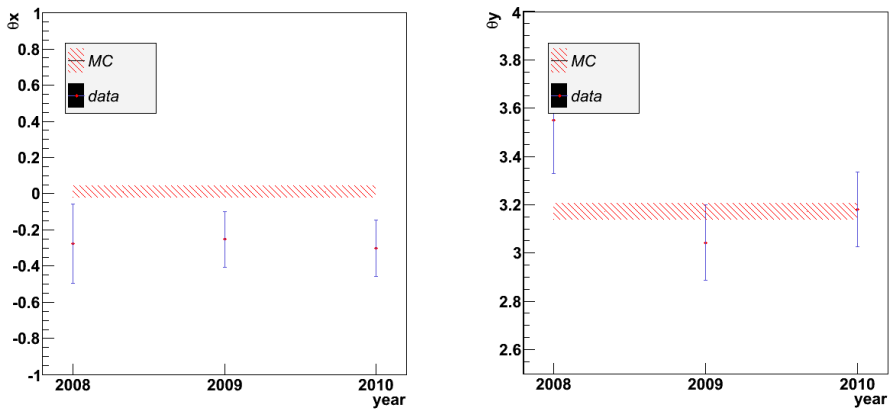

(a) (b)

Figure 4.15: Mean value of the angle of the contained muon tracks in the xz plane in left and yz right.

4.3 The τ detection in OPERA

The main physics goal of the OPERA experiment is the direct observation of ν_τ appearance from ν_μ oscillation. As already mentioned, this is possible identifying the decay topology of the τ particle produced in the charged current interaction. About 85% of the τ decays have only a single charged daughter particle, μ^-, e^-, h^-, see eq. 2.1, leading to a specific decay topology, that is used to distinguish it from the ν_μ interactions. As sketched in Fig 4.16 a clear kink exists between the daughter particle and the τ lepton, and also a larger missing transverse momentum due to the involved ν_τ. Fig 4.16 shows a schematic of the two different categories of τ decays, called long and short decay:

- *long-decay* Top-sketch of Fig. 4.16. The τ decay occurs in the first or second lead plate downstream the one containg the vertex. In this case it is possible to see the clear kink angle between the τ and the daughter track.

- *short-decay* Bottom-sketch of Fig. 4.16. The τ decay is in the same lead plate where the neutrino interaction occurred. The τ candidates are selected on the basis of the impact parameter (IP) of the τ daughter track with respect to the interaction vertex.

Taking into account the geometrical features of the OPERA ECC, and considering as short decays also the events in which the τ decays in the first plastic base after the vertex, the expected ratio of these two categories is: 29.6% long events and 70.4% short ones [67].

The expected number of ν_τ interactions in the detector for $22.5 \times 10^{19} p.o.t.$ (corresponding to 5 years at nominal beam intensity), assuming $\Delta m^2 = 2.5 \times 10^{-3} eV^2$ and full mixing, is ~ 115 $\nu_\tau CC$ events. The detection efficiency, the events expected and

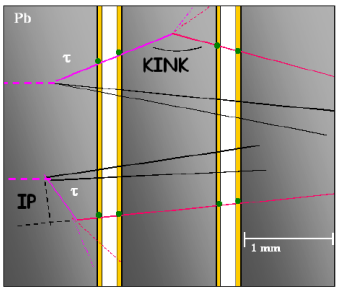

Figure 4.16: Schematic picture of the τ detection technique in the ECC cell for long (top) and short (bottom) decays.

the expected background was already presented in sections 4.3.2 and will be further discussed in the following sections.

4.3.1 Applied cuts fot the τ selection

Several cuts are applied to the different decay topologies to select the τ events. Here is a short summary on the main selection criteria, a full description can be found in [53]. For all the decay channels the kink is required to occur within 2 lead plates downstream of the primary vertex, and the kink angle has to be larger than 20 mrad. The other cuts are channel dependent:

$\tau \to e$ The daughter momentum is required to be $1\ GeV < E_e < 15\ GeV$; the lower cut is applied to reduce the background from low energy electrons, the upper limit to reduce the background from prompt electrons from $\nu_e CC$ interactions. Next, the transverse momentum at the decay vertex is required to be $> 0.1\ GeV/c$ to reject the $\nu_e CC$ interactions.

$\tau \to \mu$ In this decay channel the μ is required to have an energy $1\ GeV < E_\mu < 15\ GeV$. The lower cut rejects possible low energy hadron background and rejects events for which the μ identification is poor, the upper cut reduces the background from scattering of a prompt muon from $\nu_\mu CC$ events. Moreover, a cut on p_t at the decay vertex of $p_t > 0.25\ GeV/c$ is applied. A full recalculation of the efficiency for this channel is presented in [67], including the efficiency of the electronic detector reconstruction (due to trigger, the geometry selection, the event selection, the brick finding), the efficiency of the scanning (CS and vertex finding efficiency), the kinematic cuts applied and the branching ratio of the process.

$\tau \to h$ Severe kinematical cuts at the decay and the primary vertex are applied to suppress the background:

- daughter momentum higher than 2 GeV/c;

- decay P_t higher than 600 $MeV/c, 300$ MeV/c if there is a gamma found pointing to the decay vertex to reject hadron interactions;
- missing P_t at primary vertex lower than 1 GeV/c to reject NC events with larger missing p_t (neutrino);
- azimuth angle ϕ between the resulting hadron momentum direction and the parent track direction (in the transverse plane) larger than $\pi/2$ rad.

4.3.2 Background

The main background sources will be discussed in this section, they are studied with a full simulation of the physics processes, the beam and the detector; most of them are still under study to have a comparison of the expectation with the measurements, and to use the data to obtain constraints on the background.

The main sources are:

- *Prompt ν_τ production in the primary proton target and in the beam dump* The CNGS beam is obtained from the protons hitting a carbon target, hence also the generation of D_s is possible. These particles can decay into a ν_τ, leading to a small intrinsic contamination of the beam. Taking into account the features of the CNGS and the baseline of the experiment, this contamination [70] is expected to be negligible, of the order of $O(10^{-6})$ $\nu_\tau CC$ interaction per $\nu_\mu CC$ interaction.
- *One-prong decay of charmed particles.* Charm particles have a lifetime and a mass similar to the τ particle, see Tab. 4.2, thus, they can mimic the decay of the τ, in the case that the reconstruction of the event fails to identify the primary muon, and the secondary muon is attached to the primary vertex with negative charge. Charmed particles are produced in CC and NC neutrino interactions through the reactions:

$$\begin{aligned} &\nu_\mu + N \to c + \mu^- + X \\ &\nu_\mu + N \to c\bar{c} + \mu^- + X \\ &\nu_\mu + N \to c\bar{c} + \nu_\mu + X \end{aligned} \tag{4.1}$$

From the CHORUS experiment [71] the following relative rates and thresholds are obtained (extrapolated to OPERA energy):

$$\begin{aligned} &\frac{\sigma(\nu_\mu + N \to c + \mu^- + X)}{\sigma(\nu_\mu N) \to \mu^- X} = (4.38 \pm 0.36)\% \\ &\frac{\sigma(\nu_\mu + N \to c\bar{c} + \mu^- + X)}{\sigma(\nu_\mu N) \to \mu X)} < 0.1\% \\ &\frac{\sigma(\nu_\mu + N \to c\bar{c} + \mu^- + X)}{\sigma(\nu_\mu N) \to \nu_\mu X)} \equiv \frac{N_{c\bar{c}}}{N_{NC}} = 0.36\% \end{aligned} \tag{4.2}$$

	Mass (GeV)	$c\tau(\mu m)$
τ	1.78	87.11
D^0	1.86	122.9
D^+	1.87	311.8
D_S^+	1.97	149.9
Λ_C^+	2.29	59.9

Table 4.2: Mass and lifetime of the charm particles produced in OPERA compared to the τ particle.

As discussed in [67], the background coming from the second and third reaction is negligible.

The estimation of the background due to charm events in the different τ decay channels is reported in Tab. 4.3 where the electron and hadronic channel have been calculated with the strategy and efficiency of the proposal [53], including the latest results of CHORUS and NOMAD. The μ decay channel has been recalculated including the new efficiency evaluation in [67]. All the estimations have been made for five years of data taking at nominal beam intensity.

- *Background from π^0 and prompt electrons.* This background affects the electron channel. Scattering of primary electrons from the $\nu_e CC$ interactions can mimic the τ decay in this channel. On the other hand, the electrons produced in the π^0 conversion from a ν_μ interaction could mimic a τ decay in this channel, if a π^- undergoes a charge exchange process. The estimation of these background sources, done with a full Monte Carlo simulation, are less than $1 \times 10^{-6} \times N_{CC}$ events for the prompt electrons and about $0.1 \times 10^{-6} N_{CC}$ events from the π^0 [53].

- *Large angle muon scattering.* Muons in the $\nu_\mu CC$ events can fake a muonic τ decay in the case of a scattering with large angle. In [67] this expectation has been evaluated, taking into account for the muon a rate of large angle scattering of $1 \times 10^{-5} \times N_{CC}$ for 2 mm of lead and a muon $p_t > 250\ MeV$. This is a conservative limit considering the result of CHORUS, confirmed by more recent measurements made at CERN. The expected background is 0.07 events in the muonic channel for five years of nominal beam.

- *Hadronic reinteractions.* A source of background to the $\tau \to h$ channel is due to re-interactions of hadrons in lead from $\nu_\mu NC$ and $\nu_\mu CC$ events where the primary muon is not identified. Hadronic reinteractions can also be an important source of background for the channel $\tau \to \mu$, if the primary muon is not identified and the hadron is misidentified as a muon. The contribution to the hadronic channel has been studied with MC simulations, and confirmed by experimental cross checks. The MC studies, made using FLUKA, analyzed about 160 million events, including $0.15 - 15\ GeV \pi^+, \pi^-, K^+, K^-$ impinging on 1 mm of lead. The probability for a background interaction occurring over 2 mm of lead, satisfying

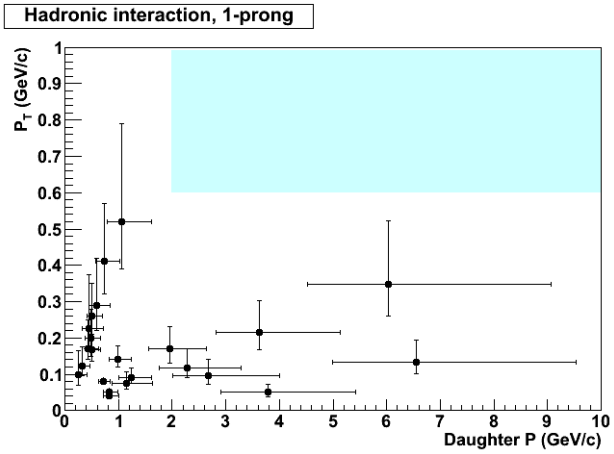

Figure 4.17: Momentum versus the transverse momentum of the daughter for 1-prong kink interactions for OPERA data. The data were collected by performing Scan Forth on hadrons after finding the ν_μ interaction vertex. The blue area is the OPERA signal region.

the selection criteria for the reconstruction of the kink topologies, is $(1.9 \pm 0.2) \times 10^{-4}$ per NC event [72].

As experimental cross check a total of 11 m of hadronic path length in Scan Forth mode, after the location of the interaction vertex, were scanned, collecting 21 hadronic 1-prong re-interactions. Figure 4.17 shows the plot of the daughter momentum versus the transverse momentum of the daughter, for these events, none of them lies in the OPERA signal region (indicated in blue). An upper limit on the expected background of 3.3×10^{-4}kinks/NC event (95% C.L.) was calculated [73], consistent with the result obtained from a brick exposure to a pion beam.

If the scattered hadron is misidentified as a muon, a contribution to the background in the muon decay channel results. In [67] this was estimated, after a MC simulation, considering the probability for a charged hadron to re-interact, the probability to misidentify a muon, and the efficiency of location of the brick. The expected background is 0.374 events in the muonic channel for five years of nominal beam.

The total background expected in five years of nominal beam for the different sources is summarized in Tab. 4.3. The muon channel was fully recalculated in [67], and the background estimation for the electronic and hadronic decay channel comes from [53]. The estimation of hadronic reinteraction background in the hadronic decay channel was recalculated in 2010 for the paper about the first τ candidate [72] and corresponds to a data sample of only 1088 events (CC+NC), fully analyzed at this time; this number is also given in Tab. 4.3 and is marked with a $*$.

	$\tau \to e$	$\tau \to \mu$	$\tau \to h$	$\tau \to 3h$
charm background	0.17	0.025	0.14	0.17
large angle muon scattering		0.07		
hadronic reinteraction		0.374	0.011$*$	

Table 4.3: Expected background events for five years of nominal beam. Result of the electronic and hadronic channel were given in [53] and the muonic channel in [67]. The background due to hadronic reinteraction, given in [72], for a sample of 1088 events (CC+NC), is marked with a $*$ (see text).

4.4 Number of expected τ decays

The analysis of the ν_μCC interactions can be used to monitor the beam, as we have seen in the last section: the number of events expected in the target is compatible with the collected events. Consequently, also the number od expected ν_τ CC events can be estimated the same way. The estimation of the expected events has been reported in the OPERA proposal [53] in 2000, and was fully recalculated in [67], considering the efficiency of brick identification and track reconstruction in the first two years of run. Including this new analysis the $efficiency \times branching\ ratio$ to reconstruct a $\tau \to \mu$ decay slightly decreases from 2.85% to 2.67%. The expected number of μ from τ decays, for the *p.o.t.* collected in the years analyzed is 1.13 applying this new efficiency.

A further correction to the expected number of $\tau \to \mu$ decays is coming from the new muon reconctruction efficiency for contained muons from ν_μ CC events, as described in the last section. The μ-momentum spectrum from τ-decay has been simulated starting with 5000 ν_τ CC interactions, this spectrum is shown in Fig. 4.18(a). In the prvoius section the μ-momentum spectrum from ν_μ CC events was presented and compared to the MC expectation, and also the MC/data ratio was calculated for each bin and shown in Fig. 4.10. This correction factor is now applied, bin per bin, to the muon spectrum from τ-decays (Fig. 4.18(a)); the resulting spectrum is shown in Fig. 4.18(b). Including then the cut: $1\ GeV < p_\mu < 15\ GeV$ required in this decay channel, the number of τ events expected is 0.91.

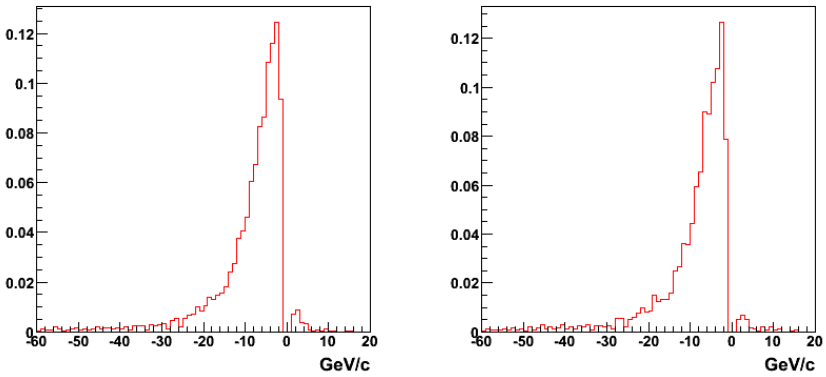

(a) (b)

Figure 4.18: MC spectrum of the μ momentum $\times$ charge sign due to the τ decays obtained from the simulation of 5000 ν_τ events, normalized to the expected number of μ due to τ decay on the left. MC spectrum of the μ due to the τ decay obtained from the simulation of 5000 ν_τ events, normalized to the expected events and corrected with the muon reconstruction efficiency obtained in the previuos section on the right.

Conclusions

The OPERA experiment is looking for the direct appearance of ν_τ in a pure ν_μ beam, via the detection of the τ lepton produced in the ν_τ CC interactions. The neutrino beam is produced at CERN SPS, 730 km far from the detector, located at the Gran Sasso National Underground Laboratory. The experiment started to take data, with the emulsion/lead target filled, in 2008 and is still running; it collected until now:

year	on-time events collected	CC events	internal events
2008	10141	7276	1709
2009	21455	15185	3559
2010	25492	17443	3201

After the complete analysis of a part of the events collected in 2008-2009, including 1088 events (CC+NC), OPERA found its first oscillation τ candidate. Collecting the events corresponding to the 22.5×10^{19} *p.o.t*, about 10 ν_τ CC events are expected to be detected until the end of the experiment, with a background at the level of one event.

The OPERA experiment, as described in Chapter 2, includes electronic detectors composed of scintillator planes, which interleave the target walls, and the magnetic spectrometers placed downstream of each target sector module, which are equipped with drift tubes and resistive plate chambers.

This thesis is focused on the reconstruction and the identification of the muon tracks produced in the ν_μ CC events. This is mainly important to identify the number of ν_μ interaction, and to prevent to misidentify them as ν_τ interactions, and it also permits to monitor the CNGS beam and the number of expected events. The reconstruction software includes a Kalman filter applied to the three-dimensional tracks to estimate the muon momentum and the position and the slope of the track in the region of the interaction vertex.

Part of my thesis work has been spent to implement a procedure to use the χ^2 of the Kalman filtering step to improve the track finding algorithm. The procedure developed permits to remove from the tracks the points with a bad χ^2 and select a better point, in case it exists.

In this thesis, MC analyses on samples of ν_μ CC (DIS and QE), $\overline{\nu}_\mu$ CC DIS, ν_μ NC, have been studied to investigate the software reconstruction capability. The ν_μ CC DIS events are expected to be 90% of the total CC events, the software for this sample of events obtains:

events with at least one 3-dim track reconstructed	96.6%
events with a $\mu-$ track reconstructed and identified	90.9%
events with a $\mu+$ track reconstructed and (mis)identifed	2.3%

For this sample, the Kalman procedure obtains a normalized momentum resolution of 18% for the muon tracks leaving the detector, and of 9% for the muons stopping in it. The resolutions obtained for the x and y-coordinate positions on the CS films, are 7.5 mm and 9.5 mm; but the position reconstruction is affected by an underestimation of the error.

This MC analysis points out that the ν_μQE events have a better reconstruction due to the smaller number of hits per event. Two different efficiencies (hit efficiency and track efficiency) have been defined to study the quality of the tracks reconstructed, those confirm that the ν_μ CC DIS events are not well reconstructed in case of short tracks (low energetic events), and the good reconstruction of the ν_μ CC QE events.

A data-MC comparison has been made considering the data collected in 2008, 2009 and 2010. The number of events for the three years of data taking are in agreement within 10%. All the parameters studied (muon momentum, slope of the track, number of tracks reconstructed per events) are in good agreement with the MC expectations, with the exception of the χ^2 of the track. For this χ^2 a significant disagreement has been found in its distribution, and as a consequance, this χ^2 was not used as a cut-parameter to select well reconstructed tracks.

The analysis of the ν_μCC interactions and the comparison with the MC expectation has then been used to estimate the expected ν_τ CC events. Considering the expected ν_τ events reported in the [67], and the correction derived from the ratio data-MC obtained for the ν_μCC events, the number of τ events (in the decay $\tau \to \mu$) has been estimated.

Part II

ArDM experiment

Chapter 5

The ArDM experiment

Astronomical observations about the structure and evolution of the Universe are well described by the Big Bang model, working in the framework of General Relativity; they support the hypothesis that the ordinary atomic matter represents only a small fraction of the total energy in the Universe.

The first observation, that supported this hypothesis, was published in 1933 by Fritz Zwicky, studying the Coma Cluster:

Present estimates of the masses of nebulae are based on the observations of the luminosities and internal rotations of nebulae. It is shown that both these methods are unreliable; that from the observed luminosities of extragalactic systems only lower limits for the values of their masses can be obtained, and that from internal rotations alone no determination of the masses of nebulae is possible [87]. In this paper he claimed that there must be more than two orders of magnitude more matter than could be accounted for by the observed luminous matter [88].

The experimental observations allowed to determine the basic features of our Universe. The Universe is spatially flat, the expansion is accelerating, and it is comprised of about one third Dark Matter (DM) and two thirds a new form of Dark Energy (DE) [89]. In this scenario the DE and a cold Dark Matter (CDM) components dominate.

To be compatible with the experimental observations the DM has to be neutral (no electromagnetic interaction), not-baryonic (zero baryonic number) and massive (to be cold); the WIMP (Weakly Interacting Massive Particle) represents a possible DM candidate.

The DM can be detected directly or indirectly; the direct detection is achieved by observing the elastic scattering of WIMP particles on target nuclei, while with the indirect method one tries to detect the products of the annihilation of the dark matter particles, in astronomical objects (galaxy).

The experimental limits on the WIMP cross section obtained by several experiments, are reported in Fig. 5.1; the extremely small cross section (spin-independent) expected for the WIMPs interaction (smaller than 10^{-44} cm^2 for masses of few of tens GeV), induces the number of expected events to be low. This requires the capability of measuring few expected recoil events in the energy range of 1 to 100 keV (cold DM), and at the same time a negligible background from other natural sources of radiation.

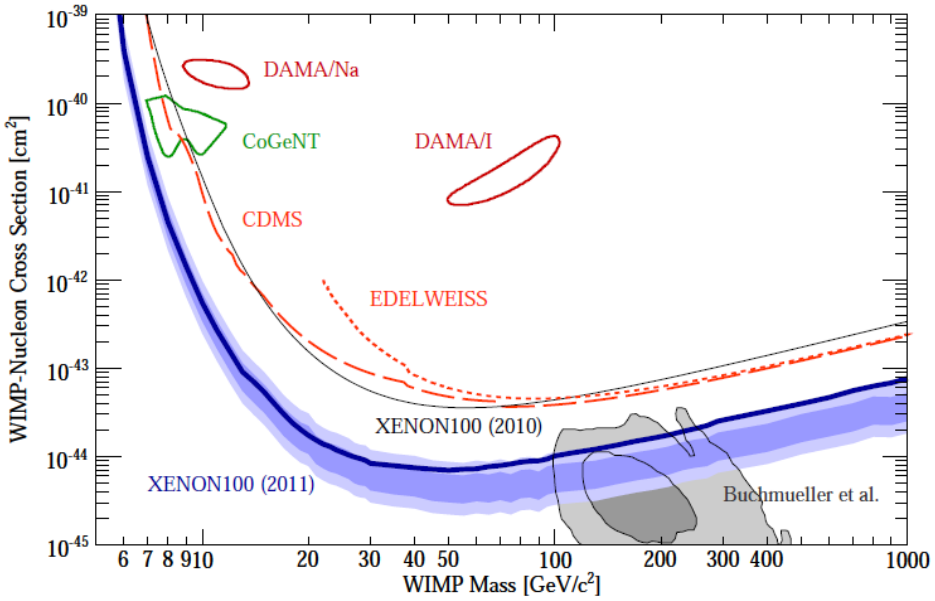

Figure 5.1: Spin-independent elastic WIMP-nucleon cross-section σ as function of WIMP mass. The XENON100 limit at 90% CL is shown as the thick (blue) line together with the 1σ and 2σ sensitivity of this run (shaded blue band). The limits from XENON100 (2010) [90] (thin, black), EDELWEISS [91] (dotted, orange), and CDMS [92] (dashed, orange, recalculated with $v_{esc} = 544\ km/s$, $v_0 = 220\ km/s$) are also shown. Expectations from CMSSM are indicated at 68% and 95% CL (shaded gray) [93], as well as the 90% CL areas favored by CoGeNT (green) [94] and DAMA (light red) [95]. The figure is reported from [96].

The main detectors searching for DM are based on three processes: the ionizing effect of a particle interaction, scintillation light from electronic excitation or a thermal signal from lattice vibrations. All these methods, alone or combined, allow to discriminate between the nuclear recoils (i.e. WIMP signal) and the electron recoil.

5.1 Liquid argon scintillation light

The liquid argon is used as target in many physics experiments since it has excellent scintillation properties and, given its relatively high electron mobility, is suitable for drifting electrons. Moreover, argon is easily available and this permits also the possibility to scale towards very large mass detectors. The properties of liquid argon are summarized in Tab. 5.1.

The passage of ionizing particles in liquid argon induces the formation of excited atoms (excitons) and electron-ion pairs; the scintillation light is produced both by the electron-ion recombination and by the radiative emission of the exciton. The scintillation light due to excitons is produced in the following process:

$$\begin{aligned} &Ar^* + Ar \rightarrow Ar_2^* \\ &Ar_2^* \rightarrow Ar + Ar + h\nu(UV) \end{aligned} \tag{5.1}$$

The scintillation light due to recombination, after the ionization process, is instead produced as follows:

$$\begin{aligned} &Ar^+ + Ar \rightarrow Ar_2^{**+} \\ &e^- + collisions \rightarrow e_{th}^- \\ &Ar_2^{**+} + e_{th}^- \rightarrow Ar^{**} + Ar \\ &Ar^{**} \rightarrow Ar^* + heat \\ &Ar^* + Ar \rightarrow Ar_2^* \\ &Ar_2^* \rightarrow Ar + Ar + h\nu(UV) \end{aligned} \tag{5.2}$$

Ar_2^+ represents the molecular ion and Ar_2^* the excited dimer; the step generating heat corresponds to a non-radiative transition, e_{th} is the thermalized electron. The wavelength spectrum of the scintillation light is in both cases peaked at 128 nm, due to the emission of a 9.8 eV UV photon.

The recombination process depends on the ionization density, and it is affected by the presence of an electric field. Applying an electric field, the free electron can be drifted and collected, and the ratio between charge and light produced can be measured. As discussed in [99], recombination of electrons and positive ions from the initial ionization decreases with increasing electric fields, particularly for heavily ionizing particles (α particles). Measurements in LAr have been reported by [100]. The recombination factors for relativistic particles with unit charge are fitted with a Birks law dependence as a function of the ratio of the particle stopping power $\frac{dE}{dx}$ to the applied drift electric field [101, 102]:

$$\frac{dQ}{dx} = A\frac{dE/dx}{1 + k_b\frac{dE}{dx}} \tag{5.3}$$

T at 1 atm (K)	87.2
$\rho(g/cm^3)$	1.396
λ_{att} 50 $keV\gamma$ (g/cm^2)	1.4
$\mu_{electron}(cm^2/Vs)$	500
W_{ion} (eV)	23.6
W_γ (eV)	25
λ_{scint} (nm)	128
τ_{fast} (ns)	7
τ_{slow} (μs)	1.6

Table 5.1: Main properties of LAr: temperature at 1 atm and corresponding density, attenuation length for 50 keV γ, electron mobility at the boiling point, average energies needed for the production of an electron-ion pair [97] or of one scintillation photon [98] (measured for 1 MeV electrons), LAr scintillation wavelength, lifetime of fast and slow scintillation components.

$\frac{dQ}{dx}$ is the charge of free electrons per path length produced by the ionizing particle, A and k_b are parameters to be obtained from the fit. A is the asymptotic value of the collected charge per unit length corresponding to a unitary specific energy loss. This expression is purely phenomenological and it is not valid in the high recombination region, that is in either low electric fields or high ionization density.

Hence, taking into account that the recombination depends on the electric field, the light collection is maxim at zero field.

Scintillation light emission is characterized by two decay times, associated to the radiative decay of the the singlet and the triplet state of the argon dimer to the lowest excited level. The slow and fast decay times differ significantly; the fast is approximately 7 ns, and the slow about 1.6 μs, as shown in Tab. 5.1. The clear difference between the decay times of the two components allows to separate the fraction of scintillation light due to the two different de-exitation states.

In case the charge produced in the ionization process is drifted and measured, both the ratio between charge and light and the ratio between the fast and slow component of the light collected depend on the type of interacting particle, and can be used as powerful discriminant of nuclear recoil signals against γ and electron backgrounds. A sketch of the expected distributions for electron-gamma recoils and nuclear recoils, is reported in Fig 5.2(a) for the ratio between fast and slow component (pulse shape discrimination) and in Fig5.2(b) for the ratio between charge and light. In [103] the results of the pulse shape discrimination in liquid argon is presented; as shown in Fig.5.3

The total scintillation light emitted due to the interaction of an ionizing particle in argon is generally quantified by the scintillation yield (Y_{scin}), defined as the mean number of photons per unit absorbed energy. The scintillation yield is observed to be dependent on the particle nature. The scintillation yield in this case can be estimated considering the mean energy needed to produce a UV photon in liquid argon. In

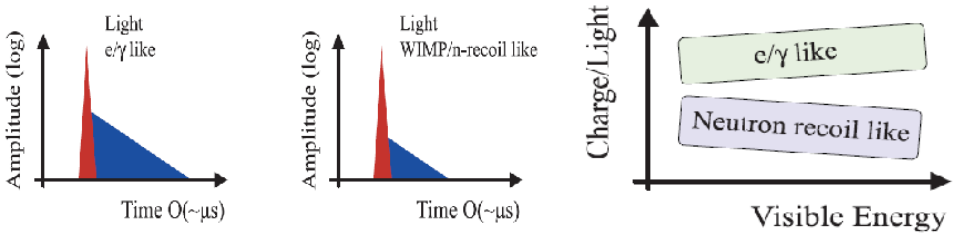

(a) (b)

Figure 5.2: Sketch of the possible discriminant between types particles in liquid argon. In 5.2(a) scintillation time structure for electron and nuclear recoils, in 5.2(b) the ratio between charge and light.

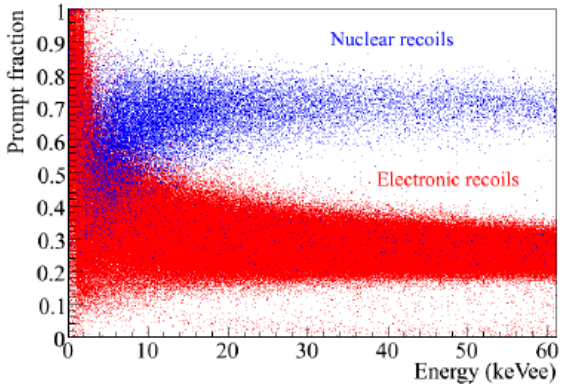

Figure 5.3: A scatter plot of the prompt fraction of the charge signal vs. electron equivalent energy deposition for tagged electron and nuclear recoils, reported in [103].

absence of an electric field the number of emitted photons is:

$$N_{ph} = N_i + N_{ex} = \left(n_i 1 + \frac{N_{ex}}{N_i}\right) = \frac{E}{W'_{l,\beta}}\left(1 + \frac{N_{ex}}{N_i}\right) = \frac{E}{W'_{l,ph}} \tag{5.4}$$

where N_i and N_{ex} represent, respectively, the number of excited atoms and the number of electron-ion pairs produced; $W'_{l,\beta}$ is the mean energy required to produce an electron-ion pair, $W'_{l,ph}$ is the intrinsic mean energy for photon production in liquid argon. From [104] $W'_{l,\beta}$ is estimated to be $23.6eV$ and the measured value of N_{ex}/N_i to be 0.21 [105], $W'_{l,ph}$ has been estimated to be 19.5 eV[106].

The scintillation light produced can be reduced due to electron escaping and quenching. The electron escaping process occurs since a fraction of electrons does not recombine for a long time (order of few ms), due to the small ionization density of the track. The quenching, mainly in the high linear energy transfer (LET) region, occurs when a large number of excitons are produced, so that the chance of two of them colliding is considerable, and they can undergo the reaction:

$$Ar^* + Ar^* \rightarrow Ar + Ar^+ + e \tag{5.5}$$

Hence, due to the ion and electron recombination only one photon is emitted instead of two.

The scintillation reduction is taken into account as an effective average energy loss for photon production $W_{l,ph}$, higher than the value considered so far, $W'_{l,ph}$. For relativistic electrons, from [106], the energy needed to produce a photon, $W_{l,ph}$, is estimated to be 25 eV.

5.2 The ArDM detector

The conceptual design of the ArDM experiment is illustrated in Fig. 5.4, the full description of the detector can be found in [110, 111]. A total mass of about 2 *tons* of highly purified liquid argon is contained in a vacuum insulated stainless steel dewar with following dimensions: 200 cm high and with an inner diameter of 100 cm. The inner detector is a double phase (liquid-vapor) TPC detector, with a fiducial mass of about 850 kg, including a light readout on the bottom of the system and a charge readout on the top of it, in the gas phase. After an event in the fiducial volume has produced scintillation light and free ionization electrons, the light can be collected by the Photo Multiplier Tubes (PMTs) placed at the bottom of the detector, and the electrons drift up from the interaction point following the electric field lines. The drift field is provided by a Cockcroft-Walton high-voltage circuit, designed to reach up to $3kV/cm$, for a total drift length of 120 cm

In Fig.5.5(a) and 5.5(b) the drawing and a photo of the actual detector are shown. In this picture the light readout system is shown, it includes a plane with 14 low background PMTs, suitable for cryogenic operation (8" Hamamatsu R5912-02MOD with bialkali photocathodes) To improve the light collection reflector foils cover the lateral sides of the detector.

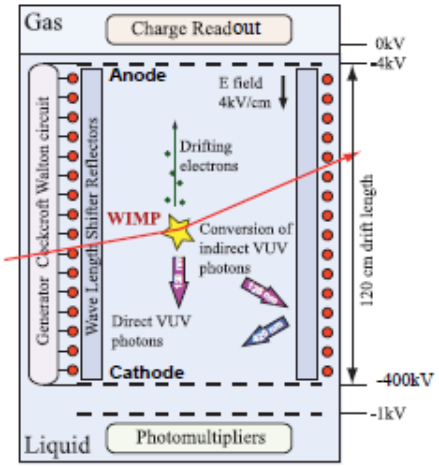

Figure 5.4: Conceptual layout of the ArDM experiment.

The charge readout system is placed in the gas argon phase. In order to overcome the surface tension of the LAr two extraction grids are needed to extract the electrons from the liquid and subsequently drift them to the charge readout system. The final configuration of the charge readout will contain a double stage LEM-TPC (Large Electron Multiplier TPC) in order to increase the signal to noise ratio, before the detection on a two dimensional anode [112]. The LEM-TPC is a novel kind of double-phase noble gas TPC in which the ionization electrons are drifted towards the liquid surface on top, are extracted into the gas phase by means of two extraction grids precisely positioned across the liquid. In the vapor phase, Townsend avalanche takes place in the electric field region confined in the LEM holes; then the charge is collected by segmented electrodes, on which the induced signals are recorded. The LEM has being developed on a smaller scale in a dedicated setup [118]. Until now a temporary charge readout, without multiplication, is installed in the ArDM detector.

The cryogenic system The detector is housed in a vacuum tight stainless steel dewar vessel. Before filling with LAr, the vessel is evacuated to a high vacuum, below 10^{-6} mbar, to minimize the contamination of the liquid from remaining impurities and out-gassing. To purify the liquid argon a custom-made purification cartridge, based on CuO powder, is used.

The detector vessel is surrounded by a jacket of LAr, called argon bath, that allows to cool down the detector. The surrounding LAr jacket is enclosed by an outer shell of stainless steel, which is actively pumped to keep an insulation vacuum better than 10^{-4} *mbar* for thermal insulation.

To continuously keep under control pressures and temperatures of the different parts of the system, a Programmable Logic Controller (PLC) system is used. The PLC controls all the vacuum and cryogenic processes: operation of the vacuum pumps, recirculation of the LAr in the detector vessel.

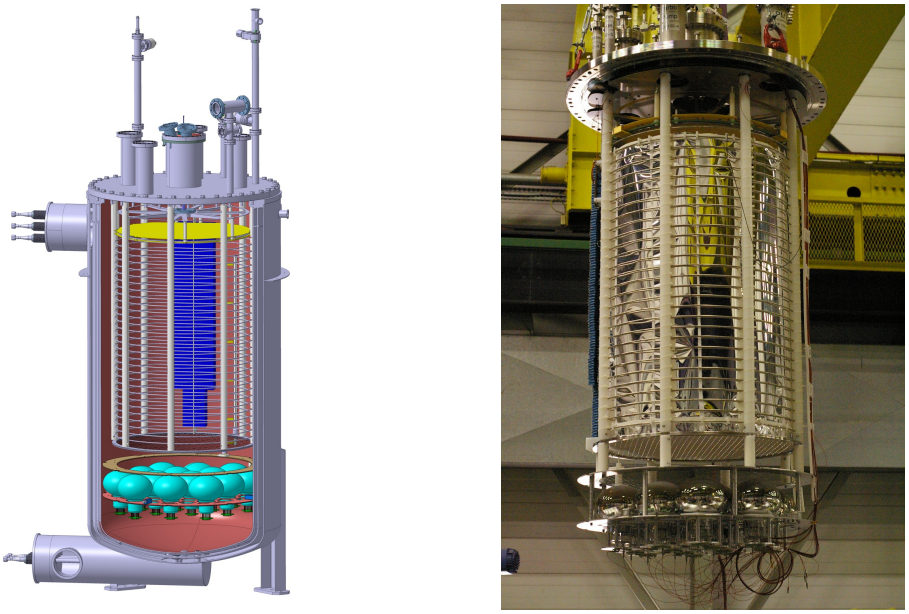

(a) (b)

Figure 5.5: Setup of the ArDM detector. In (a) a 3D drawing of the ArDM detector is shown; in (b) a picture of the main component of the detector.

The inner detector As already discussed, the inner detector consists of the PMT plane at the bottom, the reflector on the sides, the high voltage system, and the charge read-out on top.

The reflector and the PMTs have been coated with TPB (tetraphenylbutadiene) to shift the scintillation light from the VUV to the visible part of the spectrum (420 nm), the sensitive region of the PMTs. In ArDM the reflectors consist of Tetratex (TTX) foils, 254 μm thick, coated by evaporation with 1 mg/cm^2 of TPB, which has a fluorescence decay time of 1.68 ns and an emission spectrum between 400 and 480 nm. The shifted and reflected light is collected by PMTs, also coated by evaporation with a thin layer (0.05 mg/cm^2) of TPB for detection of direct scintillation light. To calibrate the PMT a light pulse from a 400 nm blue LED has been used, placed in the vapour region above the liquid argon surface. The PMT gains were set to 2.5×10^7 adjusting the voltages.

The development of high voltage systems is crucial for ArDM, which needs a stable and uniform drift field over the maximum drift length of 120 cm. The Cockcroft-Walton high voltage circuit [113] provides the electric field needed to drift the electrons, in a cylinder with radius about 40 cm, that confines the so called fiducial volume.

Very high purity argon ($[O_2]_{eq} < 1$ ppb, oxygen-equivalent impurity concentration less than a part per billion) is needed in order to drift free electrons over long distance (1.2 m) [117].

5.2.1 Background evaluation for the ArDM experiment

MC simulations to estimate the expected number of background events have been discussed in [113, 114]. In this section a short summary of the main background sources is presented.

- *Neutron background.* The single nuclear recoils induced by a neutron can not be distinguished from the WIMP induced nuclear recoil; hence, in this kind of experiment it is important to estimate the number of neutrons expected from the natural contamination with radioactive elements of the material composing the detector or the material surrounding it. The neutrons from radioactivity arise mainly from the decay chains of ^{238}U and ^{232}Th, having an energy in the range of few MeV.

  The detector consists mainly of metallic material (stainless steel) with a contamination U/Th typically of the order of few ppb, and minerals and glasses with higher contamination of the order of few hundred ppb. Hence, as reported in [114], the biggest contribution from the detector materials comes from the glass of the PMT and the vetronite of the LEM.

  The detector will be located at the Canfranc Underground laboratory [115], at a depth of 2540 $m.w.e.$ (meter water equivalent). The estimation of the expected neutron background from the radioactivity in the rock has been reported in [116]. To limit the number of events due to neutrons coming from the rocks a shielding surrounding the detector has been designed, composed of blocks of polyethylene with a thickness of 50 cm, such that any neutron has to cross at least 50 cm of polyethylene to enter in the fiducial volume.

  Neutrons can be induced also from the high energetic cosmic muons reaching the deep underground laboratory. Neutrons are produced by spallation or photonuclear processes, or by secondary interactions of the muon-induced hadronic showers. The shielding is less efficient for the muon-induced neutrons, due to the different expected energy spectrum of the induced neutrons, and since the fast muons can easily penetrate the shielding, the detector materials in this case can act as target for muons.

  The neutron background is reduced by a factor of about 2, distinguishing the multiple scattering events (MC simulations shows that half of the neutrons have more than one interaction in the detector) from the WIMP, that would never scatter more than once in the detector.

- *Electron recoils from ^{39}Ar.* ^{39}Ar is naturally present in atmospheric argon [107, 108] ($^{39}Ar/Ar = 8 \times 10^{-16}$), it is a β-emitter with a lifetime of 269 years and a Q-value of 565 keV. This induces a background with a rate of about 1 kHz/ton of liquid argon. The presence of ^{39}Ar requires a discrimination capability of about 10^8 to keep the background, due to mis-identification of electronic recoil events, to an acceptable value in DM search experiments. In fact, a fraction of about 4% of the ^{39}Ar$-\beta$ decay is in the region of interest for the DM experiment, corresponding to energy transferred to the nuclei of 30-100 keV. Replacing the

atmospheric argon (contaminated with ^{39}Ar) with argon extracted from underground wells, can reduce the rate of β-events more than one order of magnitude, in fact this argon is depleted from ^{39}Ar by more than one order of magnitude [109].

Gammas from U/Th of the detector components produce an interaction rate which is about three order of magnitude smaller than electron recoils from decays.

5.3 Analysis of the PMT signals

Tools to analyse the signals collected by the PMTs have been developed.

The data acquisition configuration is set to register all the PMT signals with a window of 1 μs before the trigger, as clearly visible in the traces in the Fig. 5.6(a) and 5.6(b). In the figure the signals of four PMT are reported, and it is visible the so defined fast component, the first 50ns of the signal, and the rest of the signal (defined slow component), in which the individual peaks are visible. The main steps of the reconstruction analysis, applied to all the PMT and to the virtual channel (the digital sum of all the 14 PMT signal) are:

- *Pedestal analysis*: the first μs of the signal (in this data taking configuration can not be correlated with the event that we are looking for) is studied to evaluate the pedestal of the signal. First of all, a rough evaluation of the mean and the sigma of the signal in this range is performed. Due to the fact that a single photo-electron (p.e.) signal can contaminate the pedestal region, a peak finding algorithm is applied here to find and remove the single p.e. signals.

  The single p.e. is identified looking for peaks 3σ above the mean value of the pedestal, and is removed masking 10 ns of signal before and after the peak. After removing it, the mean and the sigma of the pedestal is re-evaluated. The mean and sigma are used for the calculation of the threshold identifying the peak, hence they can be initially shifted by the presence of the p.e.; for this reason the procedure is iteratively applied (generally 2 iterations are sufficient). The pedestal is subtracted from the signal.

- *Peak finding:* The signal of the virtual channel is scanned in a fixed interval looking for the highest value; once the highest peak is determined, the software scans the signal from the time of this peak going backward until the signal is less than `[ 3*PedSigma]`, where PedSigma corresponds to the sigma of the pedestal previously calculated. This point is considered the beginning of the signal, t_0. The position in time of this main peak is called PeakTime.

- *Signal integration:* The maximum integration region allowed is 4.5 μs. The procedure starts applying the peak finding algorithm over the allowed integration region, hence the integration is limited on the region where a signal (peak) is found. The integration region around the peak is defined as the region where the signal is 4 times above the mean pedestal value. Two peaks are considered separated if their time distance is more than 40 ns.

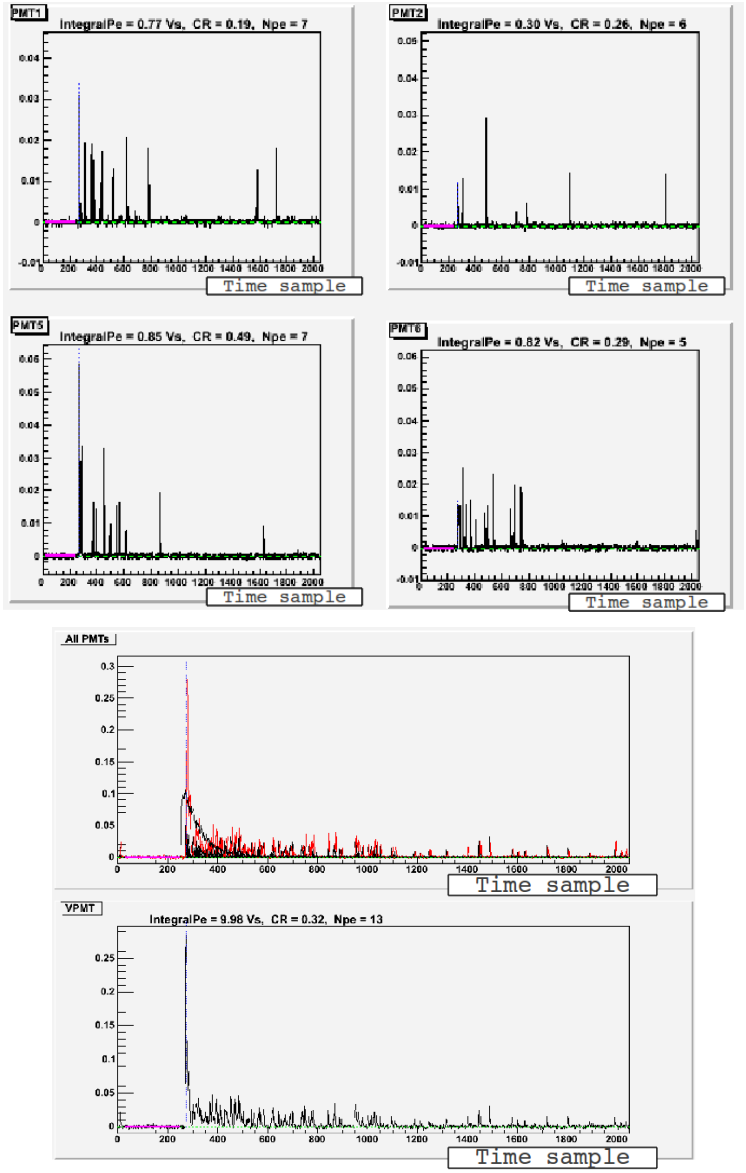

Figure 5.6: In (a) PMT signals for one event taken with the external ^{22}Na source, externally triggered. Four PMT signals are plotted. In (b) top: the signal of all the PMTs, the analog sum and the trigger signal are superimposed . In (b) bottom: the signal of the virtual PMT is reported. In all plots each channel correspond to a time sample of 4 ns.

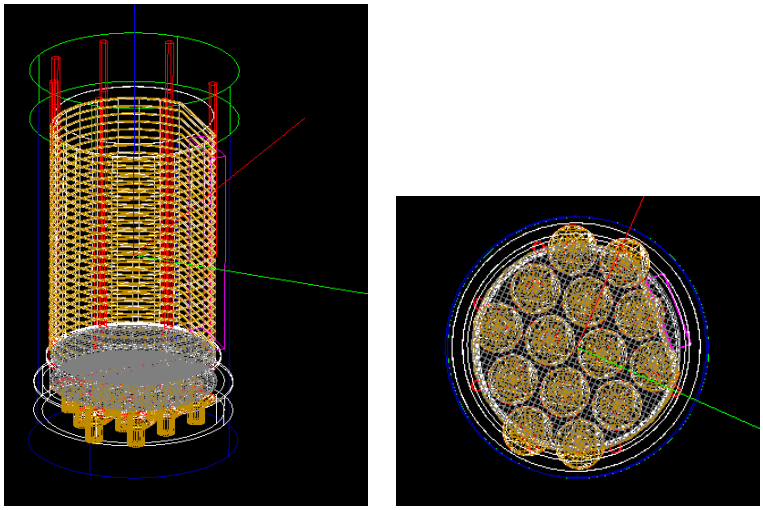

(a) (b)

Figure 5.7: Sketch of the ArDM geometry implemented in GEANT4, in (a) lateral view of the detector, and in (b) top view.

5.3.1 Monte Carlo simulations

A full Monte Carlo (MC) simulation of the ArDM detector has been developed [113], based on GEANT4 [119]. It includes a detailed description of the detector geometry and the tracking of the particle, including the full simulation of the light propagation. In Fig. 5.7(a) and 5.7(b) a sketch of the geometry of the internal detector implemented is shown in the two projections.

The physics processes involved and simulated to describe the gamma interaction in the detector are: Compton scattering, photoelectric absorption effect, pair production, and scintillation. The argon scintillation process is implemented producing a number of photons (with $\lambda = 128\ nm$) proportional to the energy deposited in the liquid argon. Taking into account the energy and the type of the recoiling particles (here we consider only electron recoils) , the mean number of scintillation photons produced can be calculated as:

$$\overline{N}_{\gamma scint}(E) = \frac{E}{W_{l,ph}} \tag{5.6}$$

where $W_{l,ph}$ is the mean energy required to produce a scintillation photon. Considering the quenching factor (for the electrons) due to the electrons escaping from recombination and without electric field, it is:

$$W_{l,ph} = 25\ \frac{eV}{\gamma} \quad \rightarrow \quad \overline{N}_{\gamma} = \frac{40\gamma}{keV} \tag{5.7}$$

The simulated scintillation photons are isotropically emitted.

To understand the detector response, the propagation of optical photons has been fully simulated including: VUV propagation, wavelength shifting, reflection and refraction on the internal detector surfaces, Rayleigh scattering. In the interaction with the

surfaces the optical photons can be: absorbed, re-emitted wavelength shifted, reflected or transmitted. All these processes have been described using the standard GEANT4 code.

The wavelength shifting process has been implemented taking into account the material property, and considering that the photons are always absorbed and re-emitted by the TPB; the visible photons are re-emitted isotropically.

The TPB has been evaporated on the reflector and on the PMTs, so in the simulation two different volumes have been built, covering the surface of the reflector and the PMT photocathode with the material property of the wavelength shifter material, to perform the process of wavelength shifting. A wavelength shifting efficiency has been added to include the possibility that the photon is absorbed and not re-emitted, and to simulate the effect of a non-perfect evaporation of the TPB on the surface, that decreases the number of photons re-emitted. Because this efficiency includes the effects of the surface geometry covered by the TPB, the evaporation process of the TPB and also the decreasing of the TPB efficiency with time, two different efficiencies were introduced for the reflector and the PMTs, since these surfaces have been evaporated with different procedures at different times.

The reflection and refraction processes have been implemented using the standard GEANT4 `OpticalBoundaryProcess`, implementing standard GEANT4 `OpticalSurface` for all the surfaces of all the materials in the liquid argon volume: the surface of the reflector, the surface of the PMT photocathode, and the surface between the liquid and gas argon phase.

The first surface is defined between the reflector and the wavelength shifter, it reflects, by definition, only visible photons; a reflectivity of 92% and diffuse reflection were assumed in the MC simulation for the reflector foils.

Similar, the optical surface of the PMT is defined between the TPB coating of the PMT and the PMT glass window covering the photocathode. The photons reaching the photocathode are absorbed.

The liquid argon surface has been implemented as a standard optical surface to describe the refraction process between two materials with different refraction indices (Snell law).

Once the photons have been absorbed by the PMT photocathode surface, the collection efficiency of the PMT is applied. The collection efficiency includes quantum efficiency (q.e.) measured by Hamamatsu for each PMT, and the parametrization of the efficiency as function of the point hit by the photon on the photocathode surface.

5.4 Data taking in 2010, event selection

The ArDM detector was filled for a first full test of the cryogenic system and the light readout in September/October 2010. During this test the high-voltage system has been tested reaching, in stable conditions, 60 kV.

The detector was first evacuated for about two months to reduce the out-gassing rate and the impurities; then it has been cooled (filling the external bath with liquid argon), and then filled with argon gas. The PMTs have been tested first in cold argon

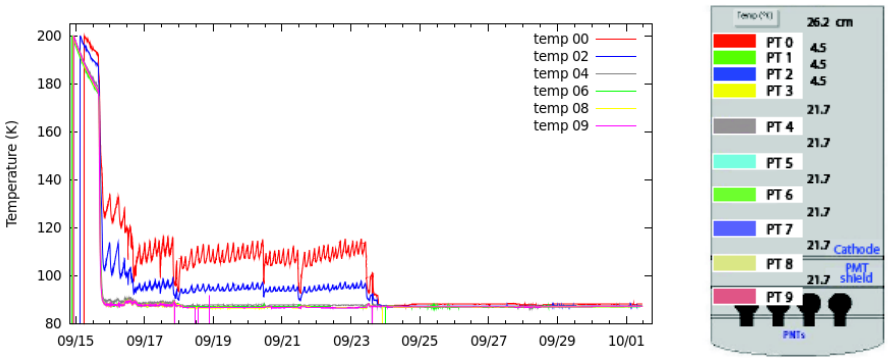

(a) (b)

Figure 5.8: In (a) the temperature in different positions, as shown in 5.8(b), during the 2010 data taking are shown. The temperatures stabilize at 87 K when the liquid argon reached the respective sensor in the detector.

gas. The detector was filled in two steps. In Fig. 5.8(a) the temperatures inside the dewar during the data taking are plotted.

During the test the ArDM light response was tested in many different configurations: data have been taken with the LED to calibrate the PMT response, with the external ^{22}Na source and different trigger configurations, with muons crossing the detector, part of these configurations with or without electric field.

In this chapter the analysis of the data taken with the external ^{22}Na source is presented.

The calibration of PMT gains has been obtained analysing the signal of a single photoelectron (p.e.) for each PMT. This has been done with two different approaches: dedicated runs collecting the light signal of the LED and analysis of the single p.e. peaks in the data collected with the external source.

The LED calibration data have been taken periodically during all the data taking period, to test the stability of the PMT gain; in these runs the LED ($\lambda = 390nm$) was pulsed with a waveform generator, and the data acquisition system was triggered synchronously with the same signal. To calibrate the detector also the data with the external source have been analysed outside the region of interest for gamma interaction, to look for the single photo-electron peaks.

In both cases the signal from single p.e. has been fitted with the sum of two Gaussians (to include the possibility that a peak involves 2 p.e.) as shown in Fig. 5.9; the mean value of the Gaussian corresponds to the mean PMT gain for single p.e.. In Fig. 5.10(a) the PMT calibration is plotted for the different runs for each PMT, including both approaches, the results with these calibrations are perfectly compatible, and the gain is quite stable during the data taking. In Fig. 5.10(b) the sigma of the Gaussian function fits of the single p.e. peaks is reported, it is observed to be quite stable (variations within 15%)for all PMTs. It represents the uncertainty in the gain value and will be used to smear the true expected value obtained from the MC simulation for the MC-data comparison.

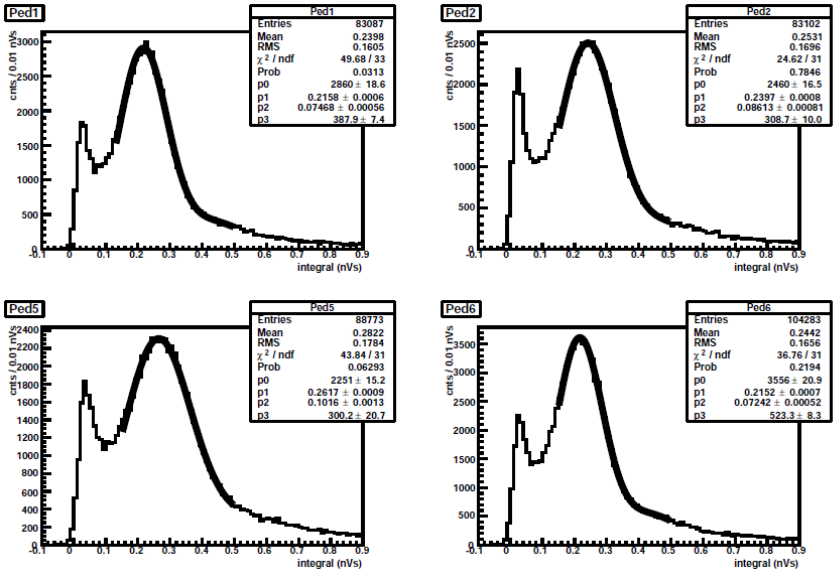

Figure 5.9: Integral of the the single p.e. signals from 4 PMTs, fitted with a Gaussian to find the gain calibration factor.

To calibrate the ArDM and test the light readout system a 20 kBq ^{22}Na source has been used; it emits at the same time two back-to-back 0.511 MeV annihilation γ-rays, in few *ps* and a third 1.275 MeV γ-ray from the de-excitation of the daughter ^{22}Ne* nucleus. The setup of the system for data taking with the external source is sketched in Fig. 5.11(a) and 5.11(b), the position of the source was moved along the height of the detector. The data acquisition configuration is set to be triggered externally, using the signal from the NaI crystal placed near the source as sketched. A threshold on the NaI crystal signal is required, at least one of the less energetic γ's has to be detected, this trigger configuration infers that the detector, for each event, can be crossed by: one 0.511 MeV γ, one 1.2 MeV γ, or two γ: one 0.511 MeV and one 1.2 MeV.

Once the PMT traces and the virtual PMT signal have been analysed, following selection criteria are applied to select the gamma events:

- *peak time:* In the analysis the software is forced to look for the main peak in the region of $250 - 350$ time samples (corresponding to the range 1 μs to 1.2 μs) . The distribution of the peak time for the different positions in which the source has been placed is shown in Fig. 5.12. The peaks in the four source positions are compatible with each other, due to the fact that one time sample is 4 ns, not short enough to see the different mean time propagation of the light in the events, from the different positions of the external source. In fact, the different z-position of the source induces a highest mean position of the gamma interaction, and of the scintillation light generation point in the liquid argon, as will be shown in the next section with a MC simulation.

  Applying only the peak time selection on each of the event samples, a fraction

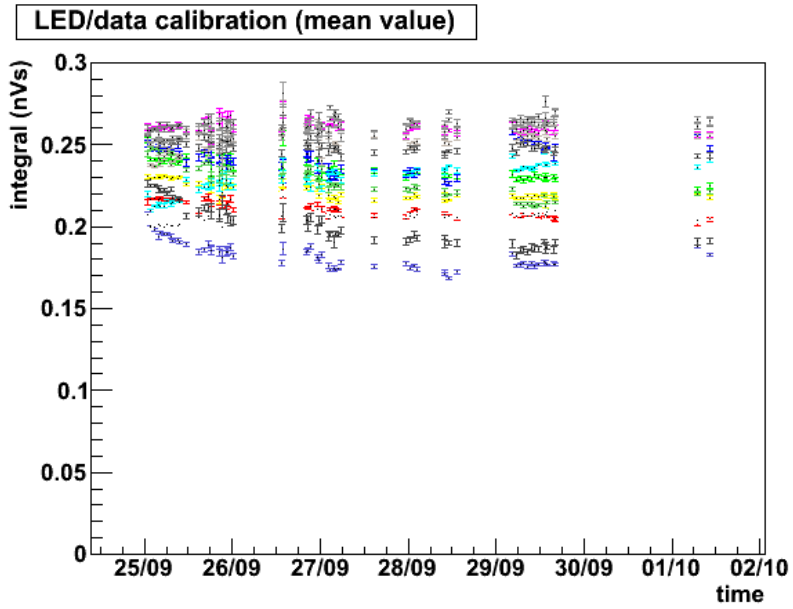

(a)

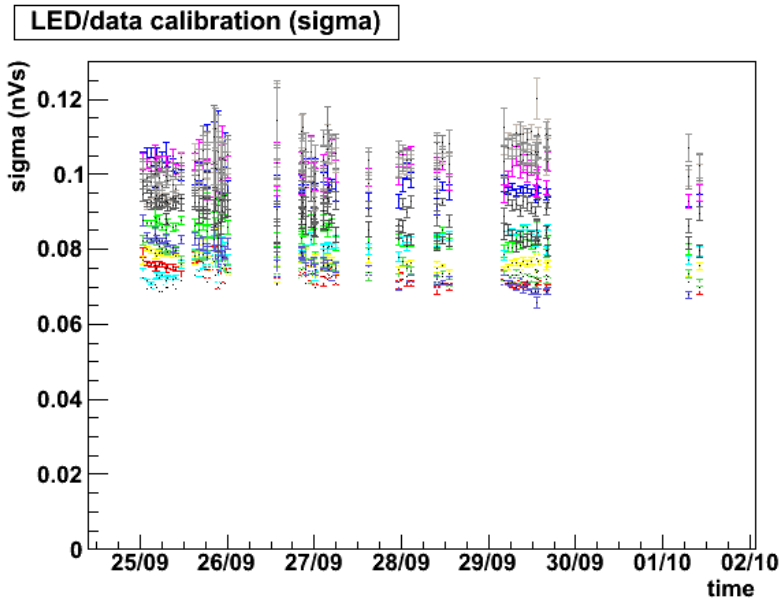

(b)

Figure 5.10: In (a): PMT calibration results obtained during the data taking with the dedicated LED runs, and with the analysis of the data taking with the external source; the mean of the Gaussian fit for the single p.e. peak is reported for all the PMTs. In (b): uncertainty of PMT gain, the sigma of the Gaussian fit for the single p.e. peak is reported for all the 14 PMTs.

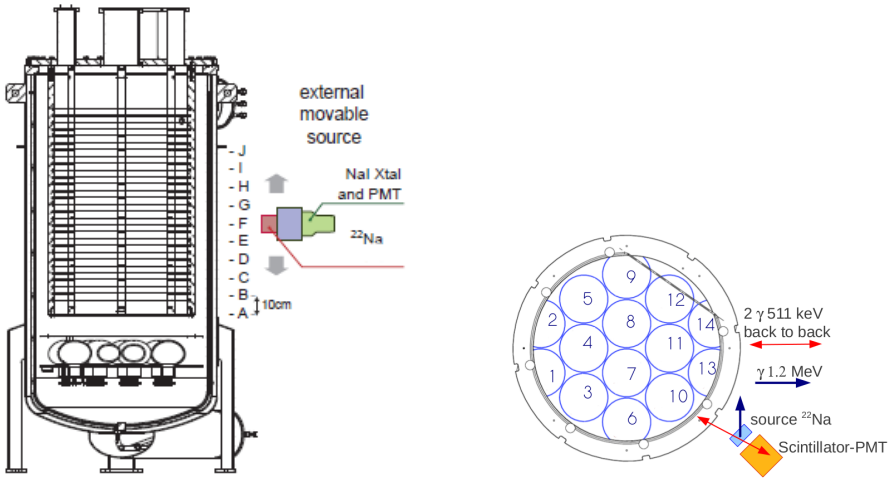

(a) (b)

Figure 5.11: Sketch of the ArDM detector and the source position; in (a) the different z-position of the source are shown, in (b) the view of the detector and the source setup is sketched in the xy-plane including a possible γ event.

of 52.8%, 51.1%, 50.8%, 50.0%, is discarded, respectively, in the four positions of the source.

- *Pedestal sigma:* the RMS distribution of the pedestal calculated for the virtual channel is shown in Fig. 5.13. A high pedestal signal can be found if there is an overlap of a signal, or a part of it, not correlated with the one due to the gamma triggered by the external NaI scintillator. For this reason a cut, event by event, on the maximum pedestal RMS value has been set to 0.005 nVs as shown in the Fig. 5.13. It is also possible to observe that, as expected, the pedestal RMS distribution is independent of the source position. Applying only this cut, a fraction of 12.5%, 12.8%, 12.6%, 12.1%, has been discarded, respectively, in the four source positions.

  The pedestal RMS of each PMT trace has also been checked, showing that the cut on the virtual channel is sufficient, and a more strict cut, requiring the pedestal sigma $< 0.005\ nVs$ for all the PMT traces in each event, has the same selection capability.

After the two cuts just described, the following parameters, event by event, have been taken into account to select the interesting events:

- the number of peaks in the allowed integration signal region,
- the number of time samples in which the signal is integrated (effective time integrated),
- the effective time integrated in the range of the signal used to calculated the pedestal (pedestal time integration),

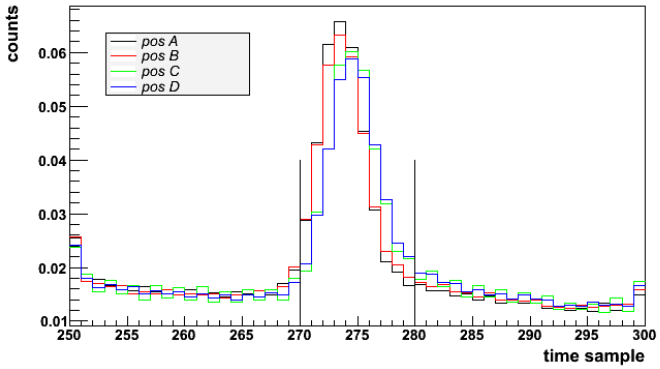

Figure 5.12: Peak Time distribution for the virtual PMT channel, for the four different source positions A,B,C,D (see Fig. 5.11(a)). The black lines correspond to the cuts applied to select the gamma events, the events with $275 < PeakTime < 280$ are selected. The time sample is 4 ns.

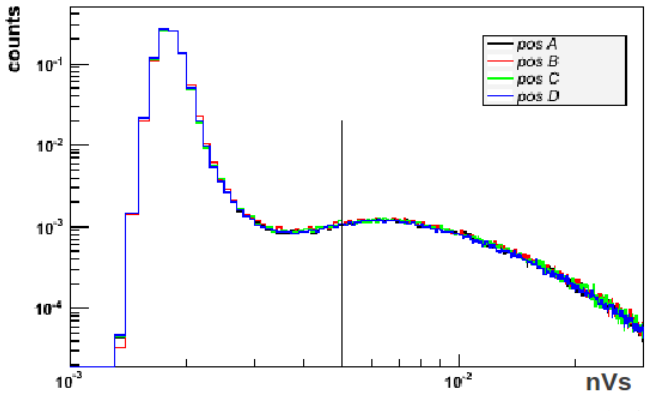

Figure 5.13: Normalized pedestal sigma distribution for the virtual PMT channel, for the four different source positions A, B, C, D. The black line corresponds to the cut applied to select the gamma events, the events below the cut are selected.

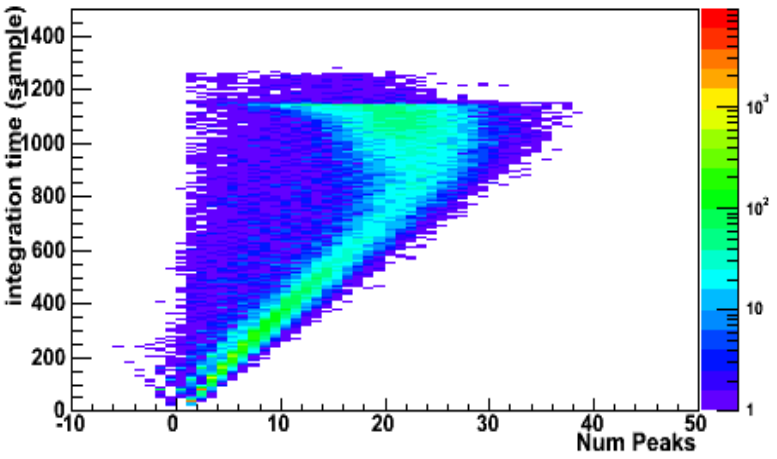

Figure 5.14: Distribution of the number of peaks found in the signal time range, and corresponding integration time in the event, for the virtual channel in the position D of the source.

- and the integral of the pedestal signal.

In Fig. 5.14 the effective integrated time is plotted with respect to the number of peaks found event by event. A negative number of peaks is obtained in the case that the main peak has a negative signal. This kind of event can not be related to the triggered event which we are interested. Therefore, the events with a number of peaks less than zero are discarded.

The effective integrated time and the integral of the signal are plotted in Fig. 5.15. As expected the integral increases with the integration time, and the maximum integrated time possible ($4.5\mu s$) is reached for the most energetic events. No cuts are applied on these parameters.

For these selected events the total signal integral of the event is defined as the sum of the integrals (obtained with the peak finding algorithm) of each PMT. This will be reported in p.e. using the conversion factor obtained with the gain calibration of each PMT.

As already discussed, the pulse shape analysis is one of the most powerful discriminants to select the particle type. In this case the goal is to separate the single gamma events from the pile-up, the events due to muons in random coincidence with the trigger and the background. The pile-up events are due to overlap of more than one source event in the same triggered window. The integrated signal of the fast component includes the integration from the starting point of the signal to the peak, plus the first 50 ns after the peak.

A further cut is then applied to the integral of the trigger signal to increase the threshold of the trigger configuration.

In Fig. 5.16 the fast/slow component ratio (CR) for the events (with the selections discussed: PeakTime, pedestal sigma, number of peaks and integral of the trigger

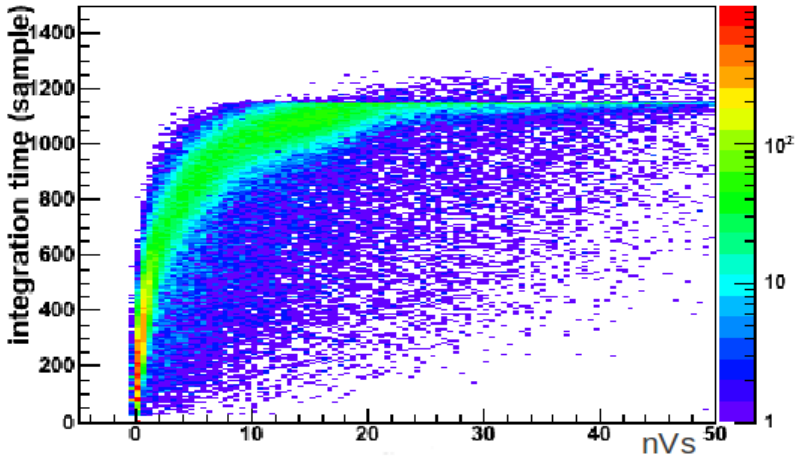

Figure 5.15: Distribution of the integral of the signal [nVs] and corresponding time of integration of the signal for the virtual channel in the position of the source D.

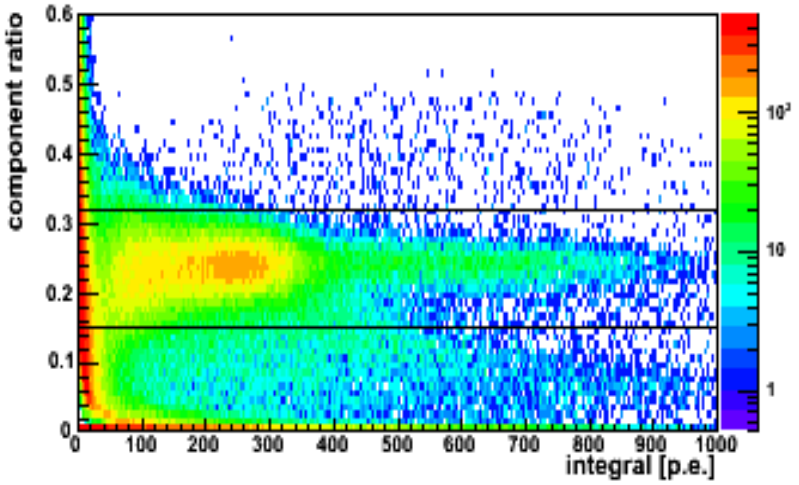

Figure 5.16: Fast/slow component ratio distribution and corresponding integral of the signal for the selected events described in the text, for the source position D.

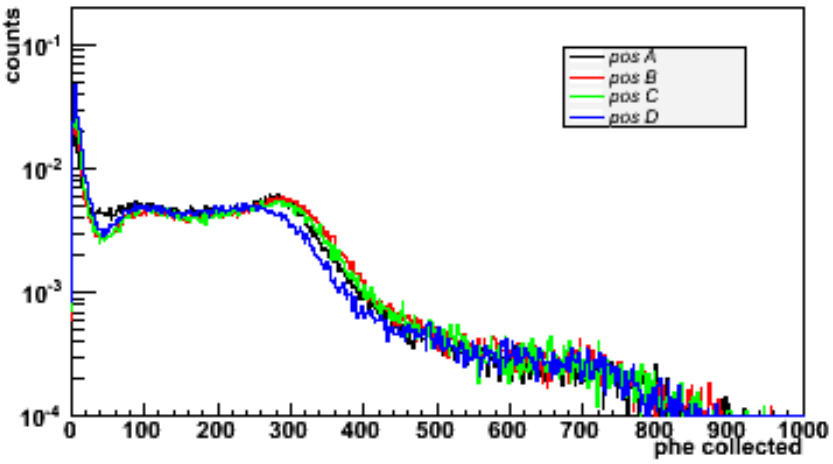

Figure 5.17: P.e. collected for the gamma-like selected events in the four different positions: A, B, C, D.

signal) is shown as a function of the total integral (p.e) of the signal. The cut defined to select the gamma events is: $0.15 < CR < 0.32$.

The number of events triggered for each sample and the fraction selected as gamma events are summarized in Tab. 5.2.

	events triggered	cut I (% ev.)	cut I+II (% ev.)	final selection (% ev.)
position A	892457	41.2%	32.5%	14.7%
position B	843998	40.9%	32.1%	14.0%
position C	598076	40.2%	32.7%	13.7%
position D	906998	40.1%	32.7%	13.1%

Table 5.2: Number of events collected in the four runs with the external source in the four different positions A, B, C, D. The cut I is the Peak Time selection, the cut II is the Pedestal sigma selection and the final selection is the sum of all the cuts described in the text. The final number of events represents the selected gamma events.

The collected p.e. spectrum for the selected events is shown in Fig 5.17 for the four different positions, the peaks around 300 p.e. correspond to the 0.511 MeV *gamma* energy. A light collection yield of 0.7 $p.e./keV$ has been obtained in the lower position.

5.4.1 Data-MC comparison

Many different types of events have been simulated to describe the expected detector results. In this section only the simulation of the external gamma source in the configuration of September-October 2010, and the data-MC comparison for the gamma events is presented. The gamma source configuration has been simulated generating two photons in each event, one with energy of 0.511 MeV the other one with energy

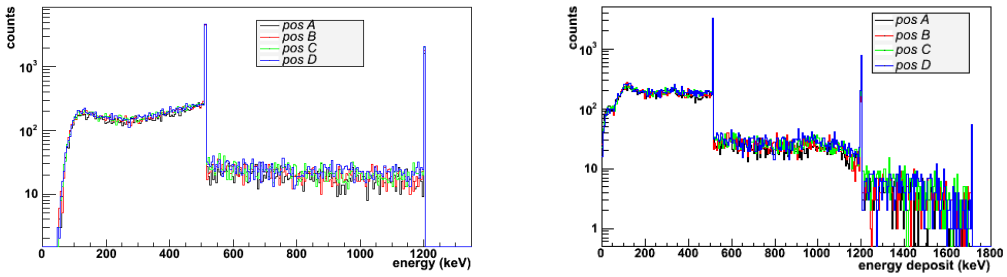

Figure 5.18: In (a) the energy of the first of the two gamma simulated entering the fiducial volume is plotted, in (b) the energy deposited by both gammas in the fiducial volume. The two sharp peaks correspond to the full energy of the original photon.

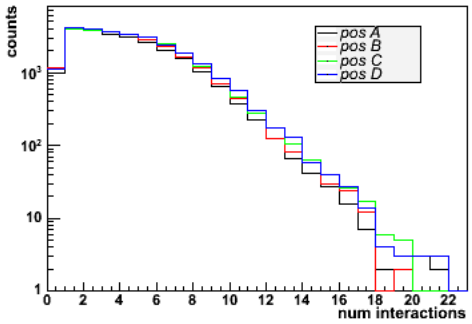

Figure 5.19: Number of Compton scattering processes in the fiducial volume for each event, due to both gammas simulated.

of 1.2 MeV. The two gammas are generated in the same position. To simulate the back to back generation of the two annihilation photons, the 0.511 MeV photon is simulated randomly in the geometrical cone defined by the NaI crystal; the second photon of 1.2 MeV energy is generated randomly in the 4π solid angle.

The fiducial volume, as already described, is surrounded by about 10 cm of liquid argon, and about 2 cm of stainless steel; hence the gammas entering the detector are not monochromatic. In Fig. 5.18(a) the energy of the first gamma entering the fiducial volume is reported; the total energy deposited in the fiducial volume, by both gammas, is shown in Fig. 5.18(b). Two peaks corresponding to the full energy deposited at 0.511 MeV and 1.2 MeV are visible in the spectrum of the energy deposited.

The interaction mainly contributing in the range of few hundred keV to few MeV is the Compton scattering; in Fig. 5.19 the number of Compton interactions, due to both gammas simulated, is shown: most of the events include more than one interaction. The position of the first Compton interaction in the fiducial volume is shown for the z-coordinate in Fig. 5.20 and in the *(xy)* plane in Fig. 5.21.

The p.e. spectrum obtained for the external gamma source has been compared with the MC expectation, obtained with the GEANT4 simulation, described in the previous section. For this purpose a further selection on the data has been applied:

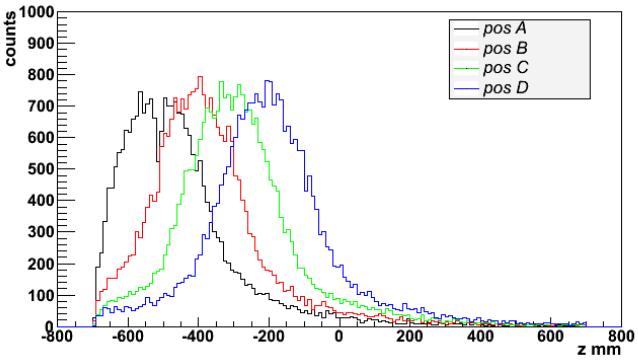

Figure 5.20: Z-coordinate position of the first Compton scattering in the fiducial volume, due to the first gamma entering it.

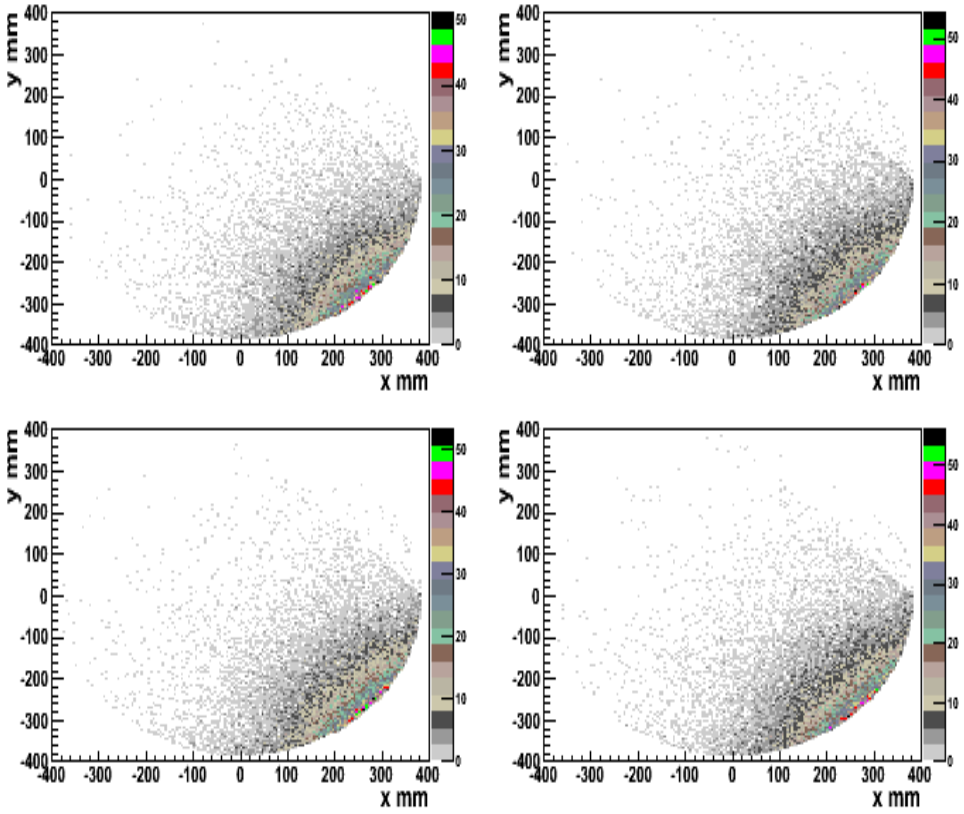

Figure 5.21: Scatter plot in the *(xy)* plane, of the position of the first Compton scattering in the fiducial volume, due to the first gamma entering it.

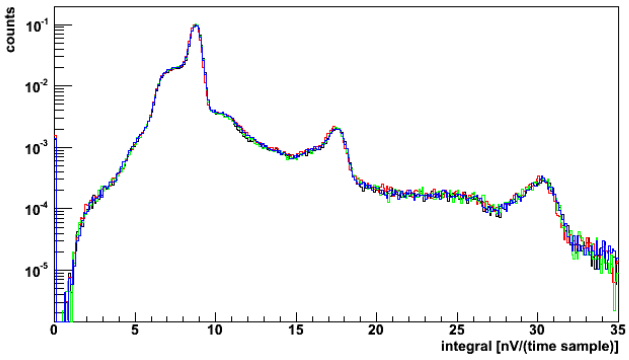

Figure 5.22: Integrated spectrum (nV/sample), of the NaI scintillator, used as trigger, in the four different positions of data taking.

as shown in Fig. 5.22 the spectrum collected by the NaI scintillator used as trigger is formed by three different peaks, the first one represents the detection of the gamma of 0.511 MeV energy emitted by the source, the second one to the detection of the 1.2 MeV γ energy and the third one to the detection of both. In the MC simulation a 0.511 MeV photons always enters the detector in each simulated event, so only the events in the first and in the third peak have been considered for the comparison with the MC simulation; in any case this choice permits to compare the events with correct energy simulated, but not the correct ratio between the number of events in each sample.

No background (from signal due to natural radioactive, or noise due to dark count) has been added to the MC expectation, and this explains the big difference in the very low energy (< 20 $p.e.$) part of the spectrum in Fig. 5.23. The collected p.e. expected by the MC simulation have been smeared, PMT by PMT, event by event, with a Gaussian function, with a sigma equal to the sigma obtained in the gain calibration fit of each PMT, to include the variation in the p.e. conversion factor. The MC spectrum is normalized to the number of selected gamma events, excluding the low energy part of the spectrum dominated by the background.

The data-MC comparison for the data taking at the highest position D, is shown in Fig. 5.23. The reflectivity of the reflector, the conversion efficiency of the TPB on the reflectors and on the PMTs have been set to the values reported in Tab. 5.3; with these assumptions the position of the peak generated by the $0.511MeV$ total energy deposition, is in quite good agreement.

reflectivity of reflector foils	92%
conversion efficiency TPB on the reflector foils	58%
conversion efficiency TPB on the PMTs	28%

Table 5.3: Values used in the MC simulation for the reflectivity, the TPB conversion efficiency on the reflector, and on the PMTs.

Measurements have confirmed that the reflectivity of the reflector foils should be bigger the 90%, and also MC tests show that lower values of the reflectivity induce both a lower light collection, and a distortion of the spectra shape, in particular the peak at 511 keV disappears, not compatible with the data.

Some tests have been made using an AmBe source, filling the detector with argon gas, to estimate the conversion efficiency of the TPB. Taking data with the source in different positions inside the detector and shielding the emitting source, to have scintillator light going down in the direction of the PMTs or up (in the direction of the gas phase), proves that the conversion efficiency of the TPB on the reflector foils is approximately a factor two bigger than on the PMTs, due probably to the different methods used to evaporate the TPB. Taking into account that the efficiency in cold liquid could be bigger than the one in warm gas, some MC tests have been done to fix the values of the TPB efficiency; the ratio between the two efficiencies was kept about a factor 2, and finally the values chosen at the end are shown in Tab. 5.3

In Fig. 5.24(a), 5.24(b), 5.24(c), 5.24(d), 5.24(e), 5.24(f), 5.24(g), 5.24(h), the data-MC comparison of the light collected is reported separately for each single PMT in the center of the PMT plane (number 3, 4, 5, 6, 7, 8, 10, 11). For these the agreement is good, with the exception of the 11th. In figure 5.25(a), 5.25(b), 5.25(c), 5.25(d),5.25(e), 5.25(f) the same comparison is reported for the outer PMTs (number 1, 2, 9, 12, 13, 14) and for these the disagreement is increased, in particular for the ones in the opposite position with respect to the external source. The general features of the PMT, in any case, respect quite good the MC expectations, and the disagreement seems due to geometrical reason.

The geometry implemented in the MC program is not describing accurately the detector geometry in the region of the PMT plane. In fact, the fiducial volume in the region of the PMT plane is limited by teflon foils, which haven't a well-defined geometry, wrapped around the PMTs. In the MC simulation we tried to introduce this effect by covering part of the photocathode of the outer PMTs, but no measurements are available with the part of the PMT photocathode covered. This differences in the geometry could explain the difference between the data and the simulation, considering also that this disagreement increases when the runs with the external source in the lower positions are considered.

	p.e./keV
position A	0.535 ± 0.002
position B	0.575 ± 0.002
position C	0.570 ± 0.002
position D	0.552 ± 0.002

Table 5.4: P.e. per keV expected by the MC simulation in the four different positions.

The MC simulation studies are ongoing, to define the correct geometry to describe the detector, however, the MC-data comparison showed that the peak of the spectrum

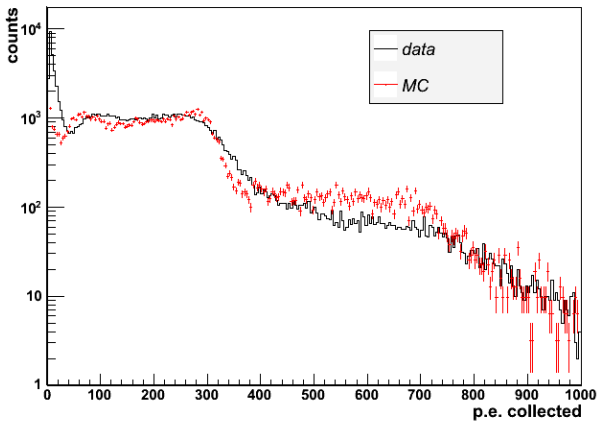

Figure 5.23: Total integrated spectrum (p.e.) collected from all 14 PMTs for the selected gamma events in black, and MC simulated spectrum in red.

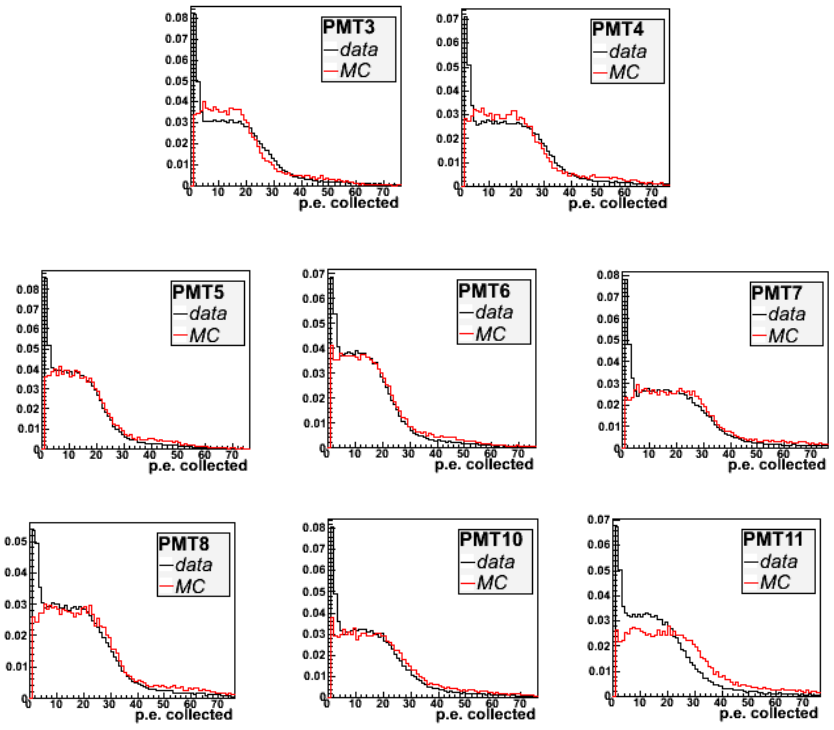

Figure 5.24: Integrated spectrum (p.e.) collected for the selected gamma events in black, and MC simulated spectrum in red, separately for PMT 3 in (a), PMT 4 in (b), PMT 5 in (c), PMT 6 in (d), PMT 7 in (e), PMT 8 in (f), PMT 10 in (g), PMT 11 in (h). The source is in the highest position D.

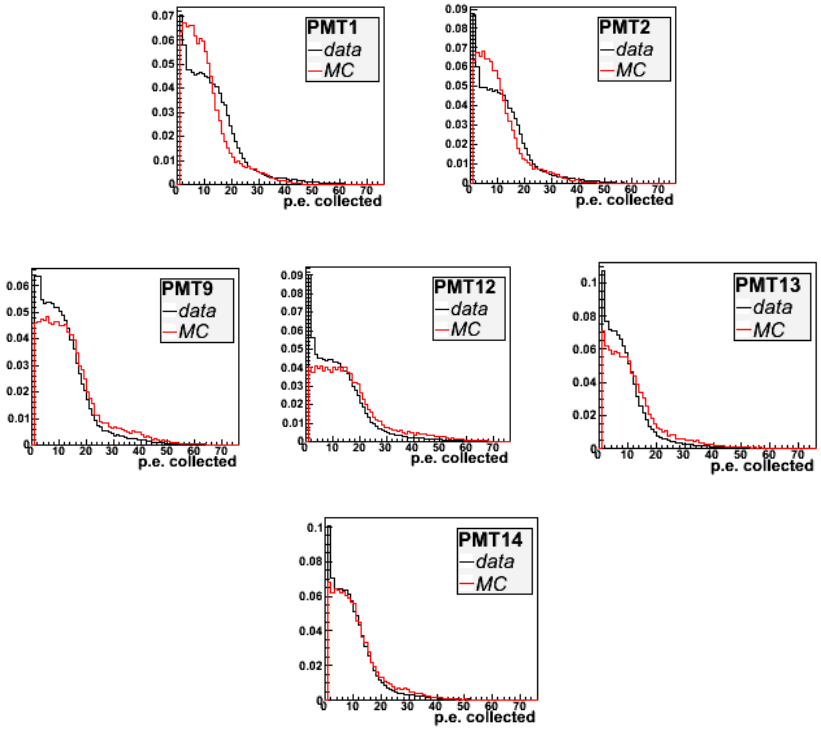

Figure 5.25: Integrated spectrum (p.e.) collected for the selected gamma events in black, and MC simulated spectrum in red, separately for PMT 1 in (a), PMT 2 in (b), PMT 9 in (c), PMT 12 in (d), PMT 13 in (e), PMT 14 in (f). The source is in the highest position D.

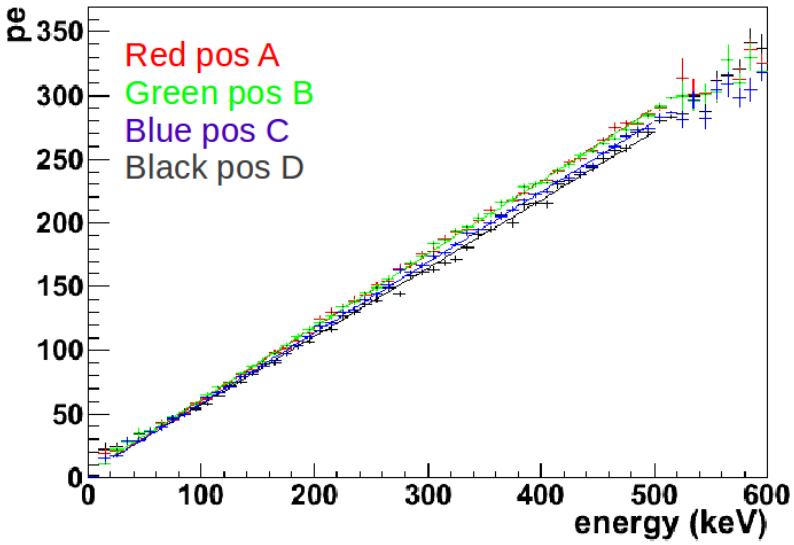

Figure 5.26: MC simulation of the mean number of p.e. collected as a function of the energy deposited by the γ's entering the detector, for the four source position A,B,C and D.

correctly represents the 511 keV energy deposition. So the light collection of the detector has been estimated using the MC simulation: the mean p.e. collected for each simulated event has been calculated sampling the events in bins of 2 keV of energy deposit in the fiducial volume, for each different position of the source. The results are shown in Fig. 5.26, the dependence is clearly linear as expected, and the results of the linear fit are shown in Tab. 5.4. The expected light yield of the detector with the source in the lowest position is 0.535 ± 0.002 p.e./keV, where the error is only statistical.

Conclusions

In this second part of the thesis a short description of the ArDM experiment is given. The ArDM detector is a 1 ton LAr TPC to search for Dark Matter by detecting elastic collisions of hypothetical WIMPs with argon nuclei. The ratios of the ionization charge to the scintillation light and of the fast to the slow component of the scintillation light are the main and most important criteria to distinguish recoiling nuclei from gamma and electron background. Hence, it is important to understand perfectly the light collection capability of the detector, and to test the discrimination of the electron-gamma recoil events from the nuclear recoil events.

In this thesis preliminary results on the light collection from the first test in September-October 2010, is presented. The analysis confirms the dependence of the detector light collection on the height of the position of the external source with respect to the PMT plane, as expected. The data-MC comparison shows a big difference between data and expectation, understandable if a low TPB conversion efficiency is considered, both, for the TBP coating of the PMTs and the reflector foils. In particular, a conversion efficiency of the TPB on the reflector foils is expected to be higher than the one of the TPB coating of the PMTs.

The difference in the data-MC comparison between different positions of the source, especially for the outer PMTs, indicates a problem in the MC geometry description, which affects mainly the region near the HV cathode.

These results suggest to begin some dedicated studies on the PMT coating, to improve the efficiency of the TPB conversion, that could increase the light yield.

Bibliography

[1] W. Pauli, *Letter to radioactive ladies and gentleman*, at the Tubigen conference, 4 Dec. 1930.

[2] M. Goldhaber, L. Grodzins, and A. W. Sunyar; *Helicity of neutrinos. Phys. Rev.*, 1015-1017, Feb 1958.

[3] K. Kodama et al. (DONUT Collaboration), *Physics Letters B 504* 218 (2001); arXiv:hep-ex/0012035.

[4] Gargamelle Neutrino Collaboration (F.J. Hasert et al.), *Phys. Lett., B46* 138-140, 1973.

[5] D. Decamp et al. (ALEPH collaboration), *Physics Letters B 231*, 519 (1989).

[6] C. Giunti et M. Laveder, arXiv:hep-ph/0310238v2.

[7] M. Gell-Mann, P. Ramond and R. Slansky, in *SuperGravity*, edit by D. Freedman and P.vanNieeuwenhuizen (North-Holland, Amsterdam, 1979), p. 315.

T. Yanagida, *Proceedings of the Workshops on Unified Theory and Baryon Number in the Universe*, ed. O. Oswada and A. Suganiti (Japan, 1979).

R.N.Mohapatra and G. Senjanovic, *Phys. Rev. Lett 44* (1980) 912.

[8] Z. Maki, M. Nakagata, S. Sakata, *Prog. Theor. Phys. 28*, 870 (1962).

Pontecorvo, *Zh. Eksp. Toer. Fiz. 53*,1717 (1967) [*Sov. Phyys. JETP 26*, 984 (1968)].

[9] Boris Kayser; arXiv:hep-heh/0804.1121v3.

[10] L. Camilleri, E. Lisi, John F. Wilkerson, *Annu. Rev. Nucl. Part. Sci. 58:343-69*, 2008.

[11] Kraus C, et al., *Eur. Phys.J* C 40-447 (2005).

[12] K. Assamagan et al., *Phys. Rew. D53* 6065 (1995).

[13] R. Barate et al., *Eur. Phys. J. C2* 395 (1998).

[14] WMAP Collaboration; astro-ph/0803.0586 (2006).

[15] SDDS Collaboration, *Phys. Rev. D74* 123507 (2006); arXiv:astro-ph/0510447.

[16] H.V. Klapdor-Kleingrothaus, et al. *Phys. Lett. B 586* 198 (2004).

H.V. Klapdor-Kleingrothaus, et al.*Nucl. Instr. Meth. A 522* 371 (2004).

[17] Bahcall JN. *Phys. Rev. Lett. 12*, 300 (1964).

[18] Homestake Collaboration, *Astrophys. Journal. 496* 505 (1998).

[19] SAGE collaboration *Phys. Rev.C 60* 055801.

[20] Gallex Collaboration, *Phys. Lett. B 447* 127 (1999).

[21] GNO Collaboration, *Phys. Lett. B 616* 174 (2005); arXiv:hep-ex/0504307.

[22] K.S. Hirata et al., *Phys. Rev. Lett. 65*, 1301-1304 (1990).

[23] Kamiokande collaboration, *Phys. Rev. Lett. 77* 1683 (1996).

[24] SuperKamiokande collaboration, *Phys. Rev. Lett. 90* 171302 (2003); arXiv:hep-ex/0212067.

SuperKamiokande collaboration, *Phys. Rev. D69* 011104 (2004); arXiv:hep-ex/0309011.

SuperKamiokande collaboration: arXiv:0803.4312.

[25] SNO Collaboration, *Nucl. Instrum. Methods Phys. Res. Sect A 449* 172 (2000).

[26] SNO Collaboration, *Phys. Rev. Lett. 101, 11301* (2008).

[27] KamLAND Collaboration, S. Abe et al., *Phys. Rev. Lett. 100* 221803 (2008); arXiv:0801.4589v3 [hep-ex].

[28] Borexino Collaboration, *Phys.Rev.Lett.101* 091302, (2008); arXiv:atr0805.3843.

[29] Gaisser TK, *Phys. Scr. T121* 51 (2005).

[30] Hirata KS et al., *Phys. Lett. 18* 196 (1988).

[31] Becker-Szendy R. et al. *Phys. Rev. D 205* 416 (1992).

[32] Allison WWM et al. *Phys. Lett. B 391* 491 (1997).

[33] The SK Collaboration, *Phys. Rev.. D 81* 092004 (2010); arXiv:1002.3471v1[hep-ex].

[34] MINOS collaboration; arXiv:0708.1495.

[35] K2K collaboration, *Phys. Rev. D74* 72003 (2006); arXiv:hep-ex/060603.

[36] MINOS collaboration, *Phys. Rev. Lett. 101* 1131808 (2008); arXiv:hep-heh/1004.2647v1 (2010).

[37] CHOOZ collaboration, *Phys. Lett. B466* 415 (1999); arXiv:hep-ex/9907037.

[38] LSND collaboration, *Phys.Rev.Lett. 77* 3082, (1998); arXiv:nucl-ex/9709006.

LSND collaboration, *Phys.Rev.Lett. 81* 1774, (1998); arXiv:nucl-ex/9605003.

[39] KARMEN collaboration, *Phys. Rev. D65* 112001 (2002); arXiv:hep-ex/0203021.

[40] MiniBoone collaboration, arXiv:0704.1500.

[41] MiniBooNE Collaboration, *Phys. Rev. Lett. 105*, 181801 (2010); arXiv:hep-ex/1007.1150v3.

[42] http://www.neutrino2010.gr.

[43] T. Schwetz, M. Tortola, Jose W.F. Valle, *New J.Phys. 10* 113011 (2008); arXiv:hep-ph/0808.2016v3.

[44] M. Mezzetto, T. Schwetz, *J. Phys. G37* 103001 (2010); arXiv:hep-ph/1003.5800v2.

[45] G. L. Fogli, E. Lisi et al., arXiv:hep-ph/0905.3549v2.

[46] M. Ishitsuka, T. Kajita, H. Minakata, H. Nunokawa; *Phys. Rev. D72* 033003 (2005); arXiv:hep-ph/0504026.

[47] F. Ardellier et al., *Double Chooz: A search for the neutrino mixing angle* θ_{13}, (2006); hep-ex/0606025.

[48] X. Guo et al., *A precision measurement of the neutrino mixing angle* θ_{13} *using reactor antineutrinos at Daya Bay*, (2007); hep-ex/0701029.

[49] C. Giunti, Chung W. Kim: *Fundamentals of neutrino physics and astrophysics*, Oxford University Press (2007).

[50] G.P. Zeller; arXiv:hep-ex/0312061v1.

[51] E. A. Paschos, *Nucl. Phys. Proc. Suppl. 112* 89-97 (2002); arXiv:hep-ex/0204138v1.

[52] P. Lipari, *Nuclear Physics B (Proc. Suppl.)*, 274-287 (2002).

[53] M. Guler et al. OPERA: *An appearance experiment to search for* $\nu_\mu \to \nu_\tau$ *oscillations in the CNGS beam. Experimental proposal.* CERN-SPSC-2000-028, CERN-SPSC-P-318, July 2000.

[54] http://www.lngs.infn.it/

[55] M. Buhler-Broglin et al., CERN AC Note (2000-03)

CNGS project: [http://proj-cngs.web.cern.ch/proj-cngs/

[56] R. Acquafredda et al. [OPERA Collaboration], *The OPERA experiment in the CERN to Gran Sasso neutrino beam.* JINST 4 (P04018) (2009).

[57] E. Eskut et al. (CHORUS Collaboration), Nucl. Instrum. Meth. A 401, 7 (1997).

[58] A. Anokhina et al. [OPERA Collaboration], *Emulsion sheet doublets as interface trackers for the OPERA experiment* JINST 3 (P07005) (2008).

[59] T. Nakamura et al., *The OPERA film: New nuclear emulsion for large-scale, high-precision experiments. NIM A 556* (2006) 80-86.

[60] A. Anokhina et al. [OPERA Collaboration], *Study of the effects induced by lead on the emulsion films of the OPERA experiment. JINST 3* (P07002) (2008).

[61] T. Fukuda, K. Kodama, M. Komatsu, S. Miyamoto, K. Morishima, T. Nakano, T. Omura, Y. Sakatani, and O. Sato. *The analysis of interface emulsion detector for the OPERA experiment in Japan scanning facility. Journal of Instrumentation*, 5(04):P04009 (2010).

K. Morishima and T. Nakano, *Development of a new automatic nuclear emulsion scanning system, S-UTS, with continuous 3d tomographic image read-out*, Journal of Instrumentation, 5(04):P04011 (2010).

[62] N. Armenise et al., *High-speed particle tracking in nuclear emulsion by last-generation automatic microscopes. Nucl. Instrum. Meth.*, A551:261 (2005).

L. Arrabito et al., *Hardware performance of a scanning system for high speed analysis of nuclear emulsions. Nucl. Instrum. Meth.*, A568:578 (2006).

L. Arrabito et al., *Track reconstruction in the emulsion-lead target of the OPERA experiment using the ESS microscope., JINST*, 2:P05004 (2007).

[63] A. Mengucci, A. Paoloni, M. Spinetti, and L. Votano, *Gas mixture studies for streamer operation of Resistive Plate Chambers at low rate. Nucl. Instrum. Meth. A 583(2-3)*, 264 (2007).

[64] R.Zimmermann et al., *The precision tracker of the OPERA detector., Nucl. Instr. Meth.* A555, 435, (2005).

[65] B. Wonsak, *The recosntruction if tracks with the drift tubes in the muon spectrometers of the neutrino experiemnt OPERA*, DESY_THESIS-2007-035 (2007).

[66] R. Zimmermann et al., *A general track reconstruction scheme and its application to the OPERA drift tubes* OPERA internal notes 83 (2007).

[67] PhD Thesis T.Tran: *Recherche des oscillations de neutrinos par apparition du nu-tau avec désintégration muonique du tau dans l'expérience OPERA*, Université Claude Bernard Lyon I; OPERA internal page.

[68] R. Acquafredda et al., *First events from the CNGS neutrino beam. New J. Phys.* 8 303 (2006).

[69] A. Bertolin et N. T. Tran. *OpCarac: an algorithm for the classification of the neutrino interactions recorded by OPERA*. OPERA internal note, August 2009.

[70] B. Van de Vyver. *Nucl. Instr. and Meth. A 385* (1997).

M.C. Gonzalez-Garcia and J.J. Gomez-Cadenas. *Physics Review D 55* 1297 (1997)

[71] A. Kayis-Topaksu [CHORUS Collaboration]. *Associated Charm Production in Neutrino-Nucleus Interactions. The European Physical Journal. C, Particles and Fields 2007*, vol. 52, no3, pp. 543-552. CERN-PHEP-2007-031.

[72] OPERA Collaboration. *Observation of the first τ candidate in the OPERA experiment in the CNGS beam. Physics Letters B* 691 (2010). (arXiv:1006.1623v1).

[73] PhD Thesis Knuesel J., *Study of physics background and track reconstruction efficiency for the data analysis of the OPERA experiment*, University of Bern, OPERA internal pages. (2010).

[74] PhD Thesis Cazes A., *Étude du faisceau CNGS et identification des muons dans l'exprience OPERA. Optimisation de la ligne de faisceau du projet SPL-F*, Université de Paris VI Pierre et Marie Curie, OPERA internal pages.

[75] A. Cazes, Jean Eric Campagne, *Pattern Recognition*, OPERA internal notes.

[76] R.E. Kalman; *Transaction of the ASME- Journal of Basic Engineering, 82* 35-45 (1960).

[77] Sorenson, H.W 1970.*IEEE Spectrum vol. 7* 63-68 (1970), *Least-Squares estimation: from Gauss to Kalman.*

[78] R. Frühwirth, *Application of the Kalman filtering to track and vertex filtering*, *Nucl. Instr. Meth. A262*, 444 (1987).

[79] Welch, Bishop; SIGGRAPH 2001 Course.

[80] P. Billoir, *Track Fitting with multiple scattering: a new method*, *Nucl. Instr. Meth. 225*, 352, (1984).

[81] J.E. Campagne, *Muon tracking in heterogeneous structures.* OPERA internal notes.

[82] R. Zimmermann *Charge sign determination with the Precision Tracker of OPERA.* OPERA internal notes.

[83] OPERA collaboration, R. Acquafredda et al., JINST 4 P04018 (2009).

[84] J. Marteau for the OPERA Collaboration, Nucl. Instrum. Meth. A 617, 291 (2010).

[85] OPERA collaboration, arXiv:hep-ex/1102.1882v1.

[86] A. Ferrari et al. Nuclear Physics B (Proc. Suppl.) 145 (2005).

[87] F. Zwicky, *Helv. Physica Acta. 1933. V.6.*, 110.

[88] W. Rau, *Proceedings of the IVth International Pontecorvo Neutrino Physics School, pubblished in Physics of Elementary Particles and Atomic Nuclei*; arXiv:astro-ph/1103.5267v1.

[89] Riotto A., CERN Yellow Report CERN-2010-001, 315-362; arXiv:hep-ph/1010.2642v1.

[90] E. Aprile et al. (XENON100), *Phys. Rev. Lett 105*, 131302 (2010).

[91] E. Armengaud et al. (EDELWEISS), arXiv:1103.4070.

[92] Z. Ahmed et al. (CDMS), *Science 327* 1619 (2010).

[93] O. Buchmueller et al., arXiv:1102.4585 (2011).

[94] C.E. Aalseth et al. (CoGeNT), *Phys. Rev. Lett. 106*, 13301 (2011).

[95] C. Savage et al., *JPAC 0904*, 010 (2009).

[96] XENON100 Collaboration, arXiv:astro-ph/1104.2549.

[97] M. Miyajima et al., *Phys. Rev. A9* 1438-1443 (1974).

[98] T. Doke, K. Masuda and E. Shibamura, *Nucl. Instrum. Meth, A291*617-620 (1990)

[99] A. Marchionni and ArDM Collaboration, arXiv:1012.5967 (2010).

[100] C. R. Gruhn and Edmiston, *Phys. Rev. Lett. 40* 407- 409 (1978).

R. T. Scalettar, P. J. Doe, H. J. Mahler and Chen, *Phys. Rev. A 25 2419-2422* (1982).

E. Shibamura et al., *Nucl. Instrum. Meth. A260 437- 442* (1987).

J. Thomas and Imel, *Phys. Rev. A 36 614-616* (1987).

[101] S. Amoruso et al. (ICARUS), *Nucl. Instrum. Meth. A523 275-286* (2004).

[102] P. Cenninia, S. Cittolin, *Nucl. Instrum. Meth. A 345 230-243* (1994).

[103] Lippincott et al., *Phys.Rev. C78 035801* (2008).

[104] M. Mijajima et al., *Phys. Rev. A 9* , 1438 (1974).

[105] S. Kubota et al., *Phys. Rev. B 17* 2762 (1978).

[106] T. Doke et al., *Nucl. Instr. and Meth. A 269*,291 (1988).

[107] H. Loosli, *Earth and Planetary Science Letters 63* 51, (1983).

[108] P. Benetti et al. (WARP), *Nucl. Instrum. Meth. A574*, 83 (2007);

Preprint astro-ph/0603131.

[109] D. Acosta-Kane R. et al., arXiv:astro-ph/0712.0381.

[110] A. Rubbia, *ArDM: A ton-scale liquid argon experiment for direct detection of dark matter in the universe*, J. Phys. Conf. Ser. 39 (2006) 129. (arXiv:hep-ph/0510320).

[111] L. Kaufmann and A. Rubbia, *The ArDM Project: A Direct Detection Experiment, Based On Liquid Argon, For The Search Of Dark Matter. Nucl. Phys. Proc. Suppl.* 173 (2007) 141.

[112] A. Badertscher et al., *NIM A 641*, (2011) 48.

[113] L. Kaufmann, PhD thesis: *Detector Performance and Background Studies for the ArDM Experiment*, ETH Zürich (2008).

[114] L. Kaufmann, A. Rubbia, arXiv:hep-ph/0612056v1 (2006).

[115] LCS Laboratorio Subterraneo de Canfranc, www.isc-canfranc.es.

[116] J.M. Carmona, S. Cebrian, *Astroparticle Physics 21 523* (2004).

[117] WARP collaboration, arXiv:0804.1217 (2008).

[118] A. Badertscher et al., arXiv:1012.0483 (2010).

[119] http://www.geant4.org/geant4/

Acknowledgements

First of all I want to express my gratitude to Prof. André Rubbia for the possibility to get my Ph.D. at the particle physics institute of ETH Zürich. I thank Andreas and Alessandro for reading this thesis, for the corrections and the useful discussions.

I am grateful for the daily support to the ETH group: Alberto, Devis, Federico, Filippo, Lukas, Luigi, Silvestro, Sosuke, Thierry and Ursina, and to Rosa for her help in all the administrative issues.

I want express my gratitude to the OPERA collaboration people that helped me: Alessandro B., Anselmo, Dario, Stefano; and a big thank to all the friends that I found in this collaboration for the nice time spent together during collaboration meetings and shift weeks.

I like to thank the friends that I have known in Geneva and the friends in Italy that help me since many years.

Finally, a special big thank to my brother, my niece and all my family: without you I could not finish.